A Thesis Submitted for the Degree of PhD at the University of Warwick

Permanent WRAP URL:

http://wrap.warwick.ac.uk/152399

Copyright and reuse:

This thesis is made available online and is protected by original copyright.

Please scroll down to view the document itself.

Please refer to the repository record for this item for information to help you to cite it.

Our policy information is available from the repository home page.

For more information, please contact the WRAP Team at: wrap@warwick.ac.uk

warwick.ac.uk/lib-publications
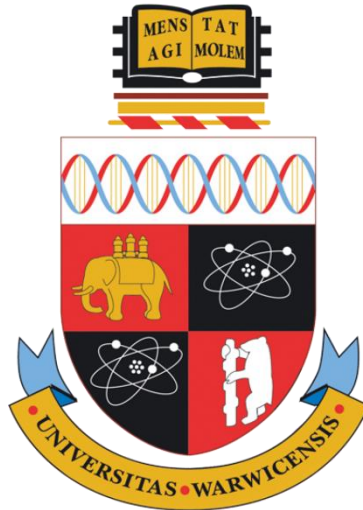
Cardiac Image Computing
for Myocardial Infarction Patients

By

Jayendra Maganbhai Bhalodiya

A thesis submitted to The University of Warwick, in partial

fulfilment of the requirements for the degree of

Doctor of Philosophy in Engineering

Warwick Manufacturing Group,

The University of Warwick

March 2020

TABLE OF CONTENTS

Dedicated to the bond of relationship that we shared with

Prof Tiwari

ACKNOWLEDGEMENTS

Amoroso, Zhou Yutao, Waltraud Baier, Guillaume Remy, and Mike Donnelly. A big hug to you guys.

Finally, I heartily acknowledge a tiny significant human, Maryam Sharifzadeh, who would still be reading the whole thing and looking out for her name. I am grateful to Maryam for putting quite a lot of her emotions into my PhD. Despite having cultural and technical differences, she has been an absolute gem during PhD journey.

Also, I would like to thank myself for taking so many decisions from the beginning until the end.

Thank you

DECLARATION

This thesis is submitted to the University of Warwick in support of my application for Doctor of Philosophy. I have composed it by myself, and I have not submitted it in any previous application for any degree.

I have obtained the required ethical approvals (as provided in the APPENDIX-1) to conduct this research from the University of Warwick and Royal Brompton and Harefield NHS foundation trust. I have provided a copy of my Honorary Observer placement contract with the Royal Brompton hospital in APPENDIX-1. Anonymised human data had been securely stored and analysed by the author. I have provided a computer algorithm in APPENDIX-2.

This thesis is presented by following the rules and regulations of the University of Warwick.

LIST OF PUBLICATIONS

- Bhalodiya, J. M., Palit, A., Tiwari, M. K., *et al.* (2018) 'A Novel Hierarchical Template Matching Model for Cardiac Motion Estimation', *Scientific Reports*, 8(1), p. 4475. doi: 10.1038/s41598-018-22543-y.

- Bhalodiya, J. M., Palit, A., Ferrante, E., *et al.* (2019) 'Hierarchical Template Matching for 3D Myocardial Tracking and Cardiac Strain Estimation', *Scientific Reports*, 9(1), p. 12450. doi: 10.1038/s41598-019-48927-2.

- Bhalodiya, J. M., Palit, A., Giblin, G., *et al.* (2021) 'Identifying Myocardial Infarction Using Hierarchical Template Matching–Based Myocardial Strain: Algorithm Development and Usability Study', *JMIR Med Inform*, 9(2), p. e22164. doi: 10.2196/22164.

ABSTRACT

Cardiovascular diseases (CVDs), which are a prime cause of global mortality, are disorders that affect the heart and blood vessels' functioning. CVDs may cause consequent complications, due to occlusion in a blood vessel and present as impaired cardiac wall functioning (myocardium). Identifying such impairment (infarction) of the myocardium is of great clinical interest, as it can reveal the nature of altered cardiac topography (ventricular remodelling) to aid the associated intervention decisions.

With recent advances in cardiac imaging, such as Magnetic Resonance (MR) imaging, the visualisation and identification of infarcted myocardium has been routinely and effectively used in clinical practice. Diagnosing infarcted myocardium is achieved clinically through the late gadolinium enhancement (LGE) test, which acquires MR images after injecting a gadolinium-based contrast agent (GBCA). Due to the increased accuracy and reproducibility, LGE has emerged as the gold-standard MR imaging test in identifying myocardial infarction. However, clinical studies have reported gadolinium deposition concerns in different body organs and adverse outcomes in patients with advanced kidney failure, over time. Such incidents have motivated researchers to look into the development of both accurate as well as safe diagnostic tools.

Emerging research on identifying infarcted myocardium utilises myocardial strain to safely identify infarcted myocardium, which has been addressed in the presented study. For example, myocardial strain represents the shortening or lengthening of the myocardium. If the myocardium is infarcted, then the corresponding strain values differ compared to the healthy myocardium. This finding can be identified and utilised for clinical applications. The research presented in this thesis aims to identify infarcted myocardium accurately and safely by using

myocardial strain (shortening or lengthening of the myocardium).

To achieve the aforementioned aim, the research methodology is divided into six objectives. The initial objectives relate to the development of a novel myocardial tracking method. The middle objectives relate to the development of clinical application methods, and the final objectives concern the validation of the developed methods through clinical studies and associated datasets. The research presented in this thesis has addressed the following research question:

> Research question 1: How can a 2D myocardial tracking and strain calculation method be developed using the 2D local weighted mean function and structural deformation within the myocardium?

> Research question 2: How can a 3D myocardial tracking and strain calculation method be developed using the 3D local weighted mean function to calculate 3D myocardial strain?

> Research question 3: How can 2D circumferential strain of the myocardium be used in identifying infarcted left ventricular segments for the diagnosis of myocardial infarction patients?

In literature, myocardial tracking and strain calculation methods have limited extension to 3D and dependency on tissue material properties. Moreover, additional limitations, such as limited inclusion of structural deformation details within the myocardium, are found in the literature. Therefore, methods are likely to become subjective or numerically unstable during computation. Moreover, the inclusion of myocardial details with grid-tagging MRI, for structural deformation within the myocardium, is more realistic compared to cine MRI.

The aforementioned limitations are overcome by proposing a novel Hierarchical Template Matching method, which performs non-rigid image registration among grid-tagging MR images of a cardiac cycle. This is achieved by employing a local weighted mean transformation function. The proposed non-rigid image registration method does not require the use of tissue material properties. Grid-tagging MRI is used to capture wall function within the myocardium, and the local weighted mean function is used for numerical stability. The performance of the developed methods is evaluated with multiple error measures and with a benchmark framework. This benchmark framework has provided an open-access 3D dataset, a set of validation methods, and results of four leading methods for comparison. Validation methods include qualitative and quantitative methods. The qualitative assessment of outcomes and verified ground truth for the quantitative evaluation of results are followed from the benchmark framework paper (Tobon-Gomez, Craene, Mcleod, *et al.*, 2013).

2D HTM method has reported the root mean square error of point tracking in left ventricular slices, which are the basal slice 0.31 ± 0.07 mm, the upper mid-ventricular slice 0.37 ± 0.06 mm, the mid-ventricular slice 0.41 ± 0.05 mm, and the apical slice 0.32 ± 0.08 mm. The mid-ventricular slice has a significantly higher 4% (P=0.05) mean root mean square error compared to the other slices. However, the other slices do not have a significant difference among them. Compared to the benchmark free form deformation method, HTM has a mean error of 0.35 ± 0.05 mm, which is 17% (P=0.07, CI:[-0.01,0.35]) reduced to the free form deformation method.

Our technical method has shown the 3D extension of HTM and a method without using material properties, which is advantageous compared to the methods which are limited to 2D or dependent

on material properties. Moreover, the 3D HTM has demonstrated the use of 3D local weighted mean function in 3D myocardial tracking. While comparing to the benchmark methods, it was found that the median tracking error of 3D HTM is comparable to benchmark methods and has very few outliers compared to them.

The clinical results are validated with LGE imaging. The quantitative error measure is the area under the curve (AUC) of sensitivity vs 1-specificity curve of the receiver operating characteristic (ROC) test. The achieved AUC value in detecting infarcted segments in basal, mid-ventricular, and apical slices are 0.85, 0.82, and 0.87, respectively. Calculating AUC with 95% confidence level, the confidence intervals of lower and upper mean AUC values in basal, mid-ventricular and apical slices are [0.80, 0.89], [0.74, 0.85], and [0.78, 0.91], respectively. Overall, considering the detections of LGE imaging as the base, our method has an accuracy of AUC 0.73 (P=0.05) in identifying infarcted left ventricular segments.

The developed methods have shown, systematically, a promising approach in identifying infarcted left ventricular segments by image processing method and without using GBCA-based LGE imaging.

ABBREVIATIONS

AHA	American Heart Association
AUC	Area Under the Curve
BHF	British Heart Foundation
BSREC	Biomedical and Scientific Research Ethics Committee
CABG	Coronary Artery Bypass Graft
CC	Correlation Coefficient
CMR-FT	Cardiac Magnetic Resonance-Feature Tracking
CT	Computed Tomography
CVDs	Cardiovascular Diseases
DENSE	Displacement Encoding with Stimulated Echoes
DICOM	Digital Imaging and Communications in Medicine
ECG	Electrocardiogram
Echo	Echocardiography
ECV	Extracellular Volume
ED	End-Diastolic frame
ES	End-Systolic frame
FDA	Food and Drug Administration
FFD	Free-Form Deformation
GBCA	Gadolinium-based Contrast Agents
HARP	Harmonic Phase contrast
HTM	Hierarchical Template Matching
HTM-CS	Hierarchical Template Matching-Circumferential Strain
INRIA	National Institute for Research in Computer Science and Automation-Asclepios project
IUCL	Imperial College London-University College London
LA	Left Atrium
LAX	Long-axis
LCA	Left Coronary Artery
LCx	Left Circumflex
LGE	Late Gadolinium Enhancement
LV	Left Ventricle
LVEF	Left Ventricular Ejection Fraction
LWM	Local Weighted Mean
MC	Moving Chunk
MEVIS	Fraunhofer-Institut für Digitale Medizin
MI	Myocardial Infarction
Mm	Millimetre
MRI	Magnetic Resonance Imaging
MS	Moving Segment
MT	Moving Template
MW	Moving Window

MX	Moving template section
MY	Moving segment section
NaN	Not a Number
NCC	Normalised Cross-Correlation
PCI	Percutaneous Coronary Intervention
PET	Positron Emission Tomography
RA	Right Atrium
RBHT	Royal Brompton and Harefield NHS Foundation Trust
RC	Reference Chunk
RCA	Right Coronary Artery
RMSE	Root Mean Square Error
ROC	Receiver Operating Characteristics
RS	Reference Segment
RT	Reference Template
RV	Right Ventricle
RW	Reference Window
RX	Reference template section
RY	Reference segment section
SAX	Short-axis
SENC	Strain Encoding
SinMod	Sine Wave Modelling
SPECT	Single-Photon Emission Computed Tomography
SSFP	Steady-State Free Precession
STE	Speckle Tracking Echocardiography
TDI	Tissue Doppler Imaging
TRE	Target Registration Error
UK	United Kingdom
UPF	Universitat Pompeu Fabra

LIST OF TABLES

LIST OF FIGURES

Chapter 1

Introduction

1.1 Introduction to the thesis

1.1.1 Background and motivation to the research

Cardiovascular diseases (CVDs) are the prime cause of global mortality (WHO, 2017). In 2016, approximately 17.9 million deaths occurred due to CVDs, which accounted for 31% of all global deaths; the reported primary conditions were myocardial infarctions and strokes (WHO, 2017). In the United Kingdom (UK), myocardial infarction causes one hospital visit every three minutes (BHF, 2019). Furthermore, official reports show that every year approximately 735,000 Americans suffer from myocardial infarction. Out of them, about 525,000 have a first-time myocardial infarction, and approximately 210,000 have a second-time myocardial infarction (CDC, 2015). Such incidents show a need to improve cardiac treatments. As treatments depend on diagnostic results, an accurate diagnosis plays a crucial role in treatment planning.

Researchers have contributed towards cardiac diagnosis methods, inspired by cardiac muscle behaviour and mechanics (Sengupta, Tajik, Chandrasekaran, *et al.*, 2008; Smiseth, Torp, Opdahl, *et al.*, 2016). This has enabled researchers to develop clinical tools such as speckle tracking (Crosby, Amundsen, Hergum, *et al.*, 2009). Growing knowledge, such as the material properties of cardiac muscle, and technological advancements, such as magnetic resonance imaging (MRI), have opened up opportunities to improve diagnosis tools (Lima and Desai, 2004).

A diagnosis tool should be accurate and safe for the ideal treatment. Moreover, it should be convenient for patients as well as clinical experts.

One of the heart conditions, which is clinically referred to as myocardial infarction (MI), arises due to insufficient blood supply to the cardiac wall muscle (myocardium) (Thygesen, Alpert, Jaffe, *et al.*, 2012). The diagnosis involves assessing reduced blood flow and muscular damage (clinically referred to as infarction) of the myocardium (Pennell, Sechtem, Higgins, *et al.*, 2004). Detecting infarction is a crucial diagnostic criterion, as it helps to understand the nature of ventricular remodelling (Pfeffer and Braunwald, 1990; Azevedo, Polegato, Minicucci, *et al.*, 2016).

In current clinical practice, clinical experts utilise late gadolinium enhancement (LGE) imaging in identifying such myocardial infarction (Pennell, Sechtem, Higgins, *et al.*, 2004; Flett, Hasleton, Cook, *et al.*, 2011). LGE imaging uses gadolinium-based contrast agents (GBCA) to highlight infarcted myocardium. Gadolinium deposits in infarcted myocardium approximately 15-20 minutes after injection, and the subsequent MRI shows infarcted myocardium with higher image intensity values (Pennell, Sechtem, Higgins, *et al.*, 2004). Such an approach of LGE imaging is promising in identifying infarcted myocardium. However, gadolinium deposition may bring allergic reactions such as urticaria and anaphylaxis (Jung, Kang, Kim, *et al.*, 2012). Such reactions depend on the type of contrast agents (McDonald, Hunt, Kolbe, *et al.*, 2019) and are controlled with premedication like antihistamine (Jung, Kang, Kim, *et al.*, 2012). However, there could be a possibility of adverse incidents like death, despite antihistamine premedication (Jung, Kang, Kim, *et al.*, 2012). Moreover, GBCA usage can bring adverse situation like nephrogenic systemic fibrosis in advanced renal insufficiency patients. Therefore, GBCA is contraindicated to use in chronic kidney disease stage 4 or 5 patients (glomerular filtration rate less than 30 ml/min/1.73m^2) (Thomsen, Morcos, Almén, *et al.*, 2013; McDonald, McDonald, Kallmes, *et al.*, 2015; Nezafat, 2015). Such advanced renal insufficiency patients cannot be benefitted

from LGE imaging-based diagnosis. Besides, even normal renal sufficiency patients are reported with gadolinium deposition in neuronal tissues (McDonald, McDonald, Kallmes, *et al.*, 2015). Inductively coupled plasma mass spectrometry of autopsied brain, transmission electron microscopy, and precontrast T1-weighted imaging have shown the gadolinium deposition in brain tissues (McDonald, McDonald, Kallmes, *et al.*, 2015). Therefore, LGE imaging may compromise patient safety and care due to gadolinium deposition (Bruder, Schneider, Nothnagel, *et al.*, 2011; Nezafat, 2015). It should also be acknowledged that LGE imaging is reported with higher accuracy and sensitivity (Pennell, Sechtem, Higgins, *et al.*, 2004). Another important criterion in diagnosing myocardial infarction patients is identifying hibernating myocardium (B. and Joseph, 2002). Hibernating myocardium refers to the state of dysfunction in the myocardium due to a reduction in coronary blood flow (B. and Joseph, 2002). Such hibernating myocardium could be fixed with blood reperfusion therapy. Therefore, identifying hibernating myocardium is helpful for prognosis. Similarly, identifying infarcted myocardium is also clinically useful as the large infarction can produce alterations in ventricular topography, affecting the prognosis in terms of patient survival (Pfeffer and Braunwald, 1990).

Myocardial strain, which is defined as shortening or lengthening of the muscle (Lai, Rubin and Krempl, 2010; Smiseth, Torp, Opdahl, *et al.*, 2016), can help identify such infarcted myocardium. Strain can be calculated during different phases of the cardiac cycle. In the cardiac cycle, systole is when muscle contraction happens, and blood is pumped out from the ventricles, which results in maximum muscle contraction at the end of systole (Katz, 2011). Therefore, researchers have utilised systolic strain, which is defined as the myocardial strain at the

end of systole, as a diagnostic measure (Crosby, Amundsen, Hergum, *et al.*, 2009).

Researchers have created safe clinical tools, based on myocardial strain for diagnosis (Gorcsan and Tanaka, 2011; Smiseth, Torp, Opdahl, *et al.*, 2016). Strain can be measured by myocardial tracking and strain estimation methods using MRI and validated against the benchmark framework (Tobon-Gomez, Craene, Mcleod, *et al.*, 2013). The benchmark framework has provided an open-access 3D dataset, a set of validation methods, and results of four leading methods for comparison. Validation methods include qualitative and quantitative methods. The benchmark framework provides the steps for qualitative assessment of outcomes and verified ground truth for quantitative assessment of results.

Such novel tools and methods could provide an accurate diagnosis. Moreover, safety and convenience could be ensured while diagnosing, as it does not involve the usage of GBCA.

1.1.2 Justification for the Research

Drug regulatory agencies, such as the United States Food and Drug Administration (FDA), ensure standards and safe drugs usage. Official reports and publications of rigorous clinical trials provide details of the drug usage. The current clinical gold-standard of diagnosing cardiac patients involves LGE imaging (Pennell, Sechtem, Higgins, *et al.*, 2004). LGE imaging provides sufficient accuracy. However, safety concerns such as adverse incidents of deaths, allergic reactions, and gadolinium deposition in brain tissues, are raised and found in the literature (Ergün, Keven, Uruç, *et al.*, 2005; Bruder, Schneider, Nothnagel, *et al.*, 2011; Nacif, Arai, Lima, *et al.*, 2012; Kanal and Tweedle, 2015; McDonald, McDonald, Kallmes, *et al.*, 2015; Nezafat, 2015). Hence, to improve the quality of patient treatment and care, clinical

experts need innovative tools that provide improved accuracy and better safety. Developed tools need to be accurate, safe, feasible and timely for clinical experts, and comfortable for patients while being used.

Therefore, this thesis has addressed the research that could help in contributing a tool for cardiac diagnosis. The fully-developed tool would be utilising material property (i.e. strain) of the cardiac muscle in identifying infarcted myocardium, which could avoid the use of GBCA and LGE. At this stage, this thesis aims to contribute a novel method and show early-stage verifications and validations with the benchmark framework (Tobon-Gomez, Craene, Mcleod, *et al.*, 2013) and associated clinical dataset. The technique would perform myocardial tracking and strain calculation using cardiac MRI. The method would be robust and flexible to be extended from 2D to 3D. Moreover, a clinical dataset of myocardial infarction patients would be used to show the developed method's applicability for the clinical problem of identifying infarcted myocardium. The addressed research would ultimately contribute to creating a tool that can identify infarcted myocardium safely and accurately, i.e. without using GBCA and LGE.

1.1.3 Research methodology overview

This thesis has presented the research methodology in three stages:

- **Stage 1 – Understanding current clinical gold-standard practice**, which involves completing the ethics approval process, a clinical placement at the NHS unit, understanding the clinical diagnosis pipeline, outlining strengths and limitations of current clinical tools through

clinical literature review, and developing clinical research questions.

- **Stage 2 – Developing a technical methodology**, which involves a technical literature review, understanding technical benchmark framework, outlining technical requirements, developing a robust method for myocardial strain calculation

- **Stage 3 – Validation and testing**, which involves selecting clinical data cohort, qualitative and quantitative evaluation of technical methods, a clinical validation using healthy and diseased cohort, and validation through standard diagnostic measure tests.

After evaluating technically and validating clinically, a discussion and conclusion could then be drawn regarding the research's validity.

1.2 Clinical review – cardiac diagnostic tools

In this section, a clinical review of cardiac diagnostic tools, which includes tools in current practice and emerging research tools, is elaborated on their strengths and limitations. This review discusses the practical concerns relating to patient treatment and care quality while diagnosing myocardial infarction patients. GBCA usage is highlighted as the prime safety concern. For reference, Chapter 1 covers the fundamentals of cardiac physiology and pathophysiology, with a specific focus on cardiac chambers, their function and the structure of cardiac wall muscle.

It demonstrates how the current method has limited safety in diagnosing myocardial infarction patients and how emerging techniques can help achieve better safety. The reviews are summarised in Table 1.1 and Table 1.2.

1.2.1 Cardiac physiology and pathophysiology

1.2.1.1 Cardiac chambers and function

The human heart is comprised of four chambers: right ventricle (RV), left ventricle (LV), right atrium (RA) and left atrium (LA). The heart can be visualised as two pumps operating in series: one with RA and RV and another with LA and LV (Katz, 2011). The LV wall has more mass and thickness than other chambers because the LV pumps oxygenated blood at a higher pressure from the heart towards the rest of the body (Guyton and Hall, 2011). The LV cavity has a conical shape, which changes during different cardiac cycle phases (Hawthorne, 1966). The LV tip is called the apex, and the muscular area, near the mitral valve, is called the base. The mitral valve regulates the blood flow and prevents the blood from flowing backwards from the LV to the left atrium.

The cardiac cycle is comprised of two phases: diastole and systole. Diastole is a ventricular relaxation phase, which initiates with isovolumic relaxation followed by rapid blood flow, diastasis and atrial systole. During the early diastole of ventricles, the pressure of ventricles falls, which causes blood to flow into ventricles from atria. A fully loaded LV with maximum volume and the closed mitral valve is the end of the diastole. The ventricular pressure remains lower during the diastole.

The second phase, systole, is a contraction phase, which starts with isovolumic contraction and rapid ejection of blood from LV. Once the mitral valve opens, LV squeezes all the blood out with a higher pressure. This phenomenon is related to the clinical measure, left ventricular ejection fraction (LVEF). The pressure is maximum in the middle of the systole and drops at the end of the systole.

LV systole involves complex mechanics such as rotation, torsion, twist, vertical and horizontal translation. Due to the non-uniform nature of LV mechanics, it is crucial to understand systolic

function while diagnosing a cardiac patient. The American Heart Association (AHA) has provided clinical guidelines to effectively quantify LV into smaller sections (Cerqueira, Weissman, Dilsizian, *et al.*, 2002). The details of the AHA model are explained in Section 1.2.2.3.1.

1.2.1.2 Cardiac wall muscle

The heart wall has multiple layers of fibre bundles: the inner layer is called the endocardium, the middle layer is called myocardium, and the outer layer is called the epicardium. The blood flowing through the heart exposes to the endocardium. The myocardium covers most of the thickness of the heart wall and contains myocytes and connective tissues. Moreover, the myocardium contributes to cardiac tensile strength and stiffness. The epicardium consists of a network of fibro-elastic connective tissues providing a smooth, slippery structure to the surface. The epicardium is continuous with the parietal pericardium. It is a fibrous sac surrounding the heart, providing smooth functioning during a heartbeat (Katz, 2011).

During systole, the subepicardial layer's myocardial fibres move in the left-handed helix direction, the mid-layer fibres move in the circumferential direction, and the subendocardial layer fibres move in the right-handed helix direction (Nakatani, 2011). As a result, the LV base experiences clockwise rotational torque, and the apex experiences counter-clockwise torque during systole.

Coronary arteries supply blood to the LV wall. The major LV coronary arteries are: left coronary artery (LCA); right coronary artery (RCA); and left circumflex (LCx). Blood flow is from the epicardium to the endocardium, via muscular branches that traverse the LV wall. Therefore, the arteries are more vulnerable to narrowing at the endocardial layer due to blood clotting (Katz,

2011). Such blood clotting leads to clinical conditions such as myocardial infarction.

Myocardial infarction patients may have infarcted muscle along with healthy muscle. Infarcted muscle is the oxygen-starved muscle that has lost its ability to contract and relax. Infarcted muscle can be transmural (throughout the cardiac wall) or non-transmural. Large transmural infarcts are likely to alter topography and function in non-infarcted as well as infarcted areas of the ventricle (Pfeffer and Braunwald, 1990). Therefore, identifying infarcted muscle is clinically essential.

1.2.2 Cardiac muscle characterisation

Due to the broader scope of cardiac muscle characterisation methods and their applications, we have narrowed down our literature review's scope by focusing on coronary syndrome and, specifically, myocardial infarction patients.

1.2.2.1 ECG test

A preliminary and useful assessment test for cardiac muscle and function characterisation is a 12-lead ECG test (Martin, Groenning, Murray, *et al.*, 2007). Clinical conditions, such as acute coronary syndrome, with recent chest pain symptoms, require rapid diagnosis regarding the possibility of myocardial infarction to provide timely restoration of blood flow, which can preserve ventricular function and improve the survival of a patient (GUSTO, 1993). In such conditions, ECG remains a cornerstone of assessment due to its simplicity and universal availability (Martin, Groenning, Murray, *et al.*, 2007).

In MI patients, ECG could help to localise the territory of an infarct safely and conveniently. However, the precision in

estimating the size of an infarct using ECG could be limited compared to LGE imaging (Martin, Groenning, Murray, *et al.*, 2007; Goldwasser, Elizari and Bayés de Luna, 2017). After the ECG test, advanced imaging tests are considered for further diagnosis.

1.2.2.2 Imaging tests

1.2.2.2.1 Purpose of different tests

A cardiac patient who presents with the chronic coronary syndrome is referred for advanced imaging tests. These tests aim to assess (i) ventricular function, (ii) ischaemia (inadequate blood flow), and (iii) viability (Flachskampf, Schmid, Rost, *et al.*, 2011).

The available tests are echocardiography (Echo), nuclear imaging (such as single-photon emission computed tomography - SPECT), MRI, computed tomography (CT), and positron emission tomography (PET). Echo is usually preferred in the acute conditions of less than 48 hours of incidence due to its bed-side availability, even though it has low image quality than MRI and operator dependent accuracy (Flachskampf, Schmid, Rost, *et al.*, 2011). SPECT, CT, and PET could provide promising diagnostic results, but they involve radiation exposure due to the modalities' intrinsic nature, which makes them less preferable. MRI usage with a pacemaker or implantable cardioverter-defibrillator patients could be prohibitive (Kalin and Stanton, 2005; Strom, Whelan, Shen, *et al.*, 2017). However, in routine patients, MRI could be an imaging modality of choice, as it provides good quality images and utilises non-ionising radiation to capture images.

Within an MRI test, (i) cine MR images are used to visualise ventricular function, myocardial thickness, estimate LVEF, and detect any morphological abnormalities (Flachskampf, Schmid,

Rost, *et al.*, 2011); (ii) ischaemia could be captured through a pharmacological stress test (Chotenimitkhun and Hundley, 2011); (iii) viability test helps in determining the ability of the myocardium to live, which involves determining hibernating myocardium and identifying infarcted myocardium (myocardium with irreversible damage). Infarcted myocardium could be identified with high accuracy and sensitivity through LGE imaging (Pennell, Sechtem, Higgins, *et al.*, 2004).

However, LGE imaging has limited patient safety in identifying infarction. Therefore, the research scope is narrowed down to critically reviewing different tests in identifying infarctions, as described in Section 1.2.2.2.2.

1.2.2.2.2 Identifying infarction – review

Current clinical practice in identifying myocardial infarction includes LGE imaging, due to its higher accuracy and sensitivity (Pennell, Sechtem, Higgins, *et al.*, 2004). LGE is reported to provide such precision that it could detect sub-endocardial infarct, when the SPECT report was normal (Wagner, Mahrholdt, Holly, *et al.*, 2003). Manual injection of GBCA is given to the patient in a typical LGE imaging for a delayed enhancement. Then LGE scan sequences are performed before the gadolinium washes out from the myocardium. Gadolinium concentration in the infarcted myocardium washes out slowly, compared to healthy myocardium, and shows infarcted myocardium with bright intensity in the MR images.

It is recommended that the scan should be performed within 10-30 minutes after injecting gadolinium to acquire good quality images (Vogel-Claussen, Rochitte, Wu, *et al.*, 2006; Franco, Javidi and Ruehm, 2015). Scanning sequences take approximately 6-9 minutes (Captur, Lobascio, Ye, *et al.*, 2019), and a complete LGE imaging takes about 18-22 minutes.

In 2006, a clinical study of 9 end-stage renal disease patients had revealed that five out of nine patients developed nephrogenic fibrosis in 2-4 weeks after the injection of GBCA for an MR scan (Grobner, 2006). A subsequent study of 7 patients has confirmed that gadolinium is detectable within 4 of 13 tissue specimens of patients with nephrogenic systemic fibrosis (High, Ayers, Chandler, *et al.*, 2007). More studies have reported the relation of gadolinium deposition within tissues in different patient conditions (McDonald, McDonald, Kallmes, *et al.*, 2015). Moreover, gadolinium deposition in brain and bone of normal renal patients (Kanal and Tweedle, 2015) is reported due to GBCA administration. LGE is also said to have limited accuracy in conditions like diffuse myocardial fibrosis (Bleumke and Pattanayak, 2015). It is reported that LGE imaging causes additional cost, time and inconvenience due to safety concerns (Nezafat, 2015). An MRI cost-effectiveness study has reported that the GBCA usage increases approximately to €50 per patient (Boldt, Leber, Bonaventura, *et al.*, 2013).

T1-weighted mapping (native T1, post-contrast T1, extracellular volume-ECV) are emerging and promising modalities in viability assessment (Taylor, Salerno, Dharmakumar, *et al.*, 2016). Clinical studies with swine (Cui, Wang, Lu, *et al.*, 2018) and canine (Kali, Cokic, Tang, *et al.*, 2014) have reported good performance of native T1 (T1 mapping without the usage of GBCA) in identifying infarction compared to LGE. A clinical study, performed at 3T with human participants (Kali, Choi, Sharif, *et al.*, 2015), showed that the native T1 mapping has high specificity and modest sensitivity in detecting chronic myocardial infarction. Moreover, post-contrast T1-weighted mapping is also reported with infarction patients (Messroghli, Walters, Plein, *et al.*, 2007), but post-contrast and ECV imaging involves GBCA usage and are widely reported with cardiomyopathy and diffuse fibrosis conditions (Taylor, Salerno, Dharmakumar, *et al.*, 2016). Native

T1 does not require GBCA, and therefore, it can be promising to patient-safety compared to LGE. The patient-scanning time of the T1 mapping scan could remain similar to LGE (Taylor, Salerno, Dharmakumar, *et al.*, 2016).

In emerging methods, strain-based identification of myocardial infarction is a promising method that can be performed through imaging tests or image analysis tests (Mangion, McComb, Auger, *et al.*, 2017). An imaging test directly produces images of myocardial strain maps at the scanner. In contrast, an image analysis test requires image processing tools to create a myocardial strain map using a separate computer.

A typical strain-based method estimates the mechanical strain in cardiac wall muscle during a cardiac cycle to show reduced strain in the infarcted muscle. Clinical studies have shown promising results. However, the accuracy varies among vendors and imaging modalities (Mangion, McComb, Auger, *et al.*, 2017). Echo-based strain methods could be more suitable in diagnosing acute conditions, due to the bedside availability of Echo (Flachskampf, Schmid, Rost, *et al.*, 2011) and lower image processing time (Crosby, Amundsen, Hergum, *et al.*, 2009). In chronic conditions, MRI-based strain methods could be more suitable, while diagnosing, due to good quality images (Flachskampf, Schmid, Rost, *et al.*, 2011) and detailed acquisition of the cardiac wall structure (Moore, Lugo-Olivieri, McVeigh, *et al.*, 2000). Radiologist's analysis time, which is defined as the time required to identify myocardial infarction directly at the scanner or using image processing tools, could vary according to the utilised imaging modality and could be higher in image processing methods compared to LGE imaging. A specific review of strain-based methods is provided in Section 1.2.2.3.3.

These tests for identifying myocardial infarction are summarised in Table 1.1.

Table 1.1 | Strengths and limitations of methods in identifying myocardial infarction.

	Accuracy		Safety	Assessment time and stress			Main Strengths	Main Limitation
	Accuracy	Reproducibility	Patient safety	Patient scanning time	Contrast agent injection requirement	Senior supervision requirement		
Current Practices								
ECG	▽	★	★	★	★	★	Safe, Universal availability	Limited accuracy
LGE	★	★	▽	○	○	○	High accuracy	Limited safety
Emerging Practices								
T1- and T2-mapping	▽	▽	★	○	★	★	Safe	Limited accuracy
Strain analysis	▽	▽	★	▽	★	★	Safe	Limited accuracy

Accuracy: ★ High ▽ Moderate ○ Limited

Safety: ★ High ▽ Moderate ○ Limited

Assessment time and stress: ★ Limited ▽ Moderate ○ High

1.2.2.3 Strain-based characterisation

1.2.2.3.1 Definition of standard AHA model

AHA has standardised the segmentation and nomenclature for cardiac imaging (Cerqueira, Weissman, Dilsizian, *et al.*, 2002) to maintain consistency among global clinical practices and research. According to the AHA model, LV muscle and cavities can be captured in short-axis (SAX) and long-axis (LAX) planes. Standard SAX planes are (i) basal (at tips of the mitral valve leaflets), (ii) mid-ventricular (at papillary muscle), and (iii) apical (lower than papillary muscle and prior to the cavity end). Each of the SAX planes is further divided into 6, 6, 4 segments, respectively. The names of the segments are mentioned in Figure 1.1. For further details, please refer to the article (Cerqueira, Weissman, Dilsizian, *et al.*, 2002). Some of the models consider the apex as the 17th segment. In our work, we have followed the 16-segment model.
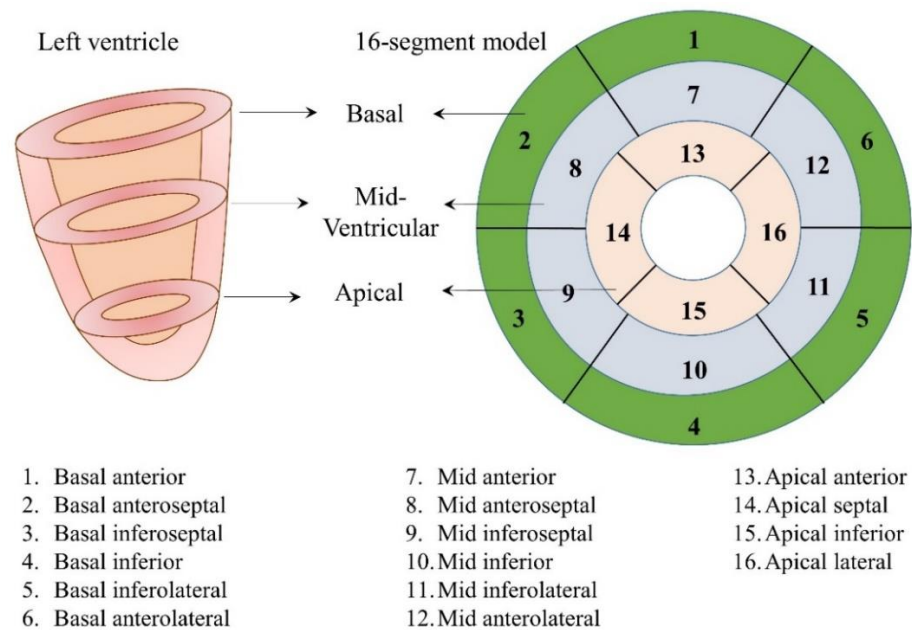
Figure 1.1| 16-segment AHA model of a human left ventricle according to the guidelines of (Cerqueira, Weissman, Dilsizian, *et al.*, 2002; Selvadurai, Puntmann, Bluemke, *et al.*, 2018). Three short-axis slices - basal, mid-ventricular and apical are shown with corresponding AHA defined segments of LV. Basal refers to the slice near the mitral valve and before the beginning of the papillary muscle, mid-ventricular refers to the slice at the approximate middle of the papillary muscle length, and apical refers to the slice beyond the papillary muscle and towards the apex but above the apex.

1.2.2.3.2 Definition of strain

Strain is a measure of deformation. In layman's words, strain quantifies how much an object has shortened or lengthened compared to its original dimensions. There are multiple technical definitions of strain in the literature. We have followed the Lagrange strain (Lai, Rubin and Krempl, 2010) definition. It is widely used and adopted in the framework of myocardial strain-based characterisation methods (Tobon-Gomez, Craene, Mcleod, *et al.*, 2013).

In the context of LV, commonly used directions of strain are circumferential, longitudinal, and radial. In general, diagnostic tools calculate Lagrange strain and project them in the respective directions. A detailed formulation of strain calculation is provided in the relevant sections of the methods chapters.

1.2.2.3.3 Strain-based methods – Review

This section has reviewed strain-based methods, by considering structural details of deformation within the cardiac wall; a technical review of the myocardial strain calculation is provided in Section 1.3.

Strain-based methods are reported with Echo as well as MRI. Among them, Echo-based methods are tissue Doppler imaging (TDI) (Zhang, Chan, Yu, *et al.*, 2005) and speckle tracking echocardiography (STE) (Crosby, Amundsen, Hergum, *et al.*, 2009). MRI-based methods are strain encoding (SENC) (Oyama-Manabe, Ishimori, Sugimori, *et al.*, 2011), displacement encoding with stimulated echoes (DENSE) (Miyagi, Nagata, Kitagawa, *et al.*, 2013; Kihlberg, Haraldsson, Sigfridsson, *et al.*, 2015), harmonic phase contrast (HARP) (Wong, Leong, Weightman, *et al.*, 2014), cardiac magnetic resonance-feature tracking (CMR-FT) (Khan, Singh, Nazir, *et al.*, 2015), and tissue tracking (Gavara, Rodriguez-Palomares, Valente, *et al.*, 2018).

Tissue Doppler imaging is a real-time strain and strain rate imaging method that is promising in identifying infarction (Zhang, Chan, Yu, *et al.*, 2005). As it is Echo-based, it is a convenient imaging method but suffers from low image quality, which limits its accuracy. It is also sensitive to the Echo operator as the accuracy is highly dependent on the direction of ultrasound probe lines.

STE is an Echo-based image processing method, which tracks the inherent pattern of speckles in Echo images (Crosby, Amundsen,

Hergum, *et al.*, 2009). Speckles are intrinsic features of ultrasound imaging, which generate due to sub-resolution scatterers. These speckles are deterministic. However, they change when the myocardial structure deforms during a heartbeat or when the angle between the myocardium and ultrasound wave changes (Meunier, 1998). The method is promising in separating infarcted myocardium from healthy myocardium (Sjøli, Ørn, Grenne, *et al.*, 2009). However, the speckle pattern generates at the boundaries of the myocardium and not within the myocardium. Therefore, the accuracy of the calculated strain remains limited to the boundary. Moreover, the speckle pattern does not remain stable, which may cause measurement error in strain values (Voigt, Pedrizzetti, Lysyansky, *et al.*, 2015).

SENC, DENSE and HARP are reported as promising methods in identifying infarction (Oyama-Manabe, Ishimori, Sugimori, *et al.*, 2011; Miyagi, Nagata, Kitagawa, *et al.*, 2013; Wong, Leong, Weightman, *et al.*, 2014). These methods utilise phase-contrast and myocardial tagging to track cardiac motion and estimate strain values. SENC has a novel advantage of quantifying vertical LV movement in SAX images (Osman, Sampath, Atalar, *et al.*, 2001), whereas DENSE and HARP are advantageous in tracking horizontal LV movement. They can combine and utilise each other's technical framework (Osman, Sampath, Atalar, *et al.*, 2001) to incorporate through-plane motion and estimate 3D strain. However, this approach of merging 2D technical methods to develop a 3D technical method could limit their accuracy of 3D strain calculation, as they are intrinsically developed for 2D.

CMR-FT and tissue tracking are emerging strain methods in identifying infarction using cine MRI (Khan, Singh, Nazir, *et al.*, 2015; Gavara, Rodriguez-Palomares, Valente, *et al.*, 2018). As they use cine MRI, they could be faster in processing, but they do not

include structural deformation within the myocardium, which could limit their accuracy (Mangion, McComb, Auger, *et al.*, 2017). CMR-FT and tissue tracking use cine MRI for strain calculation. CMR-FT uses the endocardium to calculate strain, and as an extension, tissue tracking also uses epicardium along with the endocardium (Mangion, McComb, Auger, *et al.*, 2017). Tissue tracking can include points within the myocardium. However, these structural deformation points cannot be as realistic as grid tagging MRI (Moore, Lugo-Olivieri, McVeigh, *et al.*, 2000). Grid tagging MRI can capture more details of structural deformation within LV myocardium than cine MRI.

Table 1.2 summarises the strain-based methods in identifying infarction.

46

Table 1.2| Comparison among strain-based methods in identifying infarcted myocardium.

	Imaging modality	Considers endocardium	Includes thorough myocardium	Effective for horizontal LV movement	Effective for vertical LV movement	A large number of data samples	Effectively includes strain from all systolic frames	Main Strengths	Main Limitation
Tissue Doppler	Echo	★	▽	★	★	★	○	Faster, 3D	Limited myocardium
Speckle Tracking	Echo	★	▽	★	★	★	○	Faster, 3D	Limited myocardium
Strain Encoding-SENC	MRI	★	★	▽	★	▽	○	Whole myocardium	2D
Harmonic Phase Contrast-HARP	MRI	★	★	★	▽	▽	○	Whole myocardium	Natively 2D (3D extension is limited to the tissue properties knowledge)
Displacement Encoding with Stimulated Echoes-DENSE	MRI	★	★	★	▽	★	○	Whole myocardium	2D
Feature Tracking-FT	MRI	★	○	★	★	★	○	Faster	Limited Myocardium
Tissue Tracking	MRI	★	▽	★	★	★	○	Faster	Limited Myocardium

★ Yes   ▽ Limited   ○ No

1.2.3 Discussion

In this review, various diagnostic tools are scrutinised from the clinical perspective, including the issues of accuracy, safety, and patient care. Diagnostic tools with different imaging modalities are inspected and summarised in Table 1.1 to investigate patient safety and care challenges. It is found that the current LGE imaging is highly accurate. However, LGE requires gadolinium-based contrast agent usage which could cause allergic reactions. This limiting factor could be improved through other imaging modalities. However, other imaging modalities have limited accuracy, as highlighted in Table 1.1. Therefore, in Table 1.2, strain-based diagnosis tools are examined to show the emerging methods' accuracy and robustness. It is found that some of the methods are less accurate due to limited details of structural deformation within the myocardium, and some of the methods are less accurate due to limited technical advancements. The following sections discuss diagnostic imaging tests.

1.2.3.1 Discussion of imaging tests

LGE is preferred due to its accuracy, but clinical studies have emphasised patient safety issues concerning advanced renal impairment patients due to the risk of nephrogenic systemic fibrosis (McDonald, McDonald, Kallmes, *et al.*, 2015). In such conditions, patients could not be offered LGE. Moreover, the gadolinium deposition within healthy subjects' tissues raises concerns in terms of patient care (McDonald, McDonald, Kallmes, *et al.*, 2015). Such deposition is unrelated to age, death, GBCA exposure, and renal sufficiency. Moreover, such deposition's clinical significance is not fully understood yet (Kanda, Matsuda, Oba, *et al.*, 2015; McDonald, McDonald, Kallmes, *et al.*, 2015), which limits the current clinical practice of LGE imaging. In the

literature, clinical experts have also reported similar concerns (Nezafat, 2015), and a minor concern is also reported regarding the higher diagnostic cost due to GBCA (Boldt, Leber, Bonaventura, *et al.*, 2013). As reported in Section 1.2.2.2.2, emerging methods, such as T1-weighted mapping and strain imaging, are promising for safety, but further technical improvements are required to provide as good accuracy and reproducibility as LGE imaging.

Moreover, patient scanning time of T1-mapping and cardiologist analysis time is limited in strain-based methods. However, as these methods are safe, there is a strong motivation to develop faster acquisition and analysis methods further. The advantages and limitations of the categories of methods, mentioned above, are shown in Table 1.1.

1.2.3.2 Discussion of strain-based characterisation

In this review, the specific cardiac anatomy is summarised from the clinical literature to show the myocardium's complexity. These details show that it is crucial to include structural deformation details within the myocardium in the methods. Moreover, the complex vertical and horizontal motion of LV during the systole requires to develop techniques, which are robust in 3D.

A specific explanation regarding strain-based characterisation methods in detecting myocardial infarction is described in Section 1.2.2.3.3. Echo-based methods, such as STE and TDI, could be promising in acute conditions when a faster diagnosis is essential, even though they have limited accuracy. MRI-based methods could be preferable in chronic conditions, when a detailed diagnosis is required.

Within the scope of MRI-based methods, cine MRI-based approaches, such as CMR-FT and tissue tracking, could be promising for a faster analysis in a busy clinical environment. Still, they do not include structural deformation within the myocardium as accurately as grid tagging MRI, thus compromising diagnostic accuracy. Phase contrast and myocardial tagging-based methods, such as SENC, HARP or DENSE, could capture structural deformation within the myocardium, which could be advantageous when diagnosis accuracy is paramount. Moreover, the heart has complex mechanics in vertical and horizontal directions throughout the systolic cycle. Therefore, intrinsically 2D methods, such as SENC or DENSE or HARP, could compromise horizontal or through-plane motion accuracy compared to the 3D methods like 3D STE. Such limitations show a need for an advanced and robust 3D method. Table 1.2 shows the advantages and limitations mentioned above. Moreover, a recent systematic review shows that most of the studies have limited data samples (less than 50) (Mangion, McComb, Auger, *et al.*, 2017), and different vendors have varying strain values even for the same datasets (Mangion, McComb, Auger, *et al.*, 2017), due to different methods and imaging modalities.

1.3 Technical review – Myocardial strain calculation

The previous section has reviewed diagnostic tools in identifying myocardial infarction, including strain-based tools. This section includes a review of the technical literature for the myocardial strain calculation methods. The overview of the myocardial strain calculation pipeline is explained. Then the technical methods are reviewed according to their formulations and 2D or 3D application. The outcome of the review is summarised in Table 1.3. The observations regarding the technical robustness of

existing methods are explained in the Discussion Section 1.3.3 regarding the benchmark framework of myocardial tracking and strain calculation methods.

1.3.1 Overview of myocardial strain calculation pipeline

A typical myocardial strain calculation pipeline involves the following steps: a selection of cardiac imaging, performing myocardial tracking, and formulating strain estimation. These steps are elaborated in the following sections.

1.3.1.1 Cardiac imaging

The selection of cardiac imaging is a crucial step to capture sufficient and relevant anatomical details of the cardiac wall and cardiac cycle. A stack of 2D SAX and LAX images are routinely captured in clinics to assess horizontal and vertical ventricular movements.

Echo has a high spatial and temporal resolution and suitable in emergency conditions, but the image quality is very much dependent on operator skills and patient characteristics (Flachskampf, Schmid, Rost, *et al.*, 2011). Echo images develop an intrinsic pattern of speckle features, which are of prime interest in calculating myocardial strain using tools such as STE (Crosby, Amundsen, Hergum, *et al.*, 2009).

MRI has a high spatial resolution, sufficiently high temporal resolution, and good image quality throughout the cardiac cycle. Researchers develop different types of MRI sequences to capture different kinds of anatomical details. As shown in Figure 1.2, cine MRI shows vessel boundaries (endocardium and epicardium) with a higher contrast, which is a prime interest in calculating myocardial strain using tools like CMR-FT (Hor, Baumann,

Pedrizzetti, *et al.*, 2011). Another cardiac MRI sequence is the grid tagging MRI (McVeigh and Atalar, 1992). As shown in Figure 1.2, grid tagging MRI captures a detailed structure within the myocardium, providing accurate details in calculating strain using tools like HARP (Osman, Kerwin, Mcveigh, *et al.*, 1999).

2D imaging is faster than 3D. However, it could compromise quality in the through-plane motion of ventricles, which could consequent in less accurate strain measurement. This limitation could be overcome by 3D imaging, but it costs in terms of higher acquisition time. For research purposes, 3D Echo and 3D MRI are reported in the literature (Rutz, Ryf, Plein, *et al.*, 2008; Tobon-Gomez, Craene, Mcleod, *et al.*, 2013).
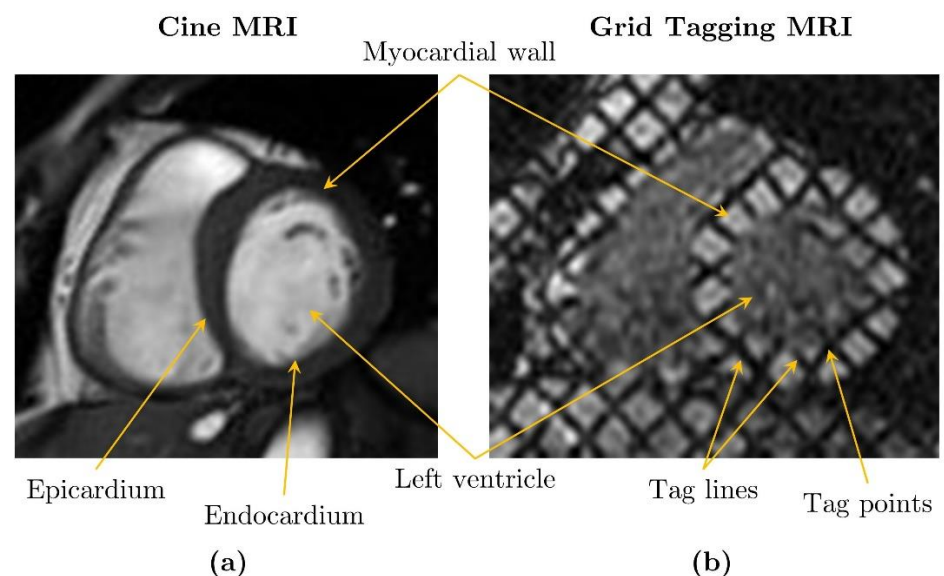
Figure 1.2| Examples of visualising left ventricular myocardial wall in **(a)** cine MRI and **(b)** grid tagging MRI. In **(a)**, cine MRI shows myocardium boundaries (endocardium and epicardium). In **(b)**, grid-tagging MRI shows the details of structural deformation within the myocardium (using tag lines and tag points) better than Cine MRI. Images are from our dataset.

1.3.1.2 Myocardial tracking

After selecting the imaging type, myocardial tracking is the next step for the strain calculation pipeline. Commonly, a cardiac cycle is captured with a sequence of image frames, and each image frame captures the structural deformation of the myocardial wall.

Myocardial tracking methods aim to establish a correspondence among the cardiac frames, in order to track the myocardial structure's deformation during a cardiac cycle. Technical and anatomical details of myocardial tracking methods could vary according to the imaging type.

In Echo imaging, the pattern of speckles provides a means of tracking the myocardium's anatomical change. Tools, such as STE (Crosby, Amundsen, Hergum, *et al.*, 2009), utilise these speckles' locations through automatic or semi-automatic procedures to perform myocardial tracking. In cine MRI, the endocardium and epicardium borders are a means of tracking. Tools, such as CMR-FT (Hor, Baumann, Pedrizzetti, *et al.*, 2011), utilise these borders for myocardial tracking. In tagged MRI, the pattern of tag lines and tag points provide a means of myocardial tracking. Tools, such as HARP (Osman, Kerwin, Mcveigh, *et al.*, 1999), utilise these tag lines and points in a coordinate system to develop a myocardial tracking model.

A detailed review of myocardial tracking methods is provided in Section 1.3.2.

1.3.1.3 Strain estimation

The previous step, myocardial tracking, provides the correspondence among the myocardial structure in each frame of a cardiac cycle. Such information can be used to perform strain estimation.

The strain estimation step aims to estimate a strain tensor at each point of the myocardium. Strain estimation formulation could vary according to the myocardial tracking method. For example, to estimate end-systolic strain, the Echo-based speckle tracking method (Crosby, Amundsen, Hergum, *et al.*, 2009) calculates the distance between two neighbour points in the end-systolic frame and compares it with the distance between the same points in the end-diastolic frame. This comparison is further used to calculate the unit change in length and strain. Another formulation (Abd-elmoniem, Stuber and Prince, 2008; Tobon-Gomez, Craene, Mcleod, *et al.*, 2013) takes each point at the end-systolic frame and estimates its displacement compared to the end-diastolic frame to compute a displacement gradient, which is further used to calculate strain.

After estimating the strain tensor, the strain is projected in circumferential, longitudinal and radial directions, as commonly known in the clinical environment.

1.3.2 Myocardial tracking methods

In the literature, myocardial tracking methods are exhaustively reviewed (Frangi, Niessen and Viergever, 2001; Wang and Amini, 2012). According to our research scope, we have reviewed MRI-based myocardial tracking methods and some of the Echo-based established techniques.

1.3.2.1 Overview of formulation categories

To categorise the technical advancements, the benchmark framework (Tobon-Gomez, Craene, Mcleod, *et al.*, 2013) has highlighted three main formulation categories: (i) Direct

detection-based methods, (ii) Fourier-based methods, and (iii) Tracking-based methods.

1.3.2.1.1 Direct detection-based methods

Direct feature detection-based methods (Young, 1999; Moore, Lugo-Olivieri, McVeigh, *et al.*, 2000) extract specific features from images and then regularize them. These features could be tag points in grid tagging MRI, manually placed fiducial markers, scale-invariant features, landmarks, blobs, corner points or anatomical features, such as valves.

1.3.2.1.2 Fourier-based methods

Fourier-based methods (Arts, Prinzen, Delhaas, *et al.*, 2010; Tautz, Hennemuth and Peitgen, 2011) utilise an imaging property, i.e. a phase shift in the spatial domain is similar to the phase shift in the Fourier domain. This phase shift can be used to estimate the displacement field among cardiac frames to perform myocardium tracking.

1.3.2.1.3 Tracking-based methods

Tracking-based methods (Chandrashekara, Mohiaddin and Rueckert, 2004) utilise image intensity values. A tracking-based model commonly transforms one image into another image by maximizing the similarity matrix and estimating the deformation gradient at each point. This deformation gradient can be utilised for strain estimation, as described in the literature (Abd-elmoniem, Stuber and Prince, 2008).

1.3.2.2 Application-based review

To review the applicability of existing myocardial tracking methods and identify the scope for future research, the existing literature is reviewed in two categories: (i) 2D myocardial tracking and (ii) 3D myocardial tracking.

1.3.2.2.1 2D myocardial tracking

A well-known, commercially available myocardial tracking method is Echo-based STE, which works with 2D and 3D (Manovel, Dawson, Smith, *et al.*, 2010). STE tracks the inherent pattern of speckle features using block-matching techniques. However, Echo images' speckle features are dependent on the scanner manufacturer, and Echo has lower image quality than MRI, which may limit the accuracy of calculated strain (Manovel, Dawson, Smith, *et al.*, 2010).

Direct detection with MRI-based myocardial tracking is reported as promising in the literature. Researchers (Moore, Lugo-Olivieri, McVeigh, *et al.*, 2000) have acquired 2D SAX and LAX images with tag lines in 31 healthy volunteers using a 1.5T scanner of General Electric. A parallel plane tagging method is used in recording sequences of cardiac-gated pulses while holding breath (Moore, Lugo-Olivieri, McVeigh, *et al.*, 2000). The imaging parameters for tagging acquisition are: repetition time is 6.5 msec, echo time is 2.1 msec, phase-encoding steps are 110, bandwidth is $\pm$32-kHz, the temporal resolution of images is 32.5 msec in each subject (Moore, Lugo-Olivieri, McVeigh, *et al.*, 2000). The endocardium and epicardium of LV are identified, and grid lines are tracked using semi-automated software (Guttman, Zerhouni and McVeigh, 1997). The tracking is further used in the displacement field fitting method to calculate the end-systolic strain in circumferential, longitudinal, and radial LV directions. However,

the technique uses parallel planes of tag lines rather than a grid structure of tag lines, limiting the method's accuracy. Gridlines capture horizontal and orthogonal motion in the same MR image, whereas parallel lines capture either horizontal or orthogonal motion of the myocardium in the same image. As a result, grid lines can be more accurate than parallel lines, especially at the intersection points of horizontal and orthogonal grid lines. Such details of intersection points can be helpful to estimate deformation in smaller areas of the myocardium. Amini et al. (2001) have shown the applicability of grid tag lines in myocardial tracking using B-spline models. They acquired 2D long- and short-axis images and reconstructed the LV surface in each phase. The reconstructed surfaces are compared with the reference LV surface to compute the displacement. However, the reference LV surface is assumed as a prolate spheroid, limiting the method, as the shape and size of LV are not thoroughly uniform (Katz, 2011). Remme et al. (2005) have acquired cine MRI (with fiducial markers) and grid tagging MRI. After that, each marker was assigned with motion parameters derived from grid tagging MRI. The whole set of markers was fitted into a finite element model to perform myocardial tracking. Such methods have limited accuracy in temporal alignment between two different imaging modalities, limiting the accuracy of calculated strain. Chen et al. (2010) have developed a myocardial tracking method using specifically grid tagging MRI, which detects and locates tag points using a Gabor filter bank. The technique tracks tag points, using a robust point matching method, and it is advantageous to calculate smooth and local deformation in LV. However, the overall method is only limited to grid tagging MRI.

A Fourier-based method, Harmonic Phase (HARP), is a promising myocardial tracking method (Osman, Kerwin, Mcveigh, *et al.*, 1999). The extensions of HARP are 3D-HARP and zHARP (Pan, Prince, Lima, *et al.*, 2005; Abd-elmoniem, Stuber and Prince,

2008). Fundamentally, the HARP method calculates inverse Fourier transform of the spectral peaks in SAX grid tagging MRI. This calculation is utilized to automatically track myocardial points in a mechanical model. However, the mechanical model consists of a material mesh that retains particular tissue or muscle properties. As these properties are also in emerging research, it may limit myocardial tracking accuracy and calculated strain (Pan, Prince, Lima, *et al.*, 2005). Besides, it is reported in the literature that the HARP underestimates myocardial deformation if there are artefacts in images (Arts, Prinzen, Delhaas, *et al.*, 2010). To overcome HARP's limitations, researchers have proposed another Fourier-based method, Sine Wave Modelling (SinMod) (Arts, Prinzen, Delhaas, *et al.*, 2010). SinMod models local image areas as a part of a sine wave and considered the phase difference and average frequency at each pixel of consecutive cardiac frames to perform myocardial tracking. If the local image area has a low image quality texture, the method automatically considers a larger area. Therefore, SinMod performs better than HARP when images have artefacts or aberration in grid lines (Arts, Prinzen, Delhaas, *et al.*, 2010). However, similar to HARP, SinMod cannot include a through-plane motion for a 3D strain calculation (Arts, Prinzen, Delhaas, *et al.*, 2010). As a 3D extension of SinMod, multiple 2D SAX and LAX slices were combined (Wang and Amini, 2013), limiting the number of LAX slices.

Tracking-based methods can be divided into multiple categories, such as demon-based methods, finite element-based methods, block-matching based methods, and spline-based methods. Well-known demons–based method is Optical Flow, which was initially proposed with tagged MRI images (Prince, Gupta and Osman, 2000), and later adapted for echocardiography images (Angelini and Gerard, 2006). Fundamentally, the demons-based method performs non-rigid image registration by computing

diffeomorphic transformation using velocity field parameters. As a result, it can effectively handle local deformations of the myocardium. However, the method is dependent on Gaussian regularisation rather than biologically motivated regularisation. To resolve this limitation, an improved method, iLogDemons, is developed by integrating elasticity and incompressibility of cardiac muscle (Mansi, Pennec, Sermesant, *et al.*, 2011; McLeod, Prakosa, Mansi, *et al.*, 2012). However, the theoretical knowledge of incompressibility, specifically the local area of incompressibility, is limited in terms of evidence within the literature, contributing towards limiting the accuracy of myocardial tracking (Mansi, Pennec, Sermesant, *et al.*, 2011). Researchers have contributed a finite element-based method, Hyperelastic Warping, for myocardial tracking (Papademetris, Sinusas, Dione, *et al.*, 2002; Veress, Weiss, Klein, *et al.*, 2002). The technique utilises MRI images to calculate force values, and these values are used to deform a finite element geometry of LV end-diastole into end-systole. The results are validated with physiological load and cardiac material properties. However, the estimation of cardiac material properties is an emerging research area, and restricted validation could limit myocardial tracking accuracy. B-spline based models have received considerable attention in the literature because they can handle local and complex deformations with comparatively fewer parameters (Deng and Denney, 2004). These models are based on non-rigid image registration methods, such as free-form deformation (FFD). FFD was initially reported to estimate deformation in breast MRI (Rueckert, Sonoda, Hayes, *et al.*, 1999). The technique was motivated by parametric modelling (Bardinet, Cohen and Ayache, 1996) and image similarity measures, such as mutual information (Maes, Collignon, Vandermeulen, *et al.*, 1997; Rueckert, Hayes, Studholme, *et al.*, 1998). Later, the method was adapted in myocardial tracking and extended with multiple grids

layers, and SAX and LAX cardiac images (Schnabel, Rueckert, Quist, *et al.*, 2001; Chandrashekara, Mohiaddin and Rueckert, 2004; Shi, Zhuang, Pizarro, *et al.*, 2012; Shi, Zhuang, Wang, *et al.*, 2012). FFD is a non-rigid image registration method to relate image points between two images, which provides LV tracking by connecting all the image points among all the cardiac cycle images with each other. To perform image registration, FFD optimises a cost function which is comprised of a similarity measure term and a smoothness term. The similarity measure term is commonly defined with normalised mutual information (Collignon, Maes, Delaere, *et al.*, 1995; Maes, Collignon, Vandermeulen, *et al.*, 1997), which FFD minimizes during optimisation to align intensities between two images. The smoothness term, which FFD maximizes during optimisation, is defined with a transformation function. The transformation function is defined with B-spline based transformation. B-spline and hierarchical B-spline (Schnabel, Rueckert, Quist, *et al.*, 2001) can relate image points in the local image areas. A faster version of FFD, using computer graphics, has contributed with a strategy to simultaneously optimize grid points (Modat, Ridgway, Taylor, *et al.*, 2010). However, FFD has a range of tunable parameters, such as multiple similarity measures, grid spacing in axial directions, multiple grid levels, regularisation function, a combination of various regularisation functions, and a total number of iterations. As a result, the accuracy of FFD is highly dependent on finding these parameter values.

Moreover, due to the regularisation function of FFD, the final calculation of strain values could be underestimated (Tobon-Gomez, Craene, Mcleod, *et al.*, 2013). To overcome this limitation, cine MRI was introduced in the pipeline with FFD (Shi, Zhuang, Wang, *et al.*, 2012). However, it increases an additional dependency of spatial and temporal alignment between cine MRI

and grid tagging MRI (Shi, Zhuang, Wang, *et al.*, 2012), limiting accuracy due to slice misregistration.

CMR-FT utilises cine MRI and performs myocardial tracking by tracking and matching techniques (Hor, Baumann, Pedrizzetti, *et al.*, 2011). Due to the simple approach of CMR-FT, it is promising for faster results in a demanding clinical environment. CMR-FT identifies the boundary of LV in one arbitrary cardiac frame by manual outlining LV border. Such a line represents a set of points. Each of these points is automatically tracked in a hierarchical matching, including 1D tracking methods. In the first step, the line passing through each of these points and the myocardium's transmural cavity are tracked with a cross-correlation matrix. In the second step, each of the border points is independently tracked with 2D windows (matrices) of different sizes (Hor, Baumann, Pedrizzetti, *et al.*, 2011). In these steps, the CMR-FT and cine MRI do not consider the myocardium's structural deformation as accurately as grid tagging MRI does. Hence, CMR-FT tracking can be limited in accuracy compared to the grid tagging MRI-based method's tracking.

With the advancements of imaging methods, 3D cardiac imaging has enabled researchers to develop robust methods to improve strain calculation.

1.3.2.2.2 3D myocardial tracking

In literature, LV is known to shrink, expand, translate vertically, translate horizontally, rotate, and develop twist and torsion during a cardiac cycle (Katz, 2011). As a result, a common complication in the myocardial tracking methods is the inclusion of longitudinal heart movement.

Myocardial tracking methods are initially developed by utilizing a sequence of 2D SAX images over a cardiac cycle at different LV

levels (Radeva, Amini and Huang, 1997). However, this approach is limited to the horizontal movement of LV and is missing vertical or through-plane movement along with the horizontal movement. Later, researchers have combined 2D LAX images with 2D SAX images, in one model, to consider out-plane (through-plane) vertical LV movement (Radeva, Amini and Huang, 1997; Chandrashekara, Mohiaddin and Rueckert, 2004). However, a limited number of LAX images could limit the method. This approach is also prone to misregistration of 2D slices, patient cooperation, and subjective to the radiographer's approach in the conduct of the imaging examination (Rutz, Ryf, Plein, *et al.*, 2008). Later, after the technical advancements of 3D imaging, researchers have acquired 3D volumes over a cardiac cycle and extended their method for 3D (Tobon-Gomez, Craene, Mcleod, *et al.*, 2013). Figure 1.3 shows an example of a stack of 2D SAX images, a combined 2D SAX and LAX images, and a 3D volume of LV.

A stack of 2D short-axis MRI   Left ventricle

(a)

A stack of 2D short-axis MRI

2D long-axis MRI

(b)

3D cardiac MRI   3D left ventricle

(c)
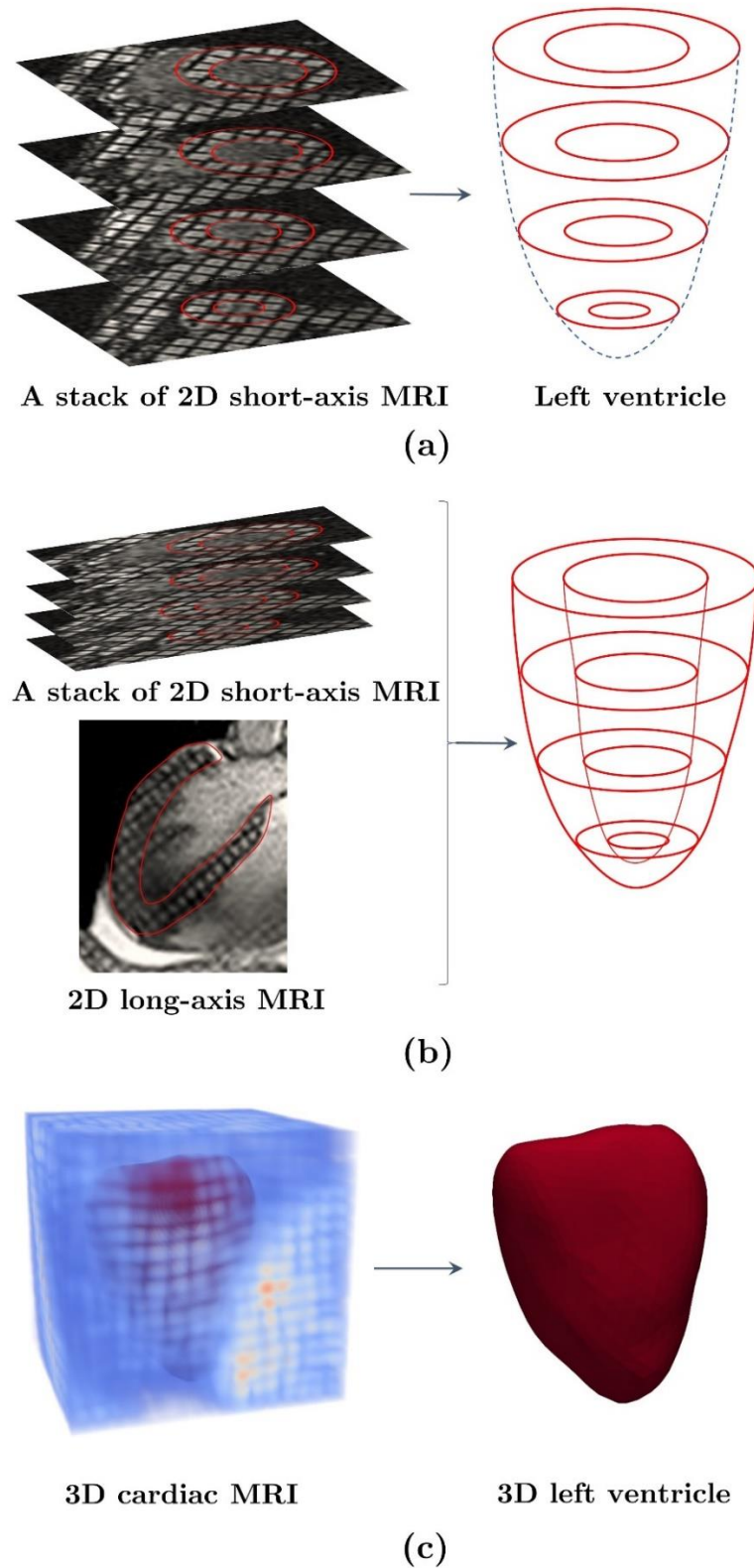
Figure 1.3| (a) A stack of 2D short-axis MRI and LV contours **(b)** A combined 2D short-axis and long-axis MRIs and contours **(c)** 3D cardiac MRI and left ventricle (Bhalodiya, Palit, Ferrante, *et al.*, 2019).

The Fourier-based method, HARP, was initially proposed for 2D imaging. However, the original HARP method could not estimate through-plane 3D motion and strain (Wang and Amini, 2012). For 3D strain calculation, SENC was combined with HARP (Sampath, Osman and Prince, 2013) and SENC with DENSE. Moreover, HARP was extended as 3D HARP by combining a few LAX slices with a stack of SAX slices which enabled the estimation of in-plane and through-plane motion (Pan, Prince, Lima, *et al.*, 2005; Abd-elmoniem, Stuber and Prince, 2008). However, these approaches are prone to misregistration of slices, and strain accuracy is limited to the number of LV slices. Besides, another 3D extension of HARP was proposed by incorporating an original regularisation function, which was based on the anatomical space of coordinates and incompressibility constraints (Zhou, Bernard, Saloux, *et al.*, 2015). This method has reported a similar myocardial tracking accuracy to the benchmark methods (Tobon-Gomez, Craene, Mcleod, *et al.*, 2013). However, the method can be affected by the unrecorded tag points and limited knowledge of local incompressibility constraints (Zhou, Bernard, Saloux, *et al.*, 2015). Tag point jumps refer to the cases in which the grid tagging points are not adequately recorded in some of the images due to technical or scanner limitations, and incompressibility refers to the tissue material property of myocardial tissues.

A Fourier-based method, which Fraunhofer-Institut für Digitale Medizin (MEVIS) (Tobon-Gomez et al., 2013) contributed, is also a promising 3D myocardial tracking method. The MEVIS method is fundamentally based on the Morphon algorithm designed to morph an N-dimensional model onto N-dimensional data in a segmentation task (Knutsson and Andersson, 2005). The MEVIS method estimates 3D displacement by combining 1D displacements in all three directions using quadrature filters. Moreover, displacement calculation is performed iteratively by the accumulation of displacement fields at multiple scales. During

this accumulation, the displacement field is weighted differently for different scales. For example, a higher weight for fine resolution scale compared to coarse resolution scale (Knutsson and Andersson, 2005). The MEVIS method is flexible to adapt different data sets, imaging modalities, and even different anatomies. The method is independent of dimensions, and it can be extended for higher-dimensional images. However, the MEVIS method could accumulate errors, produce large error outliers, and be temporal inconsistent (Tobon-Gomez, Craene, Mcleod, *et al.*, 2013).

A tracking-based method, which is contributed by the National Institute for Research in Computer Science and Automation-Asclepios project (INRIA) (Tobon-Gomez, Craene, Mcleod, *et al.*, 2013), is also a promising method in 3D myocardial tracking. The INRIA method is based on the iLogDemons method (Mansi, Pennec, Sermesant, *et al.*, 2011; McLeod, Prakosa, Mansi, *et al.*, 2012). The method utilizes a regularization function that consists of incompressibility criteria and velocity-based formulation. The INRIA method is flexible to incorporate physiological priors and their constrained values. The method has managed to capture radial strain while using 3D volumes of healthy volunteers. However, the local area of incompressibility is not considered in the method due to limited knowledge of cardiac tissue material properties, which is an emerging research area.

Moreover, the performance of the regularisation function is patient-specific, which could create inconsistent results with different datasets. Such limitations could limit the accuracy of myocardial tracking. Universitat Pompeu Fabra (UPF) has reported a promising 3D myocardial tracking method using the benchmark dataset (Tobon-Gomez, Craene, Mcleod, *et al.*, 2013). The UPF method is based on temporal diffeomorphic free form deformation-based transformation and velocity-based

formulation. The method is robust to handle a low signal to noise ratio and has temporal consistency. However, the approach could over-smooth deformation, underestimating the myocardial strain (Tobon-Gomez, Craene, Mcleod, *et al.*, 2013).

A tracking-based method, which utilised the FFD formulation, is also a promising 3D method. Rueckert et al. (1999) have developed a non-rigid image registration approach, using FFD, for 2D breast MRI. The method is extended for simultaneous registration of 2D SAX and LAX cardiac MRI for myocardial tracking (Chandrashekara, Mohiaddin and Rueckert, 2004). Further, the method is developed for 3D myocardial tracking and strain calculation (Shi, Zhuang, Wang, *et al.*, 2012). 3D extension of this method has reported results with a benchmark framework, as the Imperial College London -University College London (IUCL) method (Tobon-Gomez, Craene, Mcleod, *et al.*, 2013). The method is based on cross-correlation-based FFD, and it is well localised. It also includes automatic segmentation of the LV contours, which is a complementary advantage. However, the method fundamentally uses a bending energy-based regularisation function, which could underestimate the myocardial strain values due to the smoothing effect (Tobon-Gomez, Craene, Mcleod, *et al.*, 2013).

The CMR-FT and tissue tracking methods utilise 3D cine MRI to perform myocardial tracking with matching techniques and be promising in a demanding clinical environment (Schuster, Stahnke, Unterberg-Buchwald, *et al.*, 2015). However, cine MRI may limit the accuracy of calculated strain compared to grid tagging MRI as it does not reflect the structural deformation within the myocardium.

A summary of myocardial tracking methods is provided in Table 1.3.

Table 1.3 | Comparison of myocardial tracking and strain calculation methods.

	Imaging	Formulation	Main technical strength	3D robustness	Main limitation for accuracy
STE	Echo	Block-matching-based tracking	Faster calculation	Good	Operator dependent accuracy
HARP	MRI	Fourier-based material point tracking	Robust to tracking error	Good	Limited to the knowledge of local incompressibility constraints
SinMod	MRI	Signal frequency-based modelling	Robust to image artefacts and noise	Good	Limited number of LAX slices
SENC	MRI	Orthogonal gradient encoding	Effective for through plane motion	Limited	Prone to slice mis-registration for 3D
DENSE	MRI	Phase displacement encoding	Robust in-plane tracking	Limited	Prone to slice mis-registration for 3D
MEVIS	MRI	Elastic-based registration	Flexible to adapt image dimensions	Good	Prone to large error outliers
INRIA	MRI	Demons-based registration	Flexible to include physiological priors	Good	Limited to the knowledge of patient-specific tissue properties
UPF	MRI	Diffeomorphic FFD registration	Robust to higher noise	Good	Underestimates deformation due to regularisation
IUCL	MRI	Intensity-based FFD registration	Robust to error accumulation	Good	Underestimates deformation due to regularisation
FT	MRI	Intensity-based tracking	Does not need regularisation function	Good	Limited consideration of myocardial structure

1.3.3 Discussion

1.3.3.1 Overall pipeline

This section provides an overview of the strain calculation pipeline and a review of myocardial tracking methods. The details of the myocardial wall are highlighted with cine and tagged MRI examples. Cine MRI captures only the endocardium and epicardium efficiently. In contrast, grid tagging MRI captures better myocardial structure and deformation throughout the myocardium, making grid tagging preferable when the accuracy is essential. Grid tagging could be disadvantageous if a patient has difficulties holding their breath while capturing MRI as it may lead to faded texture in MR images.

Moreover, grid tagging MR images could suffer from fading grid lines and grid tagging points. In such conditions, the algorithms which are dependent on grid tagging MR images might not be able to perform accurate myocardial tracking. The gradient-based formulation could be preferable for accuracy in the strain calculation step, as it utilises individual points to calculate strain. Moreover, the formulation is adopted in the benchmark framework to compare existing methods (Tobon-Gomez, Craene, Mcleod, *et al.*, 2013).

1.3.3.2 Myocardial tracking

From the review of myocardial tracking methods, it is observed that the myocardial tracking methods are initially developed for 2D, making them limited to either tracking in-plane motion or through-plane motion. Researchers have combined different 2D images and 2D methods to calculate strain in 3D to overcome such limitations. However, these approaches' accuracy is prone to slice misregistration and limited to the 2D slices' numbers. A similar observation is reported in the literature (Rutz, Ryf, Plein,

et al., 2008). Later, researchers have developed fully 3D myocardial tracking methods, which utilised fully 3D volumes. Researchers have reported their results of 3D myocardial tracking and strain. However, as discussed in the benchmark framework (Tobon-Gomez, Craene, Mcleod, *et al.*, 2013), there is still research scope to improve tracking methods and accuracy. Due to the technical and knowledge-based limitations of existing methods, myocardial tracking's accuracy and consistency are still limited (Tobon-Gomez, Craene, Mcleod, *et al.*, 2013).

From the review summary of Table 1.3, it is observed that the existing myocardial tracking methods have considerable advantages such as being sufficient for 3D cardiac motion, flexible to include physiological priors (priors such as tissue incompressibility, tissue elasticity) and image dimensions, and robust to tracking error and image noise. However, the tracking accuracy of the methods is limited due to various technical and knowledge-based limitations. For example, the UPF and IUCL methods underestimate deformation due to the regularisation function. HARP and INRIA methods have limited accuracy due to the limited knowledge of patient-specific tissue material properties. It is summarised in Table 1.3 that an established Echo-based method and a recent cine MRI–based FT method are technically advantageous over these limitations, as they do not require physiological priors. However, the Echo has lower image quality, and Cine-MRI includes limited myocardial structure deformation within the myocardium. As a result, these methods can give faster results in a demanding clinical environment, but they may limit the accuracy of calculated strain values. Techniques such as IUCL, UPF, HARP, and INRIA could be more promising for the complete inclusion of myocardial structure deformation as they utilise tagged MRI. A summarised table of our review, with key strengths and limitations of the existing methods, is provided in Table 1.3. A detailed list of literature is

provided in Section 1.3.2.2. Furthermore, we have discussed the possible way of overcoming limitations with a novel method in Section 1.3.3.3.

Tracking-based deformable methods, such as the B-spline and FFD-based methods (Chandrashekara, Mohiaddin and Rueckert, 2004), could overcome the limitation of requiring patient-specific tissue properties. However, these methods have dependency of the regularisation function and the tunable parameters associated with them. It is reported that the regularisation function may over smooth the calculated strain and underestimates strain values (Tobon-Gomez, Craene, Mcleod, *et al.*, 2013). Besides, the usage of the B-spline function in myocardial tracking methods is complicated. It is reported in the literature (Deng and Denney, 2004) that the B-spline models, with a Cartesian coordinate system, are prone to ill-conditioned polynomials. Such issues were addressed by including LV periphery measurements (Ozturk and Mcveigh, 2000) and a cylindrical coordinate system with B-spline (Deng and Denney, 2004). However, these approaches could overcomplicate the method and introduce additional dependencies, such as different coordinate systems (Deng and Denney, 2004).

1.3.3.3 Direction for a new method

As the B-spline function has origin in the transformation function literature, we have explored additional literature regarding different transformation functions. It is reported in the literature that the spline-based functions can generate large errors when the spacing among points is irregular (Zagorchev and Goshtasby, 2006), which could happen in myocardial tracking methods due to the non-uniform shape of a cardiac vessel. To overcome the B-spline function's limitations, a local weighted mean (LWM)

function is proposed by (Maude, 1971). LWM is concise and less complicated than B-spline, and it was adapted for the non-rigid image registration of 2D geo-spatial images (Goshtasby, 1988). LWM is an interpolation function that maps corresponding points between two images. For the correspondence establishment, LWM uses locally weighted polynomials passing over the image points. LWM function has a similarity with the human draughtsman method of drawing functions through given points. LWM and its first derivative are continuous at all points for a smooth interpolation (Maude, 1971). LWM has a range of advantages compared to other transformation functions - including spline functions: (i) LWM does not need an extensive system of equations during computation, making it numerically stable (Goshtasby, 1988). It computes transformation by utilizing the coordinates of the corresponding control points. (ii) LWM computation involves averaging weights of control points; therefore; as a result, it can smooth out noise in the correspondences, making it preferable over multiquadratics, spline-based function, and piecewise linear function (Zagorchev and Goshtasby, 2006). (iii) LWM can adapt the density of points by stretching towards the gap, and the derivative of weight function is zero, making it continuous and smooth all over the image (Goshtasby, 1988; Zagorchev and Goshtasby, 2006). (iv) The normalized computation of LWM adapts the local image areas, making it more robust to handle local deformations (Zagorchev and Goshtasby, 2006).

To the best of our knowledge, the LWM function has not received attention from the researchers working on myocardial tracking and strain calculation methods. The LWM function's novel advantages motivate the development of a myocardial tracking method, which incorporates LWM. Moreover, it is reported that block matching-based myocardial tracking is promising with the use of 3D Echo images (Crosby, Amundsen, Hergum, *et al.*, 2009).

However, 3D MRI has received less attention with the block-matching technique (Tobon-Gomez, Craene, Mcleod, *et al.*, 2013), especially with a benchmark dataset.

Such observations motivated this work to develop of a novel method, which creatively performs block-matching and utilises the LWM function to perform 2D and 3D myocardial tracking.

1.4 Research hypothesis/aims

The research problem, which is addressed in this thesis, is as follows:

How can a myocardial tracking and strain calculation tool be developed to calculate myocardial strain to safely and accurately aid diagnostic decisions of myocardial infarction patients?

This thesis argues that a cardiac diagnosis tool can be developed, which can help identify infarcted myocardial segments of the left ventricle. This tool will assist clinical experts seeking to diagnose myocardial infarction patients safely and accurately. This research problem raises the following research questions:

1. How can a 2D myocardial tracking and strain calculation method be developed using the 2D local weighted mean function and structural deformation within the myocardium?
2. How can a 3D myocardial tracking and strain calculation method be developed using the 3D local weighted mean function to calculate 3D myocardial strain?

3. How can 2D circumferential strain of myocardium be used in identifying infarcted left ventricular segments for the diagnosis of myocardial infarction patients?

The aforementioned research questions are addressed in this thesis.

1.5 Summary

This chapter has introduced the research area of diagnosing myocardial infarction patients to address safety issues of LGE imaging. The myocardial strain is identified as a safety measure in identifying infarcted myocardium. Later, in this chapter, the reviews of diagnostic tools, myocardial tracking and strain calculation methods are provided. The reviews' highlighted points are the inclusion of structural deformation within the myocardium and the usage of local weighted mean transformation function for myocardial tracking and strain calculation. Chapter 1 concludes with the thesis's stated research problem and a set of associated research questions. The subsequent chapters of this thesis address each of these research questions.

Chapter 2

Novel Method – 2D Myocardial Tracking

2.1 Introduction

In this chapter, the Hierarchical Template Matching (HTM) method is proposed for 2D myocardial tracking. HTM is independent of tissue material properties. Moreover, the methodology uses the LWM function, as directed in Chapter 1 Section 1.3.3.3, making HTM robust to prevent ill-conditioned polynomials' errors. The method has utilised grid tagging MRI, which is vital to capture structural deformation within the myocardium. Therefore, the calculated strain values reflect the whole myocardium rather than just borders. The proposed method, HTM, is published in a journal article (Bhalodiya, Palit, Tiwari, *et al.*, 2018).

2.2 Proposed HTM method

2.2.1 Overview

The proposed method aims to calculate 2D myocardial strain values. It tracks the myocardium and calculates 2D myocardial strain by following non-rigid image registration. The image registration is performed with "point set", which refers to the set of point locations within the image. The mathematical definitions of each "point set" is further elaborated within Section 2.2.3 and Section 2.2.4. Initially, the LV myocardium is segmented and given as input. After that, as shown in Figure 2.1, image registration of HTM is designed in three steps: (i) retrieving a point set from a moving image, (ii) finding a corresponding point set from the reference image, and (iii) calculating geometric transformation among point sets of moving and reference images.

The reference image is an end-diastolic image of the respective SAX slice. HTM uses local image areas defined as Template, Segment, Chunk and Window, which are pictorially illustrated in Figure 2.2. The word 'part' is used to refer to any of those four words throughout the explanation. The phrase 'target sliding region' refers to the image area of the reference image.
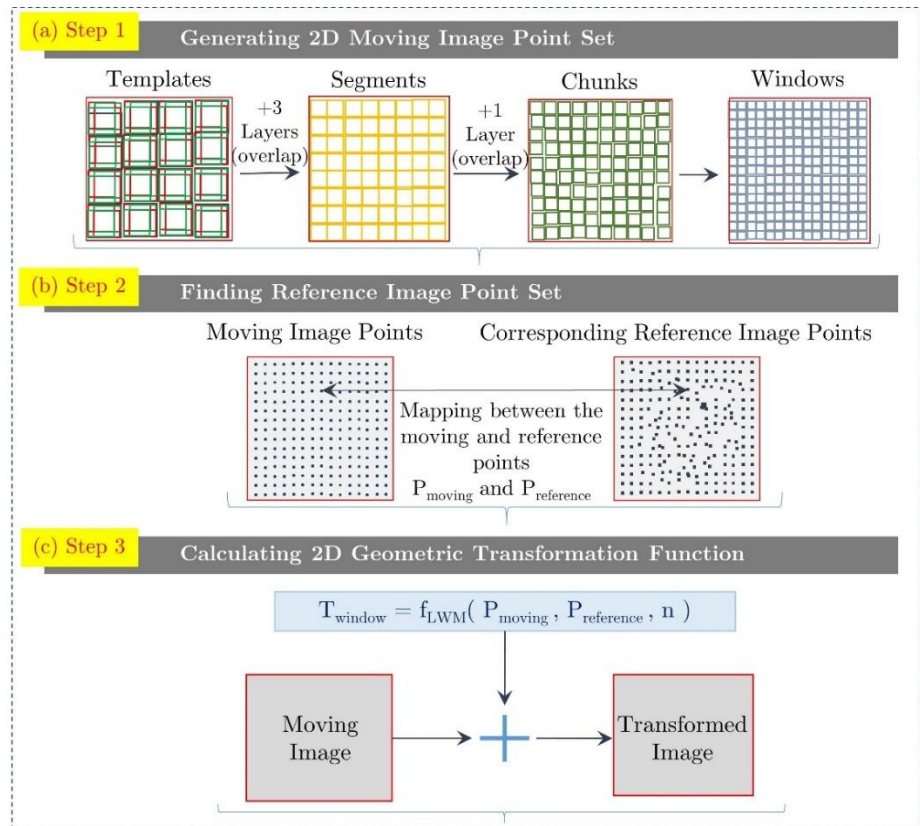
Figure 2.1| Overview of HTM steps to perform image registration in each image pair of a cardiac cycle. **(a)** Step 1 is to generate a moving image point set as defined in Section 2.2.3. **(b)** Step 2 is to find the corresponding reference image point set using the hierarchical template matching process described in Section 2.2.4. **(c)** Step 3 is to perform geometrical transformation using the local-weighted mean function as per Section 2.2.5.
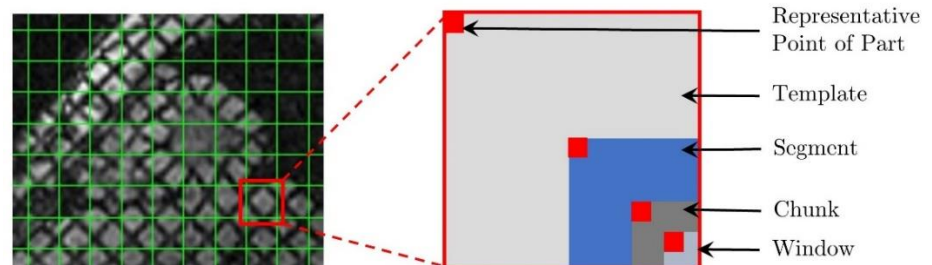
Figure 2.2| Pictorial representation of Template, Segment, Chunk, Window, and Representative Point of a part used in the hierarchical template matching method.

2.2.2 LV segmentation

The entire cardiac cycle is captured with a sequence of grid tagging MRI at different SAX planes of LV. The end-diastolic slice of each SAX plane of LV is manually segmented to identify the LV myocardium. The segmented LV myocardium and original grid tagging MRI are registered using Digital Imaging and Communications in Medicine (DICOM) (Mildenberger, Eichelberg and Martin, 2002) header information. DICOM headers contain imaging-specific information such as coordinate values, which are used during registration. The strain values of this segmented LV myocardium are used while reporting final results.

2.2.3 Retrieving moving point set

This section explains the process to create a point set of moving image points. The moving image refers to any image of the cardiac cycle. The moving image is divided into the image areas of size $t \times t$, which are called Templates. Templates are used to create Segments of size $t/2 \times t/2$. Each Segment is divided into Chunks of size $t/4 \times t/4$. Each Chunk is divided into Windows of size $t/8 \times t/8$. Initially, the value of t is set as 16, which is discussed in the Discussion Section 2.5.2. Accordingly, the parts have sizes as Template 16×16, Segments 8×8, Chunks 4×4, and Windows 2×2. The first point of each part is retrieved in a separate set $M = \{m_1, \ m_2, \ m_3, \dots, \ m_n\}$. Representative point of all Windows collectively defines a dense and uniform point set, which is referred to as a moving point set $P = \{p_1, \ p_2, \ p_3, \dots, \ p_n\}$.

2.2.4 Finding the reference point set

A hierarchical matching structure is used to find reference image points corresponding to the moving image points. Hierarchical

matching is designed with a template matching method using normalised cross-correlation (NCC) (Haralick and Shapiro, 1993; Lewis, 1995). Template matching can be performed by matching an area of one image over the other image's area. This process is commonly referred to as "sliding", and the associated image area of the other image is referred to as "sliding area". NCC algorithm takes two images as inputs and provides a matrix of correlation coefficient (CC) as an output. The range of CC values is from -1.0 to $+1.0$. The highest value in the CC matrix leads to the matching location between the images. The NCC (Haralick and Shapiro, 1993; Lewis, 1995) is adopted as three steps procedure: (i) select each moving image part and determine its relevant cross-correlation with the corresponding sliding area of the reference image, (ii) determine local sums by calculating running sums in advance (Lewis, 1995), and (iii) normalise values of cross-correlation by applying local sums to cross-correlation values which ultimately gives CC matrix.

The overlapping layers are designed as a part of the matching structure, highlighted in Figure 2.1 step 1. Three overlapping layers between Template and Segment layers are designed with parts of sizes 14×14, 12×12, and 10×10. One overlapping layer, between the Segment and Chunk layer, is created, which has parts of size 6×6. The overlapping layers play a crucial role in reducing the sliding area of the reference image during the hierarchical matching process. The mathematical definition of NCC is mentioned in Equation 2.1.

$$\gamma(u,v) = \frac{\sum_{x,y}[f(x,y) - \bar{f}_{u,v}][p(x-u, y-v) - \bar{p}]}{\left\{\sum_{x,y}[f(x,y) - \bar{f}_{u,v}]^2 \sum_{x,y}[p(x-u, y-v) - \bar{p}]^2\right\}^{0.5}}$$

$$(2.1)$$

where f refers to the reference image, $\bar{p}$ refers to the mean of the moving image template, $\bar{f}_{u,v}$ refers to the mean of $f(x,y)$, which is the image area of the reference image under the part of the

moving image. The highest value of $\gamma(u, v)$ leads to the matching location of the reference image area.

A pictorial representation of the hierarchical matching process is shown in Figure 2.3, and the mathematical expression is shown in Equation 2.2 to Equation 2.7. Overlapping layers are not shown, in the pictorial representation, to avoid the overly complicated illustration. However, they are mentioned in the mathematical equations.
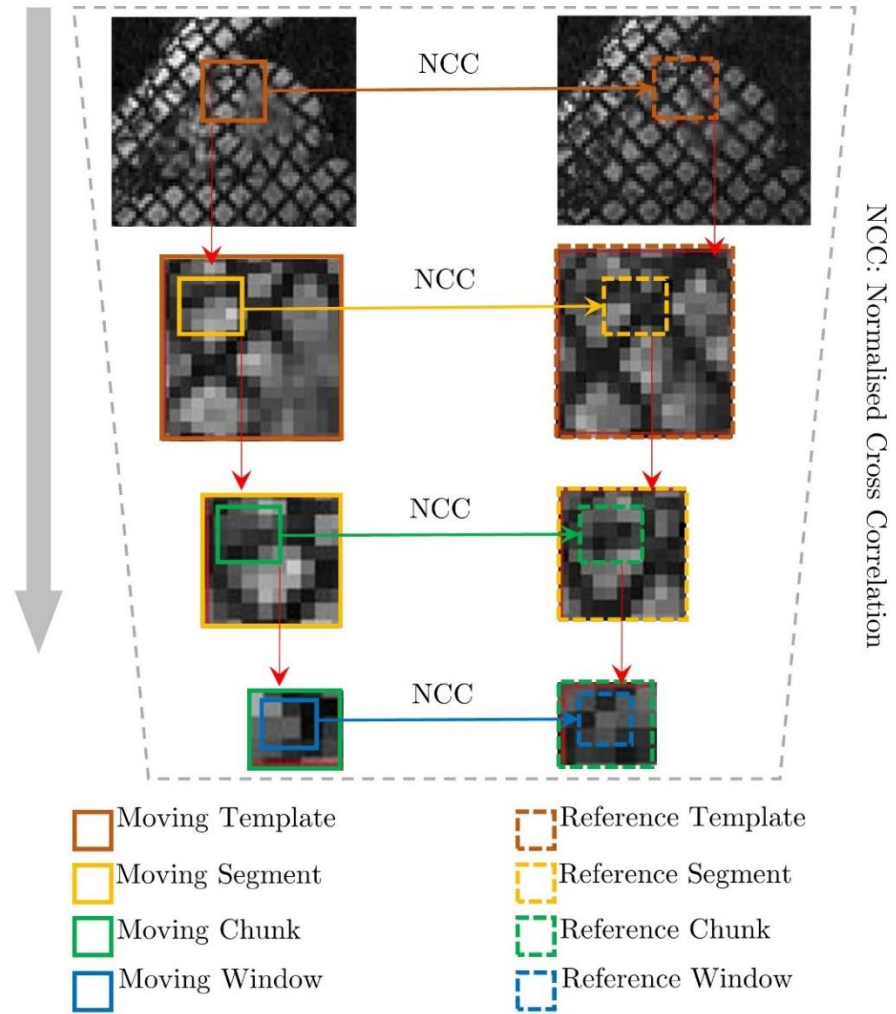
Figure 2.3| Pictorial representation of the hierarchical template matching process using normalised cross-correlation. Pictorial examples of Moving Template, Moving Segment, Moving Chunk, Moving Window, Reference Template, Reference Segment, Reference Chunk, and Reference Window.

The initial step of the hierarchical matching process is to perform NCC between the reference image and the moving image template, which is shown in Equation 2.2.

$$I_M = \sum_{i=1}^{t} MT_i \qquad\qquad RT_i = NCC(MT_i, I_R) \qquad (2.2)$$

where I_M refers to moving image, I_R refers to the reference image, MT refers to moving template, RT refers to reference template, i points to i^{th} template, and NCC is normalised cross-correlation.

Each moving template is used as NCC input for overlapping layers. Equation 2.3 shows the matching process in overlapping layers.

$$MX_{im} \subset MT_i \qquad\qquad RX_{im} = NCC(MX_{im}, RT_i) \qquad (2.3)$$

where MX has a size $(st - 2) \times (st - 2)$, and $st \times st$ is the size of a parent template. MX refers to the moving template section, RX refers to the reference template section, $i = i^{th}$ template, $m = m^{th}$ section of the template, NCC is normalised cross-correlation, MT refers to moving template, RT refers to a reference template.

The process of Equation 2.3 is carried out three times with three different sizes of moving sections. The output RX is used as input to the next step of matching in Equation 2.4. Equation 2.4 performs matching between a reference template section and a moving segment.

$$MT_i = \sum_{j=1}^{4} MS_{ij} \qquad\qquad RS_{ij} = NCC(MS_{ij}, RX_{im}) \qquad (2.4)$$

where RS refers to a reference segment, MS refers to moving segment, RX refers to a reference template section, $i = i^{th}$ template, $m = m^{th}$ section, $j = j^{th}$ segment, NCC is normalised cross-correlation, MT refers to moving template.

Equation 2.5 shows the matching of overlapping layer between segment and chunk layer. Each reference segment and moving segment section are input to NCC to find the output reference segment section.

$$MY_{ijy} \subset MS_{ij} \qquad\qquad RY_{ijy} = NCC(MY_{ijy}, RS_{ij}) \qquad (2.5)$$

where MY refers to moving segment section, RY reference segment section, MS refers to moving segment, $i = i^{th}$ template, $j = j^{th}$ segment, $y = y^{th}$ segment section, RS refers to a reference segment, NCC is normalised cross-correlation.

In Equation 2.6, it is shown that the reference segment section and moving chunk are used as input in NCC to find matching reference chunk.

$$MS_{ij} = \sum_{k=1}^{4} MC_{ijk} \qquad RC_{ijk} = NCC(MC_{ijk}, RY_{ijy}) \quad (2.6)$$

where RC refers to reference chunk, MC refers to moving chunk, RY refers to a reference segment section, MS refers to moving segment, NCC is normalised cross-correlation, $i = i^{th}$ template, $j = j^{th}$ segment, $k = k^{th}$ chunk, and $y = y^{th}$ segment section.

In Equation 2.7, matching the moving window and reference chunk is performed to find a matching reference window. The matching provides a reference window corresponding to each moving window.

$$MC_{ijk} = \sum_{i=1}^{4} MW_{ijkl} \qquad RW_{ijkl} = NCC(MW_{ijkl}, RC_{ijk}) \quad (2.7)$$

where RW refers to a reference window, MW refers to moving window, MC refers to moving chunk, NCC is normalised cross-correlation, RC refers to reference chunk, $i = i^{th}$ template, $j = j^{th}$ segment, $k = k^{th}$ chunk, $l = l^{th}$ window.

The outcome of the reference image point set (P_{RW}) corresponding to moving image point set (P_{MW}) is shown in Equation 2.8.

$$P_{MW} = \sum_{i=1}^{t} \sum_{j=1}^{4} \sum_{k=1}^{4} \sum_{l=1}^{4} MW_{ijkl}(1,1) \, ,$$

$$P_{RW} = \sum_{i=1}^{t} \sum_{j=1}^{4} \sum_{k=1}^{4} \sum_{l=1}^{4} RW_{ijkl}(1,1) \qquad\qquad (2.8)$$

where P_{RW} is reference image point set, P_{MW} is moving image point set, RW refers to a reference window, MW refers to moving window, $i = i^{th}$ template, $j = j^{th}$ segment, $k = k^{th}$ chunk, $l = l^{th}$ window.

The set of matching points is referred to as 'control points' in the next Section 2.2.5, which explains the moving and reference image points' geometrical transformation.

2.2.5 Geometric transformation

This section explains the function to transform all the points of moving image to the reference image points to find the deformation at each point, which can be utilised to calculate strain values further. A radial basis transformation function, LWM, is utilised for transformation. A moving image point set, mentioned in Equation 2.8, is used and referred to as landmarks or control points of moving image during this transformation step. Similarly, the reference image has N control points corresponding to the moving image's N control points. Moving image control points are denoted as (X_i, Y_i), and reference image control points are denoted as (x_i, y_i) in Equation 2.9, Equation 2.10 and Equation 2.11.

$$\{(x_i, y_i), (X_i, Y_i): i = 1, \dots, N\} \qquad (2.9)$$

$$X_i = f_x(x_i, y_i), \qquad Y_i = f_y(x_i, y_i) \qquad (2.10)$$

$$\text{or,} \quad X_i \approx f_x(x_i, y_i), \qquad Y_i \approx f_y(x_i, y_i) \qquad (2.11)$$

where (X_i, Y_i) is a moving image control point, (x_i, y_i) is a reference image control point, N is the number of control points, f is a symbol of function.

The points are organised as tuples in a surface representation, which is shown in Equation 2.12.

$$\{(x_i, y_i, f_i): i = 1, \dots, N\} \qquad (2.12)$$

where (x_i, y_i, f_i) is the ith point, N is the number of control points.

For each ith point, a polynomial which is passing through the point (x_i, y_i, f_i) and its $(n - 1)$ closest neighbour control points are calculated. A weight function is computed at each ith point, as shown in Equation 2.13.

$$W_i(D) = 1 - 3D^2 + 2D^3, 0 \leq D \leq 1$$

$$W_i(D) = 0, D > 1 \qquad (2.13)$$

where $D = [(x - x_i)^2 + (y - y_i)^2]^{1/2}/D_n$ and $D_n =$ distance between (x_i, y_i) and $(n - 1)^{th}$ closest control point, W is the weight function.

Due to the D_n, if the control point has a higher distance from the point, it will have a lesser effect on the transformation, which ensures the local transformation. The derivatives of W with respect to D at locations 0 and 1 are zero. Therefore, the weighted sum at all points remains smooth and continuous. The transformation function at any point (x, y) is defined as mentioned in Equation 2.14.

$$f_{(x,y)} = \frac{\sum_{i=1}^{N} W\left\{[(x-x_i)^2+(y-y_i)^2]^{1/2}/D_n\right\} Poly_i(x,y)}{\sum_{i=1}^{N} W\left\{[(x-x_i)^2+(y-y_i)^2]^{1/2}/D_n\right\}} \qquad (2.14)$$

where $f_{(x,y)}$ is the transformation function at any point (x, y), (x_i, y_i) is a reference image control point, $D_n =$ distance between (x_i, y_i) and $(n - 1)^{th}$ closest control point, W is the weight function, $Poly_i(x, y)$ is the polynomial passing through (x_i, y_i, f_i) and its $(n - 1)$ closest neighbour control points.

2.3 Formulation of strain estimation

This section describes the strain estimation formulas adapted from the literature (Abd-elmoniem, Stuber and Prince, 2008). The strain is estimated by utilising the transformation at each point, as derived in the previous section.

The displacement gradient at each point is calculated with respect to the reference end-diastolic image. Equation 2.15 shows the calculation of the displacement gradient.

$$\nabla U = \begin{bmatrix} U_{xx} & U_{xy} \\ U_{yx} & U_{yy} \end{bmatrix} = \nabla(L_{cur} - L_{ref}) \qquad (2.15)$$

where ∇U refers to the displacement gradient, U_{xx} is derivative of displacement in x with respect to x, U_{xy} is derivative of

displacement in x with respect to y, U_{yx} is derivative of displacement in y with respect to x, U_{yy} is derivative of displacement in y with respect to y, L_{cur} refers to the point coordinates in the current image of the cardiac cycle, L_{ref} refers to the point coordinates in the reference image of the cardiac cycle.

The displacement gradient is utilised to calculate deformation gradient F, which is mentioned in Equation 2.16.

$$F = (I - \nabla U)^{-1} \tag{2.16}$$

where F is deformation gradient, I is the identity matrix, and ∇U refers to the displacement gradient

The deformation gradient is utilised to calculate Eulerian strain tensor E, which is defined in Equation 2.17.

$$E = \frac{1}{2}[I - (FF^T)^{-1}] \tag{2.17}$$

where E is Eulerian strain, I is the identity matrix, F is the deformation gradient

E is projected in the circumferential and radial directions according to the equation $E_p = p^T \cdot E \cdot p$, where p represents a given direction. The definition of projecting strain adopted from the literature (Moore, Lugo-Olivieri, McVeigh, *et al.*, 2000; Tobon-Gomez, Craene, Mcleod, *et al.*, 2013). The longitudinal direction of LV is from the apex to the base, which is defined as L. Accordingly, the radial direction R is perpendicular to the epicardium and pointing outwards, which is defined as $R = M - (M \cdot L)L$, where M refers to the normal of the node. The circumferential direction C is in SAX plane and parallel to the epicardium. It is counter-clockwise when it is observed from the base. C is defined as a cross product of R and L.

2.4 Validation of 2D myocardial tracking

2.4.1 Dataset details

The required institutional ethical approval to conduct research was obtained from the Biomedical and Scientific Research Ethics Committee (BSREC), under the application number REGO 2016-1865. For a thorough understanding of myocardial infarction patients' diagnosis, an Honorary placement at an NHS unit was completed. Data collection from an NHS unit, Royal Brompton and Harefield NHS Foundation Trust (RBHT), was performed to test and validate the technical models, with required ethical approval and official guidelines.

A dataset of 1140 SAX images of 15 healthy human subjects was used to validate the 2D method explained in this chapter. The data acquisition was from a 3T SKYRA of Siemens MRI Scanner, from RBHT, London. The images have pixel sizes of $1.48 \times 1.48mm$ and $1.69 \times 1.69mm$. The data was acquired with steady-state free precession (SSFP) using proper breath holds and ECG-gating. The standard imaging sequence of grid tagging MRI was used for the acquisition with the following sequence parameters: slice thickness 6 (two patients have slice thickness 8), imaging frequency 123.22, number of phase encoding steps 156, repetition time 46.8 (two patients have repetition time 46.44), Echo time 2.46 (two patients have Echo time 2.42), Echo train length 1, Echo numbers 1. As mentioned in Figure 2.4, the data images are from four SAX slices of LV.
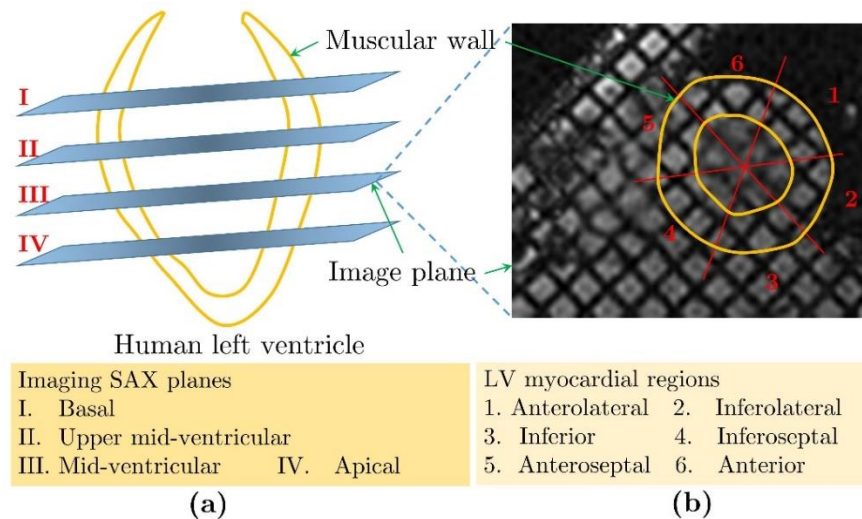
Figure 2.4| **(a)** Four short-axis MRI slices of human left ventricle: basal, upper mid-ventricle, lower mid-ventricle, and apical. **(b)** An example of six regions of left-ventricular myocardium in the mid-ventricular short-axis slice.

2.4.2 Validation methods

The validation is performed by calculating target registration error (TRE) (Fitzpatrick and West, 2001; Chandrashekara, Mohiaddin and Rueckert, 2004) of myocardial tracking and comparing the registration error with the 2D method of one of the benchmark methods (Chandrashekara, Mohiaddin and Rueckert, 2004; Modat, Ridgway, Taylor, *et al.*, 2010).

TRE is adapted as an error measure, which gives root mean square error (RMSE) between corresponding points. In grid tagging MRI, grid points are manually tracked in the whole myocardium, and these locations are used as known ground truth landmarks. After that, the same points are tracked using the 2D HTM method, which are considered tracked landmarks. The distance between locations in each ground truth landmark and the corresponding tracked landmark is calculated as RMSE in millimetre (mm). The mean RMSE is plotted for each LV SAX slice and each phase of a cardiac cycle. Similarly, the mean RMSE using

the benchmark method of free form deformation (FFD) (Rueckert, Sonoda, Hayes, *et al.*, 1999; Chandrashekara, Mohiaddin and Rueckert, 2004) is evaluated.

FFD is a non-rigid image registration method to relate image points between two images, which provides LV tracking by connecting all the image points among all the cardiac cycle images with each other. To perform image registration, FFD optimises a cost function which is comprised of similarity measure term and smoothness term. Similarity measure term is commonly defined with normalised mutual information (Collignon, Maes, Delaere, *et al.*, 1995; Maes, Collignon, Vandermeulen, *et al.*, 1997), which FFD minimizes during optimisation to align intensities between two images. A smoothness term, which FFD maximizes during optimisation, is defined with a transformation function. The transformation function is defined with B-spline based transformation. B-spline and hierarchical B-spline (Schnabel, Rueckert, Quist, *et al.*, 2001) can relate image points in the local image areas. To perform optimisation, FFD has the following tuning parameters, which are selected according to the details of their articles (Rueckert, Sonoda, Hayes, *et al.*, 1999; Chandrashekara, Mohiaddin and Rueckert, 2004): similarity measure is normalised mutual information, regularisation function (smoothness term) is bending energy, the value of bending energy is 0.001, the linear energy term (acts as a weight to the smoothness term) is 0.01, control point grid levels are 3. In the literature (Rueckert, Sonoda, Hayes, *et al.*, 1999), it is mentioned that the accuracy of their method is promising, when the distance between grid points are reduced. Therefore, we selected grid spacing in initial, middle and final levels as 4×4, 2×2 and 1×1. The results are derived and compared with our results.

2.5 Discussion

2.5.1 Strengths

This chapter described a 2D myocardial tracking and strain estimation method that can help mitigate or overcome the technical limitations of existing methods to improve tracking accuracy. The proposed method, HTM, does not require tissue material properties. Moreover, the method is robust to prevent ill-conditioned polynomials' error due to the LWM transformation function. Due to such technical advantages, the accuracy of the myocardial tracking is expected to improve with respect to the benchmark method as these limitations are reported in the literature as factors to the reduced tracking accuracy. The comparative results and validation with the benchmark method are provided in Chapter 6. The method is published in Bhalodiya et al. (2018).

2.5.2 Parameter selection

During the development of this method, in Section 2.2.4, we have considered the size of the template as 16×16. After performing a small in-house Matlab study, we selected this value to understand the accuracy of the template matching algorithm. Templates of different sizes are randomly extracted from grid tagging images of the entire cardiac cycle. The total number of templates for each size is 800. Each of the extracted templates is performed template matching with its corresponding image according to the normalised cross-correlation (Haralick and Shapiro, 1993; Lewis, 1995). The number of templates that have incorrect matchings is counted. The percentage of incorrect matchings with each template size is reported in Figure 2.5.
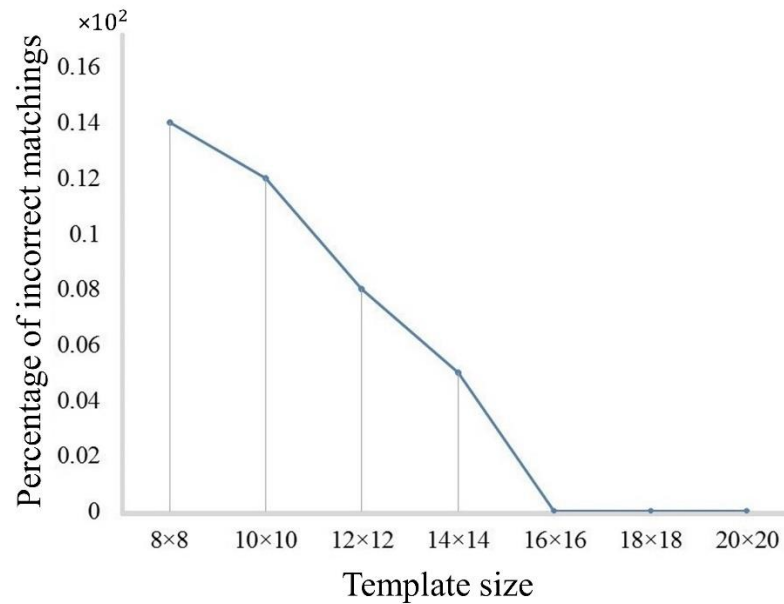
Figure 2.5| The percentage of incorrect matchings for different template sizes are plotted. The template matching is performed with normalised cross-correlation, and the total number of templates for each size is 800. The numbers on the y-axis are multipliers of 100, as shown above the axis (e.g., 0.16×100). Numbers on the x-axis are the number of local points n as defined in Section 2.2.5.

Moreover, in literature, a similar myocardial tracking method (Pedrizzetti, Claus, Kilner, *et al.*, 2016) has mentioned that the value should be at least 8×8 for sufficient accuracy, and another literature (Crosby, Amundsen, Hergum, *et al.*, 2009) noted that the smaller values are vulnerable to inaccurate matching in Echo images. Therefore, after performing the above study with our MRI dataset, we selected the initial template size as 16×16 to maintain size order in our hierarchical matching process. We observe that a higher value may lead to a higher processing time for the method, but it provides better matching accuracy than smaller values.

In Equation 2.13 and 2.14, it is crucial to select the appropriate value of n and accordingly D_n. A too-large value may result in underestimated deformation and strain values, whereas a too

small value may not perform matrix operations. The selection of n is performed after a small in-house Matlab study. n values starting from $n = 5$ up to $n = 150$ with an interval of 5 are tested for 2D error analysis, and it is assumed that the values within them will not significantly reduce target registration error. The process is repeated for randomly selected 10 (out of 15) subjects. 8 out of 10 subjects have the least error at $n = 45$, 1 has the least error at $n = 40$, and 1 has the least error at $n = 35$. An analysis plot for different n values is shown in Figure 2.6.
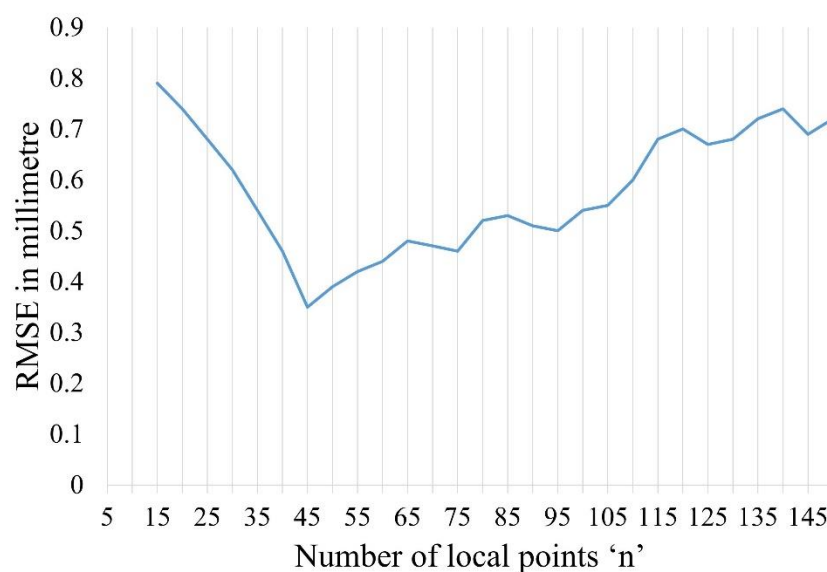
Figure 2.6| Analysis of root mean square error for different n values. n refers to the number of local points for the local weighted mean function, and root mean square error refers to the target registration error. More details of root mean square error values using target registration error are in Section 2.4.2, and the details of the local weighted mean function and local points are in Section 2.2.5.

Moreover, it has been observed in our experiments that the values less than $n = 15$ are giving computation error to proceed, the values between $n = 15$ and $n = 40$ have higher myocardial tracking error which decreases from $n = 15$ to $n = 45$, and values greater than $n = 45$ up to $n = 150$ have higher error compared to

$n = 45$. Therefore, value $n = 45$ was selected for our results, giving the least target registration error.

2.5.3 Limitations

HTM requires a manually segmented myocardium of the initial end-diastolic slice. The accuracy of HTM is sensitive to the selection of initial template size and value of n, which could be considered as limitations of the proposed method. Moreover, if the grid tagging images have faded texture or artefacts due to patient breathing, then the proposed method may cause inaccurate matchings and consequences in incorrect tracking. Such cases may require external smoothing and gives less accurate tracking.

2.6 Summary

In this chapter, a 2D myocardial tracking and strain calculation method, HTM, is described, which follows non-rigid image registration. HTM has three main stages to perform myocardial tracking. After the myocardial tracking, the strain calculation is formulated, which has adapted formulas from the literature. The validation method to examine the tracking accuracy of the HTM method is described. The strengths of HTM compared to existing methods, parameter selection, and limitations of HTM are discussed. The results are reported in Chapter 6. 3D extension of the proposed HTM method is described in Chapter 3.

Chapter 3

Extended Method – 3D Myocardial Tracking

3.1 Introduction

This chapter elaborates on the 3D extension of the HTM method for 3D myocardial tracking and strain calculation. The 3D extension of the LWM function is described, and 3D LWM is introduced in the 3D myocardial tracking pipeline. The validation methods of the benchmark framework for 3D myocardial tracking and strain calculation are described in this chapter. Moreover, the details of an open-access dataset, used to validate the 3D HTM method, are also described. This 3D extension of the HTM is published in a journal article, (Bhalodiya, Palit, Ferrante, *et al.*, 2019).

3.2 Dataset details

An open-access benchmark dataset (Tobon-Gomez, Craene, Mcleod, *et al.*, 2013) of 15 healthy subjects is used for the validation. The dataset contains 3D imaging of healthy subjects and segmented left ventricular volume using end-diastolic cine SSFP MRI. 3D volumes of grid tagging MRI and segmented LV mesh of cine SSFP MRI of each subject are used from the dataset for the 3D HTM method. Grid tagging MRI has a voxel size $0.96mm$ in each dimension. The characteristic details of the dataset are mentioned in Table 3.1.

Table 3.1 | Characteristic details of 3D dataset

ID	Patient	Modality	Age (year)	Sex	Body Surface Area (m²)	Total Cardiac Phases	End-Systolic Frame	Total Number of Slices
1	V1	3DTag	28	M	1.73	22	10	95
2	V2	3DTag	30	F	1.55	28	10	80
3	V4	3DTag	29	F	1.63	25	10	90
4	V5	3DTag	36	M	1.84	22	10	94
5	V6	3DTag	34	M	1.92	22	10	94
6	V7	3DTag	32	M	1.99	30	11	100
7	V8	3DTag	27	M	2.13	30	10	100
8	V9	3DTag	29	M	1.78	29	10	94
9	V10	3DTag	22	M	1.84	26	10	80
10	V11	3DTag	22	M	1.88	31	11	100
11	V12	3DTag	30	M	1.94	23	10	80
12	V13	3DTag	31	M	1.78	37	10	90
13	V14	3DTag	24	F	1.61	28	11	75
14	V15	3DTag	20	M	1.65	20	8	90
15	V16	3DTag	20	M	2.06	24	9	90

3.3 Validation methods – Benchmark framework

Benchmark framework (Tobon-Gomez, Craene, Mcleod, *et al.*, 2013) has provided an open-access dataset and validation methods to assess 3D myocardial tracking and strain calculation algorithms. Moreover, researchers working on biomechanic models have also reported a validation method (Evangelista, Gabriele, Nardinocchi, *et al.*, 2015, 2016; Gabriele, Nardinocchi and Varano, 2015). The validation methods are (i) tracking of ground truth landmarks, (ii) visualising myocardial points' displacement, (iii) performing strain calculation, (iv) analysing the eigenvalue curve.

The first validation method is to calculate myocardial tracking error with respect to the ground truth landmarks. The details of ground truth landmarks are obtained from the benchmark dataset provider (Tobon-Gomez, Craene, Mcleod, *et al.*, 2013).

Twelve landmark points at different anatomical locations of LV are provided. One landmark, per each anterior, septal, posterior and lateral wall at three LV levels basal, mid-ventricular and apical, is provided. These landmarks are tracked using 3D HTM, and the spatial difference between ground truth landmarks and tracked landmarks is calculated at end-systolic frames, at final frames and combinedly at all frames. The error is calculated as Euclidean distance in millimetre, and box-plots of median error are reported compared to benchmark methods. The benchmark framework has used only 12 ground-truth landmark points for an entire LV volume. The points are distributed all over the LV and cover crucial LV anatomical sections, which justifies its use for validity at this stage.

The second validation method is visualising displacement of myocardial points. The displacement is visualised at the end-systolic frame and the final frame. The end-systolic frame should have a higher displacement compared to the final frame. The displacement is calculated as a point-to-surface distance in millimetre, defined as a distance of a point from the end-diastolic surface.

The third validation method is an analysis of myocardial strain values. Myocardial strain at each frame is calculated with respect to the end-diastolic frame. The strain values are plotted as a line graph, and the curve is visualised with respect to the physiological ground truth of LV function, which expects a bell type of shape due to LV contraction and expansion. Moreover, the end-systolic peak is compared with literature (Moore, Lugo-Olivieri, McVeigh, *et al.*, 2000) values.

The fourth validation strategy is eigenvalue analysis adopted from a biomechanics protocol literature (Evangelista, Gabriele, Nardinocchi, *et al.*, 2015, 2016; Gabriele, Nardinocchi and Varano, 2015). At each point of LV myocardium, strain tensor is

calculated, which provided three eigenvalues at each point. Eigenvalues are organised into three sets, and the median of each set is calculated. These median values of each frame are plotted in a curve. The validation is performed by observing the shape of this curve, which should be the bell type of shape, due to the LV contraction and expansion's physiological ground truth.

3.4 Extension of HTM to 3D

3.4.1 Overview

The 3D HTM aims to calculate 3D myocardial strain. 3D HTM can be divided into four steps: (i) segmentation of 3D LV volumes, (ii) 3D hierarchical block-matching, (iii) 3D LWM transformation, and (iv) 3D strain estimation.

3.4.2 Segmentation of 3D LV volumes

Cardiac volumes of the whole cardiac cycle are recorded using grid tagging MRI sequence and steady-state free precession (SSFP) MRI sequence (Schär, Kozerke, Fischer, *et al.*, 2004). Grid tagging volumes are used to perform 3D myocardial tracking, whereas 3D SSFP volumes are utilised to segment end-diastolic LV myocardium. The segmented LV volumes are registered with grid tagging MRI volumes using DICOM header details as suggested by the benchmark framework (Tobon-Gomez, Craene, Mcleod, *et al.*, 2013). An example is shown in Figure 3.1. All the 3D MRI and segmented volumes are collected from an open-access data repository provided by the benchmark framework (Tobon-Gomez, Craene, Mcleod, *et al.*, 2013).

3DTAG MRI volume
(End-diastole)

Segmented LV mesh
(End-diastole)

DICOM header-based volume and mesh registration
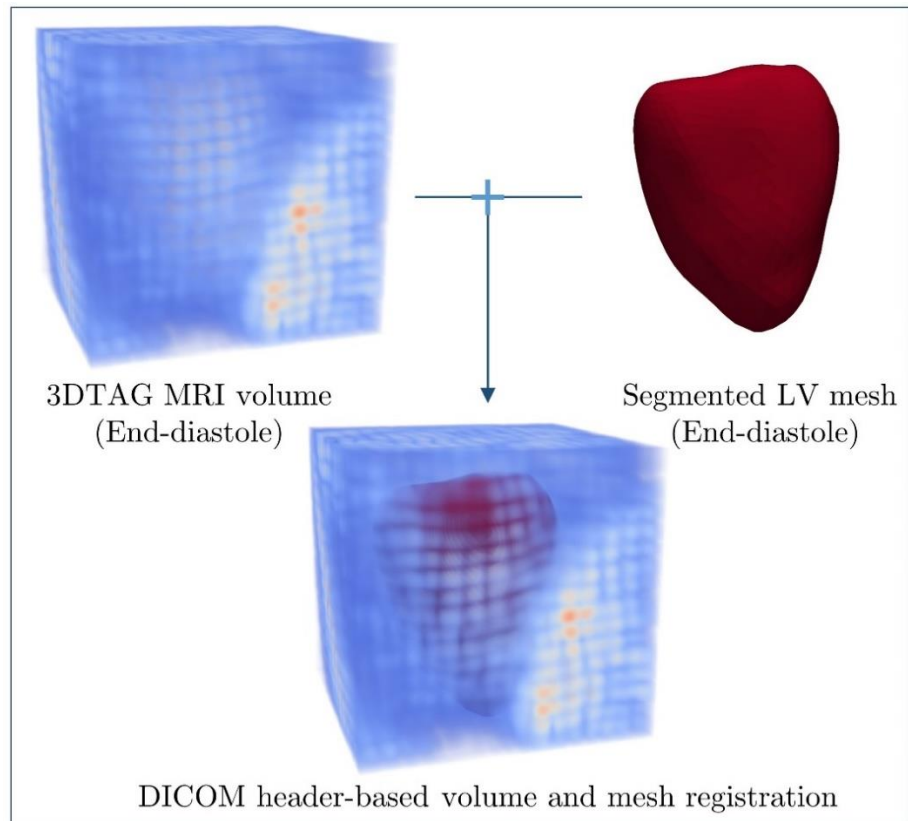
Figure 3.1| An example of registering 3D grid tagging MRI volume with 3D SSFP segmented LV myocardium using DICOM header information.

3.4.3 3D hierarchical block-matching

Figure 3.2 shows the steps of 3D hierarchical block-matching and 3D LWM transformation-based non-rigid image registration between a moving image and a reference image. The reference image is the end-diastolic image, and the moving image could be any cardiac cycle image. The entire process is divided into three steps: (i) selecting a point set from a moving image, which is referred to as a set of control points or landmarks, (ii) finding matching reference image points corresponding to each moving point, (iii) estimating dense transformation function among all moving image and reference image points using sparsely matched control points. The first two steps provide control points and are

explained in this section, and the third step is explained in the next Section 3.4.4.
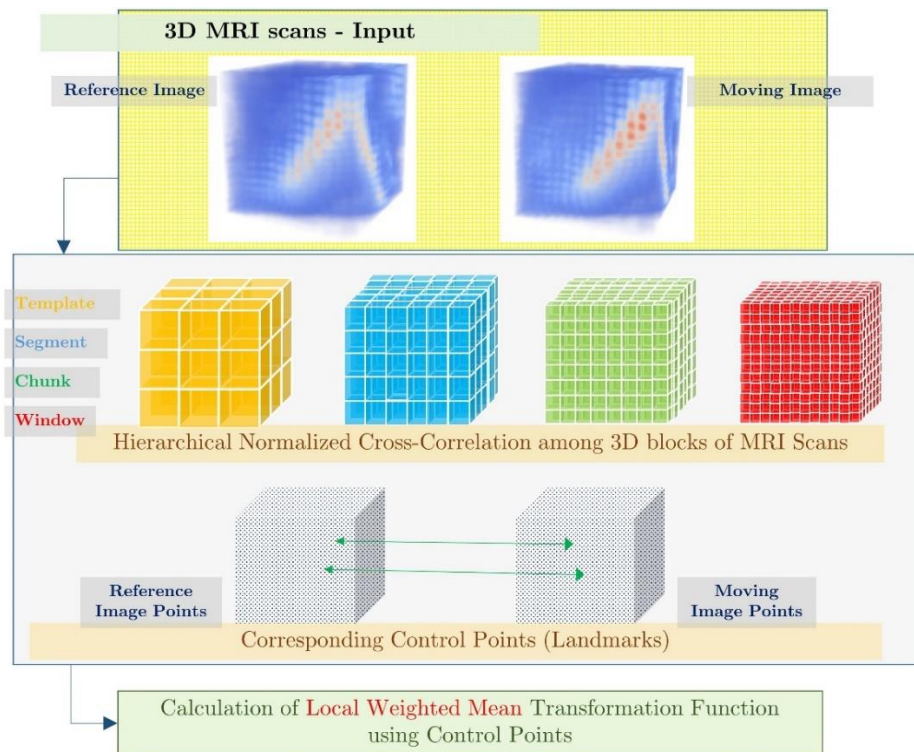
Figure 3.2| Overview of 3D hierarchical block-matching and 3D LWM transformation. 3D MRI of moving image and the reference image are given as input, which are divided into Templates, Segments, Chunks, and Windows to perform 3D Hierarchical Template Matching using normalised cross-correlation. After matching, the derived point sets are performed local transformation using the local weighted mean function.

Selecting a point set from a moving image is performed by dividing the moving image into multiple blocks of size $t \times t \times t$, which provides uniform spacing among points. These blocks are referred to as Templates. Figure 3.3 shows the pictorial definition of these blocks. Each template is divided into eight Segments of size $t/2 \times t/2 \times t/2$. Each segment is divided into eight chunks of size $t/4 \times t/4 \times t/4$, and each chunk is divided into eight windows of size $t/8 \times t/8 \times t/8$. The word 'block' refers to any of the template, segment, chunk, or window interchangeably in this chapter. The first point of each window is defined as a

representative point. The set of representative points is defined as a moving image point set. $P_m = \{m_1, m_2, \ldots, m_n \mid n = total\ number\ of\ windows\}$. The value of t is selected as 16 and accordingly template size as $16 \times 16 \times 16$, which is discussed in the discussion Section 3.5.

3D MRI Scan

■ Template ■ Segment ■ Chunk ■ Window
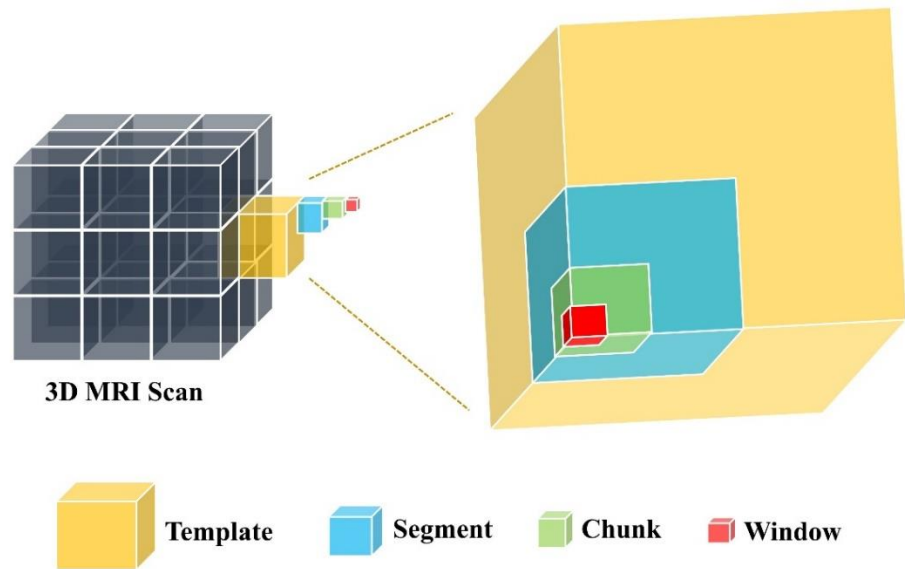
Figure 3.3| Pictorial definitions of 3D blocks: template, segment, chunk and window for the hierarchical matching process.

Matching corresponding reference image points through block-matching is performed hierarchically, as shown in Figure 3.4. 3D NCC is calculated using Equation 3.1 to perform block-matching. NCC gives CC values, and the maximum value of CC is used to find matching block-location. The value of CC ranges from -1.0 to $+1.0$, which shows the worst and the best matching, respectively.
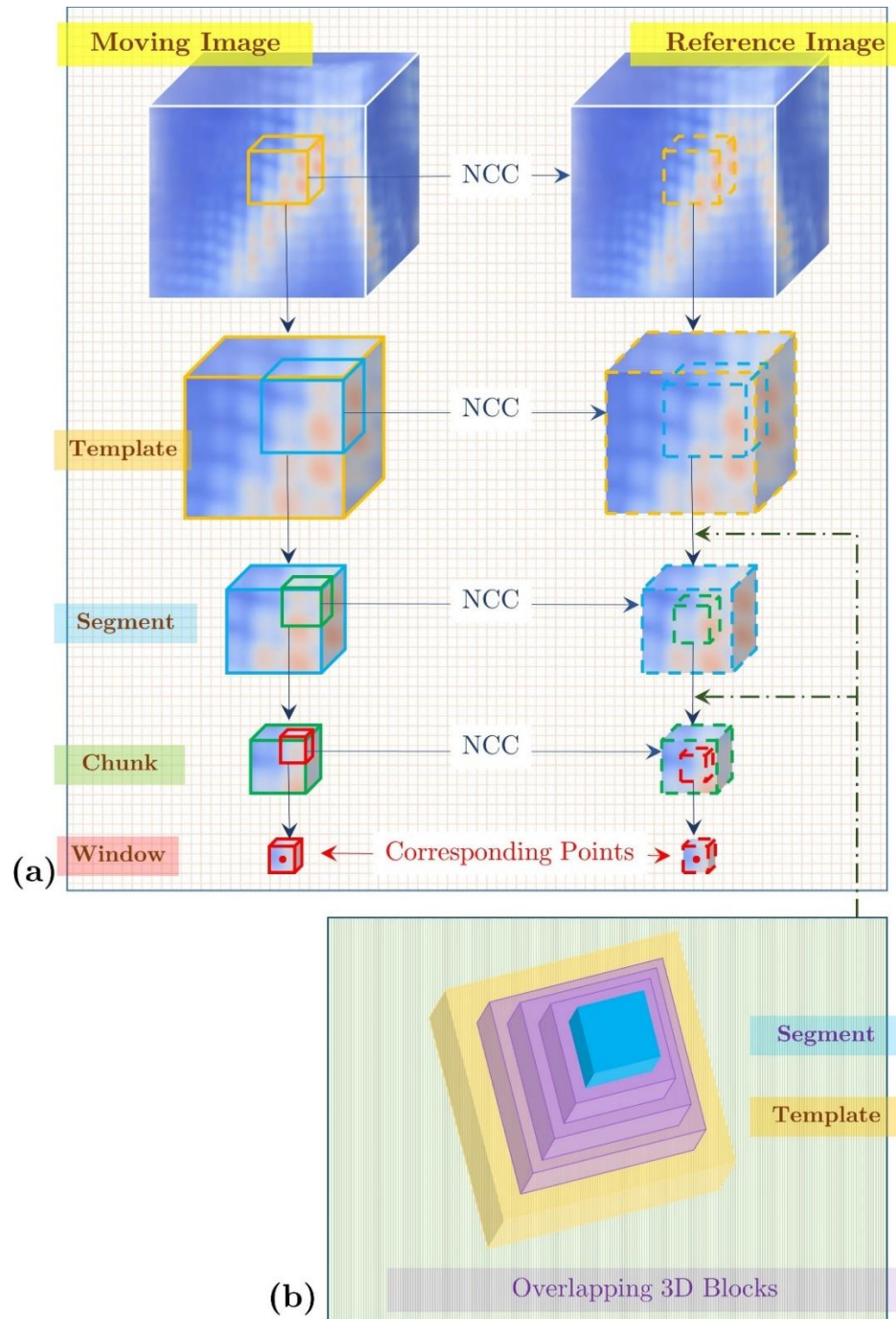
Figure 3.4| Details of hierarchical 3D block-matching process. **(a)** Hierarchical matching between moving image and reference image with 3D Templates, 3D Segments, 3D Chunks and 3D Windows using normalised cross-correlation (NCC) is shown. **(b)** Pictorial representation of overlapping 3D blocks between 3D Template and 3D Segment is shown.

$$\gamma = \frac{\sum \left[f(x,y,z) - \bar{f}_{p,q,r} \right]\left[b(x-p, y-q, z-r) - \bar{b} \right]}{\sqrt{\sum \left[f(x,y,z) - \bar{f}_{p,q,r} \right]^2 \sum \left[b(x-p, y-q, z-r) - \bar{b} \right]^2}}$$

$$(3.1)$$

where b refers to 3D moving block, $\bar{b}$ refers to the mean intensity value of the block b, f refers to the reference image, $\bar{f}$ refers to the mean intensity of the reference image, which is under block b, x, y, z and p, q, r refers to three dimensions in a 3D block.

Each 3D template is slid over the reference image, and CC at each location is calculated as mentioned in Equation 3.1. The maximum CC is used to find a matching 3D template from the reference image. In the next step, each template is divided into eight segments, and each segment is slid over the corresponding parent template of the reference image. The CC value for each segment is calculated at locations of the reference template, and the maximum CC value is used to find the corresponding segment of the reference image. After that, each segment of the moving image is divided into eight chunks, and each of them is slid over the corresponding segment of the reference image. Accordingly, maximum CC values are used to find matching chunks of the reference image. Similarly, each chunk is divided into eight windows, and each window is slid over the corresponding reference chunk to find matching windows of the reference image.

During this hierarchical matching, additional blocks of overlapping layers are used. These blocks are used to ensure the accuracy of matchings. Blocks of overlapping layer surround a segment block in a pyramid structure, as shown in Figure 3.4 (b). When a moving segment block and its surrounding blocks of overlapping layers match in the same hierarchy within the corresponding reference template block, segment matching is considered an actual match. Similarly, each chunk block is

surrounded by an overlapping block. If a moving chunk and its overlapping block match in the same hierarchy within the corresponding reference segment, it is considered an actual match. In both cases, if the match is not an actual match, then the block is regarded as a non-displaced block.

3.4.4 3D LWM transformation

This section explains the calculation of a dense transformation function between a moving image and the reference image. LWM is a radial basis function, and it maps all the points of the moving image to the reference image by calculating local transformations. LWM function takes control points of moving and reference image as inputs, which are found in the previous Section 3.4.3. Moreover, the local transformation is estimated by an input variable n. The control points are sparse matches, which LWM uses to provide the outcome of dense matches.

The initial step for 3D LWM is to organise the matching control points $\{(x_i, y_i, z_i), (X_i, Y_i, Z_i): i = 1, \dots, N\}$ according to Equation 3.2.

$$\{(x_i, y_i, z_i, X_i): i = 1, \dots, N\},$$

$$\{(x_i, y_i, z_i, Y_i): i = 1, \dots, N\},$$

$$\{(x_i, y_i, z_i, Z_i): i = 1, \dots, N\} \tag{3.2}$$

where (x_i, y_i, z_i) and (X_i, Y_i, Z_i) are control points of the reference image and moving image, N is the total number of control points.

The next step is to compute three polynomials $Poly_{i,x}$, $Poly_{i,y}$, and $Poly_{i,z}$ that fit the corresponding i^{th} control point and the closest $(n - 1)$ neighbours of that control point. The order of each polynomial is the second, and the coefficients used to define the polynomials are 10. $Poly_{i,x}$, $Poly_{i,y}$, and $Poly_{i,z}$ are used to

calculate X-component, Y-component, and Z-component, respectively, of the transformed point.

3D transformation of any point $p = (x, y, z)$ can be computed by calculating the weighted mean of all polynomials, passing over that point-p. The transformation of each X-component, Y-component, and Z-component can be found according to Equation 3.3.

$$X(x,y,z) = \frac{\sum_{i=1}^{N} W\left\{\frac{\left[(x-x_i)^2+(y-y_i)^2+(z-z_i)^2\right]^{\frac{1}{2}}}{R_n}\right\} Poly_{i,x}(x,y,z)}{\sum_{i=1}^{N} W\{[(x-x_i)^2+(y-y_i)^2+(z-z_i)^2]^{1/2}/R_n\}},$$

$$Y(x,y,z) = \frac{\sum_{i=1}^{N} W\left\{\frac{\left[(x-x_i)^2+(y-y_i)^2+(z-z_i)^2\right]^{\frac{1}{2}}}{R_n}\right\} Poly_{i,y}(x,y,z)}{\sum_{i=1}^{N} W\{[(x-x_i)^2+(y-y_i)^2+(z-z_i)^2]^{1/2}/R_n\}},$$

$$Z(x,y,z) = \frac{\sum_{i=1}^{N} W\left\{\frac{\left[(x-x_i)^2+(y-y_i)^2+(z-z_i)^2\right]^{\frac{1}{2}}}{R_n}\right\} Poly_{i,z}(x,y,z)}{\sum_{i=1}^{N} W\{[(x-x_i)^2+(y-y_i)^2+(z-z_i)^2]^{1/2}/R_n\}} \qquad (3.3)$$

where R_n refers to the distance between p and its $(n-1)^{th}$ nearest control point. $Poly_{i,x}$ refers to the polynomial passing through the point (x_i, y_i, z_i, X_i), $Poly_{i,y}$ refers to the polynomial passing through the point (x_i, y_i, z_i, Y_i), $Poly_{i,z}$ refers to the polynomial passing through the point (x_i, y_i, z_i, Z_i). W is mentioned in Equation 3.4 and Equation 3.5.

$$W(R) = 1 - 3R^2 + 2R^3, 0 \leq R \leq 1,$$

$$W(R) = 0, R > 1 \qquad (3.4)$$

$$R = [(x - x_i)^2 + (y - y_i)^2 + (z - z_i)^2]^{1/2}/R_n \qquad (3.5)$$

where n refers to the number of local control points, R_n refers to the distance between p and its $(n-1)^{th}$ nearest control point, W is the weight function.

According to the definition of W, the transformation polynomials can only affect local points of a control point (x_i, y_i, z_i), who have a distance less than R_n from that control point. Therefore, 3D LWM is capable of providing local transformation. Moreover, the derivative of W with respect to R is zero for values $R = 0$ and $R = 1$. This property is mentioned in Equation 3.6, and it ensures smoothness and continuity of the weighted sum for all image points without being restricted to the local distance.

$$\left[\frac{dW}{dR}\right]_{R=0} = \left[\frac{dW}{dR}\right]_{R=1} = 0 \tag{3.6}$$

The transformation functions in all pairs of images are calculated with respect to the reference end-diastolic image. The value of n is selected as $n = 100$, which is discussed in the discussion Section 3.5.2.

These transformations are used to calculate displacement tensors, which are further used for 3D strain calculation, as formulated in Section 3.4.5.

3.4.5 3D strain estimation

In this section, the 3D strain calculation is described by utilising the transformations calculated in the previous Section 3.4.4. The formulation follows the continuum mechanics and medical imaging literature (Abd-elmoniem, Stuber and Prince, 2008; Lai, Rubin and Krempl, 2010). The segmented LV myocardium points are tracked in all the images of a cardiac cycle in a forward tracking manner. The location of a myocardial point $p(x, y, z)$ is $[x, y, z]^T = f_{Deformation}(p, t)$ at time t. The displacement vector $u(x, t) = \left[u_x, u_y, u_z\right]^T$ is calculated as a difference in spatial locations with respect to the reference end-diastolic frame. The displacement gradient tensor is defined in Equation 3.7.

$$U = \begin{bmatrix} \dfrac{\partial u_x}{\partial x} & \dfrac{\partial u_x}{\partial y} & \dfrac{\partial u_x}{\partial z} \\[8pt] \dfrac{\partial u_y}{\partial x} & \dfrac{\partial u_y}{\partial y} & \dfrac{\partial u_y}{\partial z} \\[8pt] \dfrac{\partial u_z}{\partial x} & \dfrac{\partial u_z}{\partial y} & \dfrac{\partial u_z}{\partial z} \end{bmatrix} \tag{3.7}$$

where u refers to the 3D displacement vector.

After calculating the displacement gradient tensor U, the deformation gradient tensor F is calculated according to Equation 3.8. The code is adapted from MATLAB [Kroon], which is updated with the Lagrange strain definition.

$$F = (I - U)^{-1} \tag{3.8}$$

where F is deformation gradient, I is the identity matrix, U is displacement gradient.

Using F, the 3D strain tensor of Lagrange strain is estimated according to Equation 3.9.

$$E = \frac{1}{2}(F^T F - I) \tag{3.9}$$

where E is Lagrange strain, F is deformation gradient, I is the identity matrix.

After the strain estimation, the strain E is projected in the circumferential, radial and longitudinal directions using the local coordinate system. Strain projection definitions are followed from the benchmark framework literature (Tobon-Gomez, Craene, Mcleod, *et al.*, 2013). The projected strain is described by $E_p = p^T \cdot E \cdot p$, where p is a respective direction (circumferential, longitudinal, radial). The definition of longitudinal direction (L) is a line from the apex to the mitral valve of the base. The radial direction is $R = M - (M \cdot L)L$, where M refers to the nodal normal at each point. Therefore, the radial direction is pointing outwards and at 90 degrees to the epicardial surface. Circumferential direction (C) is a cross product between L and R. Therefore, the circumferential direction is in the SAX plane,

parallel to epicardium, and counter-clockwise, if observed from the base.

3.5 Discussion

This chapter has elaborated 3D extension of the HTM method, allowing for 3D myocardial tracking and strain calculation. The accuracy of the calculated strain is discussed in Chapter 6, with results and validation. The technical strengths, parameter selection and limitations of 3D HTM are explained in the following sections.

3.5.1 Strengths

In the literature review of Chapter 1 and Table 1.3, it is highlighted that some of the methods are natively 2D, and some of the techniques require to merge with other methods to perform 3D myocardial tracking, which are technical limitations to accurately calculate strain values. 3D HTM can perform myocardial tracking by directly incorporating the through-plane motion of LV. As a result, at each myocardial point, a 3D strain tensor can be estimated. Moreover, 3D LWM, which is incorporated in 3D HTM, is robust to prevent errors of ill-conditioned polynomials due to its mathematical advantages of efficiently solving system of equations. Besides, some of the existing methods require tissue material properties as a part of the technique, reported in the literature as limiting factors. HTM does not require such dependencies.

3.5.2 Parameter selection

In Section 3.4.4 Equation 3.5, the value of n is selected as $n = 100$ after performing a small in-house study. We have randomly selected 10 out of 15 patients and performed experiments of myocardial tracking using ground truth myocardial points. The benchmarking framework provides 12 anatomical locations as these ground truth points. We have selected different n values starting from $n = 10$ to $n = 200$, and assumed that the values within these values would not significantly change the results. The experiments of tracking ground truth myocardial points have reported tracking error in terms of Euclidean distance in millimetre. An analysis of n values is given in Figure 3.5.
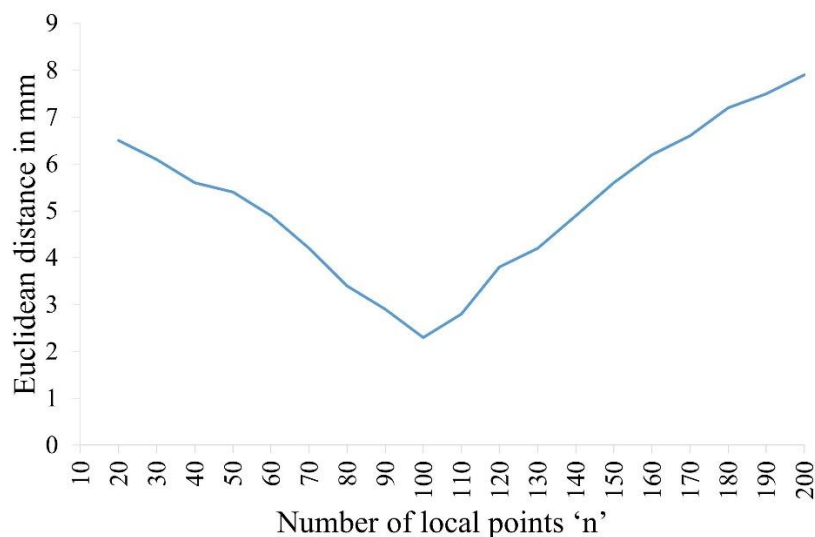
Figure 3.5| Myocardial tracking error of 3D HTM with a different number of local points (n) in 3D local weighted mean function. Y-axis shows Euclidean distance of myocardial tracking, which is defined in Section 3.3, and the number of local points and local weighted mean function are defined in Section 3.4.4.

As shown in Figure 3.5, the error values associated with n are higher in the beginning compared to the minimum error. The error values are gradually decreasing from $n = 20$ to $n = 100$. At $n = 100$, the tracking error is reported minimum, and the error is increasing from $n = 100$ to $n = 200$. 8 out of 10 subjects have

reported minimum myocardial tracking error at $n = 100$, and two subjects have reported minimum error at $n = 110$. Therefore, we have selected the parameter value of $n = 100$. It is observed that the higher and much lower values of parameter n can produce a higher error while tracking myocardial points.

In Section 3.4.3, the value of t is selected as 16, and the template size is chosen as $16 \times 16 \times 16$. This value of t is selected according to the experimental discussion of Chapter 2, Section 2.5.2. Moreover, the overlapping layers in the hierarchical matching are used to ensure the matching accuracy with this template size. From the experiments of Chapter 2 Section 2.5.2, the smaller values of t (less than 16 in each dimension) may give more incorrect matchings during the template matching step.

The input of 3D HTM is grid tagging MRI volumes for the myocardial tracking.

3.5.3 Limitations

3D HTM has used grid tagging MRI for myocardial tracking and SSFP MRI to segment the LV mesh. Therefore, the registration between image volume and segmented LV is prone to misregistration of slices, limiting the accuracy of myocardial tracking and strain calculation. The accuracy of the method is sensitive to selecting parameters n and t, which could be the technique's limitations. Moreover, image artefacts and tag fading issues in image volumes may cause myocardial tracking errors as HTM is fundamentally developed upon image intensity values. As future work, it is recommended that the 3D HTM is technically extended with other imaging modalities, such as Echo, so that the 3D local weighted mean function can be tested with speckle tracking methods.

3.6 Summary

In this chapter, the 3D extension of HTM is described to characterise 3D myocardial strain using MRI volumes. 3D HTM method is developed upon block-matching, LWM transformation and strain calculation. LWM function is introduced in the myocardial tracking and strain calculation pipeline through HTM. The 3D extension of LWM and technical details to calculate 3D strain is described. The technical strengths and limitations of 3D HTM and discussion of parameter selection are provided. The results and validations with the benchmark framework are reported in Chapter 6. The 3D HTM method has been published in a journal article (Bhalodiya, Palit, Ferrante, *et al.*, 2019). Further technical extension of HTM is considered as future work.

Chapter 4

Application Method – Application for Myocardial
Infarction Patients

4.1 Introduction

In this chapter, an application method of myocardial strain
identifies infarcted myocardial LV segments without using GBCA.
The myocardial strain is utilised as a basis of the method to
separate infarcted and non-infarcted myocardium. A clinical
dataset of myocardial infarction patients is used with the 2D HTM
method. The description of the technical steps and characteristics
of the data cohort are explained. The discussion of strengths and
limitations, along with justification for technical steps, are
detailed. The results, validation and potential clinical implications
are reported in Chapter 7. The method has been published as an
article (Bhalodiya, Palit, Giblin, *et al.*, 2021).

4.2 Dataset of myocardial infarction patients

A dataset of 38 MI patients and 5 healthy volunteers were
collected from the cardiac magnetic resonance (CMR) unit of the
Royal Brompton and Harefield NHS Trust (RBHT). Ethical
approval for retrospective data collection was obtained from the
NHS (IRAS project ID: 211977). Additionally, Biomedical and
Scientific Research Ethics Committee (BSREC) approval (REGO
2016-1865) was obtained from the University of Warwick to
process the anonymised data.

All the subjects were selected retrospectively. Patients with an MI
identified on CMR were determined from the referral details and
scan reports. The inclusion criteria are: (i) a patient, who has a
known history of infarcted myocardium, or (ii) a patient referred

for a clinically indicated CMR scan, based on symptoms suggestive of myocardial ischemia, with or without an elevation in serum troponin levels, and with a confirmed myocardial infarct on the subsequent CMR. The included patients underwent a standard departmental CMR using either a vasodilator stress perfusion protocol or a viability protocol, including comprehensive late gadolinium enhancement imaging. Patients without known infarction and other clinical conditions, such as cardiomyopathy, were excluded. All the MI subjects have anonymised images of LGE imaging and grid-tagging MRI. The images were acquired with three different 1.5T Siemens MRI scanners, with ECG triggering. LGE images were acquired with sequences that allowed the patient's normal breathing and have infarcted myocardium with high-intensity values due to post-gadolinium enhancement. Grid-tagging MRI was obtained with breath-holds, having a grid structure of myocardial tagging lines with a spacing of 6mm. In healthy subjects, LGE imaging is not available.

In all the data subjects, images from three short-axis (SAX) LV planes are processed: basal, mid-ventricular and apical SAX planes of LV. MRI SAX plane covers a lot of anatomical details of the chest. Therefore, to efficiently process data, the LV area of each image is cropped using ImageJ software. While cropping images, we ensured that all subjects' images were well-registered and had the same image dimensions.

The characteristic details of the dataset are mentioned in Table 4.1.

Table 4.1 | Characteristic details myocardial infarction patients and healthy subjects.

	Total subjects (n=43)
MI Patients	
Total MI patients	38
Sex (male/female)	Male-33, Female-5
Age (year) (mean±stdev)	63.65 ± 13.31
Size (metre) (mean±stdev)	1.74 ± 0.10
Weight (kilogram) (mean±stdev)	84.42 ± 19.79
Pixel size (millimeter)	1.32 × 1.32 to 1.75 × 1.75
Healthy Subjects	
Total healthy subjects	5
Sex (male/female)	Male-2, Female-3
Age (year) (mean±stdev)	41.20 ± 14.38
Size (metre) (mean±stdev)	1.68 ± 0.08
Weight (kilogram) (mean±stdev)	65.2 ± 13.04
Pixel size (millimeter)	1.48 × 1.48

4.3 Validation and image analysis

The validation of the 2D application method is performed through LGE (Pennell, Sechtem, Higgins, *et al.*, 2004) and the ROC test (Šimundić, 2009; Hajian-Tilaki, 2013) for diagnostic performance evaluations. The validity of comparison with LGE is justifiable, as LGE is the gold-standard clinical method in CMR to identify infarcted myocardium.

In each patient, infarcted segments (AHA segments) are identified using LGE imaging by a cardiothoracic consultant and surgeon with more than ten years of experience. LV segments revealed with gadolinium enhancement during LGE imaging are considered infarcted segments. Note that the transmural or non-transmural both conditions of LV segments are regarded as

infarcted. Transmurality is not separately assessed. Basal grid tagging with the basal LGE slice, mid-ventricular grid tagging with mid-ventricular LGE, and apical grid tagging with apical LGE imaging slice are matched. Infarcted LV segments identified from LGE imaging are used as ground truth to validate the proposed Hierarchical Template Matching-Circumferential Strain (HTM-CS)-based predictions. Therefore, the validation hypothesis for the statistical analysis is that the infarcted LV myocardial AHA segments identified using HTM-CS would be the same as the ground truth of LGE. More details of k-fold cross-validation tests are mentioned in Section 4.4.6.2.

According to the AHA model, LV myocardium is segmented (manually outlined) for each basal, mid-ventricular, and apical slices (Cerqueira, Weissman, Dilsizian, *et al.*, 2002). Then, for each basal, mid-ventricular and apical slices, the area under the curve (AUC) values of ROC tests are used to validate detection performance compared to LGE performance. AUC refers to the area under the sensitivity vs 1-specificity curve. Moreover, subject-specific results of identifying infarcted LV segments compared to LGE are validated with true positives, true negatives, false positives, false negatives, true positive rate and false-positive rate to understand the subject-specific validity of detections.

4.4 Method to identify infarcted myocardium
4.4.1 Overview

The method aims to identify infarcted myocardial segments of LV using circumferential strain. The overview of the method is shown in Figure 4.1. The five steps of the method are as follows, which are explained in the following sections: (i) segmentation, (ii) image registration, (iii) myocardial strain estimation, (iv) LV

classification as per the AHA model, and (v) detection of infarcted LV segments.
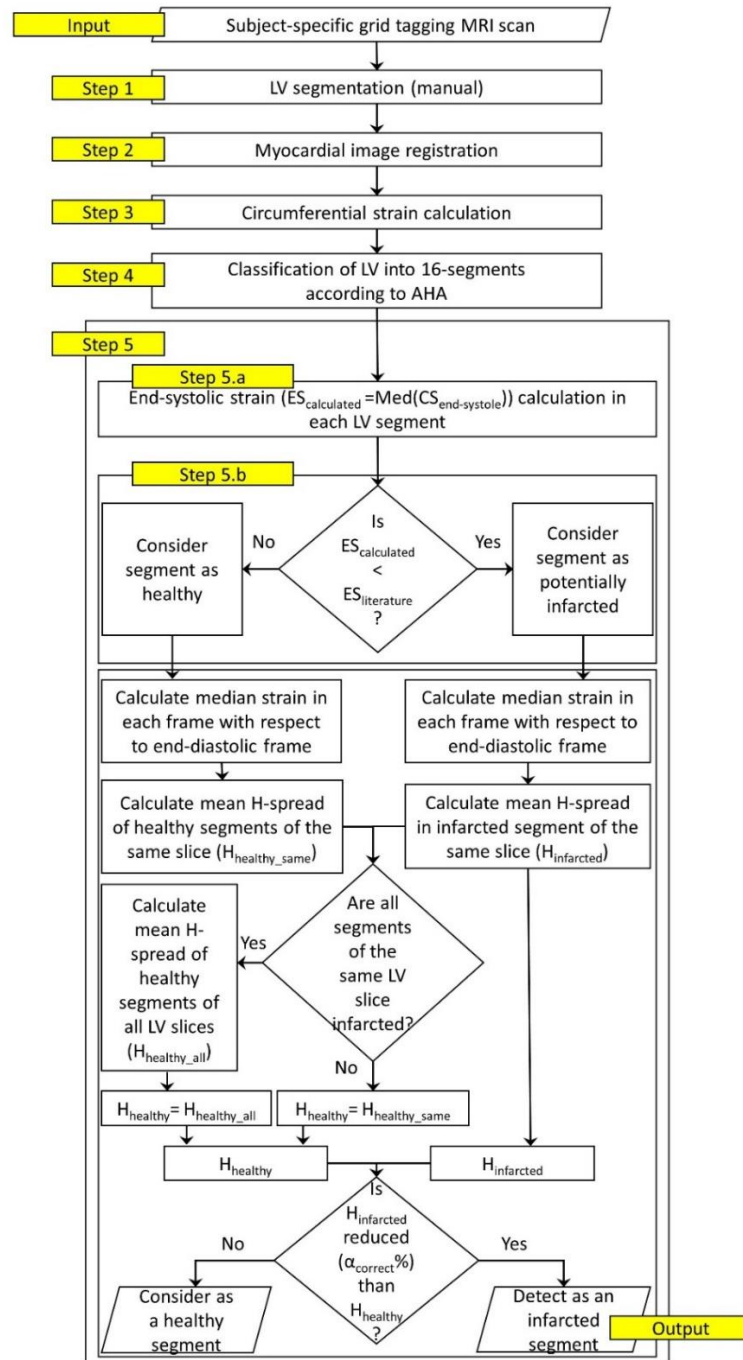
Figure 4.1| Flowchart of the proposed applied method to identify infarcted LV segments using circumferential strain values(Bhalodiya, Palit, Giblin, *et al.*, 2021). Here, $H_{healthy\_same}$ could be $H_{healthy\_basal}$ or $H_{healthy\_mid}$ or $H_{healthy\_apical}$, which are defined in Section 4.4.6.1. α and $\alpha_{correct}$ are defined in Section 4.4.6.2. $ES_{literature}$ refers to the end-systolic circumferential strain reported in Table 4.2 from literature(Moore, Lugo-Olivieri, McVeigh, *et al.*, 2000).

4.4.2 Segmentation – step 1

The endocardium and epicardium are segmented (manually outlined) using the software package ImageJ [ImageJ]. LV segmentation was performed using SAX slices of the base, mid-ventricle and apical level. The segmentation was verified by a cardiothoracic consultant and surgeon with more than ten years of experience.

4.4.3 Image registration – step 2

Image registration to perform myocardial tracking is carried out using the 2D HTM method, elaborated in Chapter 2. An overview of the 2D HTM method is shown in Figure 4.2. Myocardial points are tracked in all the frames of a cardiac cycle from end-diastole to end-systole. As mentioned in Equation 4.1, the tracking is used to calculate displacement vector $V(x, y)$ of each myocardial point in all the frames with respect to the end-diastolic frame. The gradient of each displacement vector, ∇V, is calculated according to Equation 4.2.

$$V(x, y) = P_{end-diastole}(x_1, y_1) - P_{current-frame}(x_2, y_2) \quad (4.1)$$

where P refers to the spatial position of a point.

$$\nabla V = \begin{pmatrix} \frac{\partial V_x}{\partial x} & \frac{\partial V_x}{\partial y} \\ \frac{\partial V_y}{\partial x} & \frac{\partial V_y}{\partial y} \end{pmatrix} \quad (4.2)$$

where ∇V refers to the displacement gradient.
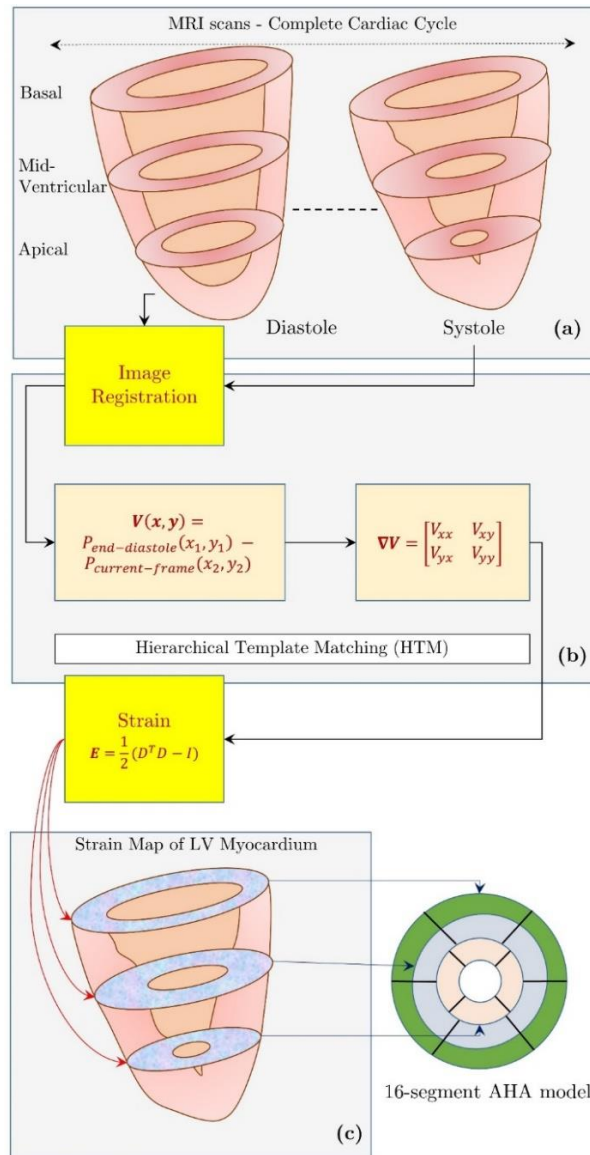
Figure 4.2| Overview of HTM-based myocardial tracking and strain. **(a)** MRI scans of a cardiac cycle at three LV levels: Basal, Mid-ventricular, and Apical. **(b)** HTM method to calculate strain values at each muscle point. V refers to the displacement vector. ∇V refers to the displacement gradient. **(c)** LV strain values, which are analysed using the 16-segment AHA model. In panel **(a)** and **(c)**, basal refers to the slice near the mitral valve and before the beginning of papillary muscle, mid-ventricular refers to the slice at the approximate middle of papillary muscle length, and apical refers to the slice towards the apex but above the apex(Cerqueira, Weissman, Dilsizian, *et al.*, 2002; Selvadurai, Puntmann, Bluemke, *et al.*, 2018).

4.4.4 Myocardial strain estimation – step 3

The myocardial strain is estimated according to the Green-Lagrange strain definition (Lai, Rubin and Krempl, 2010). The selection of Lagrange strain is further discussed in the Discussion Section 4.5.2. As mentioned in Equation 4.3, the displacement gradient is used to estimate deformation gradient (Abd-elmoniem, Stuber and Prince, 2008), which is used to estimate Lagrange strain in LV myocardium (Tobon-Gomez, Craene, Mcleod, *et al.*, 2013), as mentioned in Equation 4.4.

$$D = (I - \nabla V)^{-1} \tag{4.3}$$

$$E = \tfrac{1}{2}(D^T D - I) \tag{4.4}$$

where D is deformation gradient, ∇V is displacement gradient, I is the identity matrix, E is Lagrange strain.

Lagrange strain, E, is estimated at each myocardial point using a global coordinate system. E is projected in the circumferential direction using the local coordinate system according to the literature (Moore, Lugo-Olivieri, McVeigh, *et al.*, 2000). The circumferential strain has a positive direction in the SAX plane and counter-clockwise, if observed from the base. The direction is parallel to the epicardium border and at the right angle to the longitudinal line joining the apex to the mitral valve.

4.4.5 LV classification as per AHA model – step 4

Circumferential strain values are organised according to the 16-segment AHA model of LV classification (Cerqueira, Weissman, Dilsizian, *et al.*, 2002), explained in Chapter 1, Section 1.2.2.3.1. Each SAX slice of the basal and mid-ventricular level is partitioned into six segments: anterior, inferior, anterolateral, anteroseptal, inferolateral, and inferoseptal. Each apical SAX slice

is divided into four segments: anterior, inferior, lateral, and septal.

4.4.6 Detection of infarcted segments – step 5

This section defines the H-spread in the context of myocardial strain and describes steps to detect infarcted LV segments through k-fold cross-validation.

4.4.6.1 H-spread and detection

Infarcted myocardium does not elongate or shorten like healthy myocardium. As a result, the strain patterns of infarcted and non-infarcted myocardium during the cardiac cycle are different. Such strain patterns can be shown with a median and H-spread of strain values, as shown in Figure 4.3. Median strain values are used to avoid any large errors in strain values.
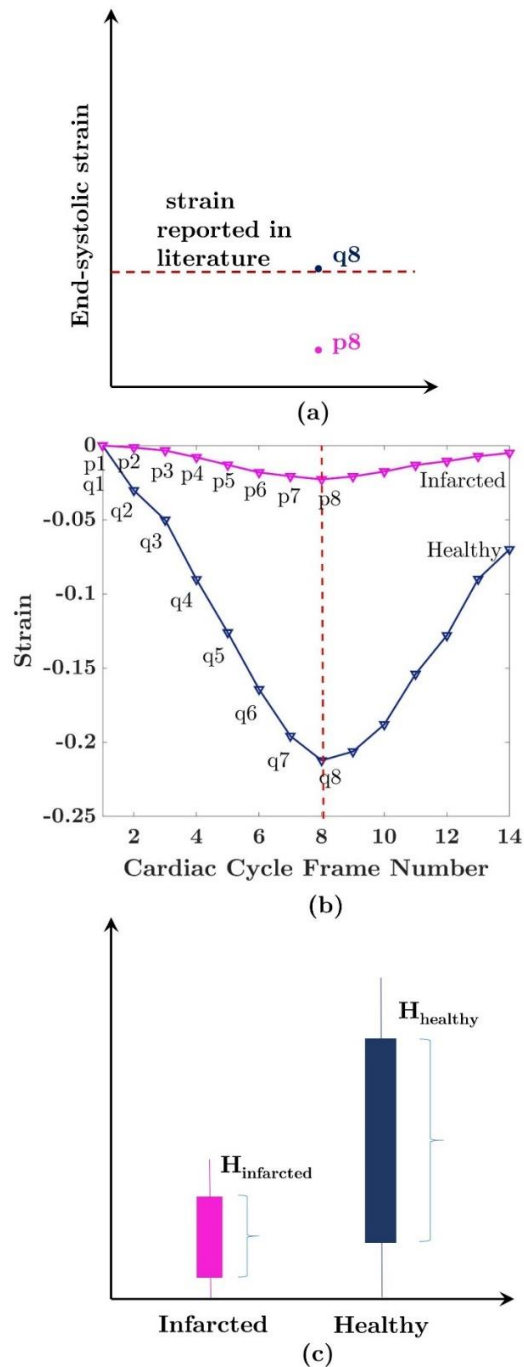
Figure 4.3| An example of comparing strain at the end-systolic frame, strain at each frame, and strain H-spread between healthy and infarcted LV segment. **(a)** An example of comparing only end-systolic strain values between healthy and infarcted myocardial segment. **(b)** An example of comparing strain values of individual frames of a cardiac cycle between a healthy and infarcted myocardial segment. **(c)** An example of comparing strain H-spread between healthy and infarcted myocardial segment.

H-spread of an LV segment is defined as a union (union refers to the mathematical union operation of set theory) of median strain values in each cardiac cycle frame ranging from end-diastole to end-systole. For example, as shown in Figure 4.3(c) and Equation 4.5, H-spread of an infarcted segment is calculated by the union of values $p_1, p_2,..., p_8$. Similarly, the union of values $q_1, q_2, ..., q_8$ shows H-spread of a healthy segment.

$$HSpread \ of \ an \ LV \ segment = \ HSpread\left(\cup_{i=ED}^{i=ES} S_{f_i}\right) \quad (4.5)$$

where ED refers to the end-diastolic frame, ES refers to the end-systolic frame, U refers to the mathematical union operation of set theory, and $S_{f_i} = Med(CS_{end-systole})$ at i^{th} frame.

Infarction Condition: A potentially infarcted segment has at least $\alpha\%$ reduced strain H-spread compared to the mean H-spread of remaining LV segments of the same LV slice. If all segments of a slice are infarcted, then healthy segments of the whole LV are considered instead of only considering the same slice.

After calculating the H-spread of "potentially infarcted" segments, *"Infarction Condition"* is checked to decide whether the "potentially infarcted" segment is an infarcted segment or not. During this step, H-spread values are calculated, as described in Equation 4.6.

$$H_{infarcted} = HSpread_{LV-segment}$$

$$H_{healthy\_basal} = \mu_{basal}(HSpread_{LV-segment})$$

$$H_{healthy\_mid} = \mu_{mid}(HSpread_{LV-segment})$$

$$H_{healthy\_apical} = \mu_{apical}(HSpread_{LV-segment})$$

$$H_{healthy\_all} = \mu_{basal-mid-apical}(HSpread_{LV-segment})$$

$$H_{healthy}$$
$$= H_{healthy\_basal} \; OR \; H_{healthy\_mid} \; OR \; H_{healthy\_apical} \; OR \; H_{healthy\_all}$$

$$(4.6)$$

Where μ refers to the mathematical mean, and $HSpread_{LV-segment}$ is as per Equation 4.5.

α could be any value greater than 0 and less than 100. For example, assume that segment 1 and 2 of a basal slice are "potentially infarcted" segments. These segments will be considered as actually infarcted if $HSpread_{LV-segment}$ is at least α% reduced compared to the mean H-spread of other segments in the basal slice ($H_{healthy\_basal}$) which includes segments 3, 4, 5 and 6. When all the segments of a slice are "potentially infarcted", then healthy segments of basal, mid-ventricular, and apical slices are used to calculate ($H_{healthy\_all}$). For example, suppose that segments 13, 14, 15, and 16 of an apical slice are "potentially infarcted". In that case, the healthy segments of basal and mid-ventricular slices are considered together during the H-spread comparison of the "Infarction Condition".

In this work, the following values of α are considered (Equation 4.7). It was assumed that the values within this range of α values would not change the results considerably.

$$\alpha = \{10, 20, 30, \ldots, 100\} \tag{4.7}$$

The α value corresponding to the highest accuracy with the training dataset is called $\alpha_{correct}$, described later in this section. Tests are performed using k-fold cross-validation (Molinaro, Simon and Pfeiffer, 2005; Kuhn and Johnson, 2013). Peak systolic circumferential strain values of Table 4.2 are adapted from the literature (Moore, Lugo-Olivieri, McVeigh, *et al*, 2000). The literature has mentioned strain values for the septal and lateral wall of LV without further dividing it into inferolateral, inferoseptal, anterolateral, and anteroseptal segments. Therefore, to enable using the literature values in our method, the same values for both anterolateral and inferolateral are used. Similarly, the same values for anteroseptal and inferoseptal are used.

123

Table 4.2 | End-systolic circumferential strain values in healthy LV myocardium.

LV Slice	Anteroseptal strain	Inferoseptal strain	Anterior strain	Anterolateral strain	Inferolateral strain	Inferior strain
Basal	-0.17±0.03	-0.17±0.03	-0.20±0.03	-0.21±0.03	-0.21±0.03	-0.16±0.03
Mid-ventricular	-0.16±0.03	-0.16±0.03	-0.23±0.04	-0.22±0.03	-0.22±0.03	-0.16±0.05
Apical	-0.18±0.03		-0.24±0.06	-0.24±0.04		-0.23±0.04

4.4.6.2 k-fold cross-validation

In each patient, infarcted LV segments are identified using LGE imaging. LV segments (transmural and non-transmural) revealed with gadolinium enhancement during the LGE test are considered infarcted segments. Transmural or non-transmural, both conditions of LV segments are regarded as infarcted. Transmurality is not separately assessed. These segments are used as ground truth and compared with HTM-CS-based detections of infarcted segments. This section explains k-fold cross-validation(Kuhn and Johnson, 2013) using the ROC curve test(Šimundić, 2009; Hajian-Tilaki, 2013), which is used to validate the method.

The area under the curve (AUC) of true negative rate (sensitivity) and the false positive rate (1-specificity) are calculated from ROC curve tests(Šimundić, 2009; Hajian-Tilaki, 2013), as prediction performance criteria, where AUC 1.0 is the highest accuracy, and AUC 0.5 is the least accuracy. ROC tests have a confidence interval of 95%. Data were prepared by dividing each LV into 16 AHA segments, and the segments are arranged as per basal, mid-ventricular, and apical slice. Total segments of basal are 258 (258=43×6), mid-ventricular are 258 (258=43×6), and apical are 172 (172=43×4). Each segment is assigned a label, as infarcted or healthy, according to LGE ground truth. Then, HTM-CS H-spread reduction is assigned to each "potentially infarcted"

segment (healthy segments are considered 0% H-spread reduction).

During k-fold tests, *"Infarction Condition"* is evaluated, using each α value (Equation 4.7). Each test assigns a score to each segment as infarcted or healthy. For example, an evaluation test with α=10 scores a potentially infarcted LV segment as infarcted if it satisfies the *"Infarction Condition"*; otherwise, it scores as healthy. As aforementioned, these scores and ground truth labels of each segment are given as input to the ROC test. α value is selected as α$_{correct}$ if the corresponding ROC test has the highest AUC. This α$_{correct}$ is used with the test dataset during the k-fold test to calculate the absolute accuracy. ROC curve tests are performed for each slice. Therefore, three separate α$_{correct-basal}$, α$_{correct-mid-ventricular}$, and α$_{correct-apical}$ are identified.

The results of detecting infarcted segments in the test dataset using three $\propto_{correct}$ values are reported as part of results and validation in Chapter 7. The selection of k value in the k-fold test is mentioned in the Discussion Section 4.5.2.

4.5 Discussion

4.5.1 Strengths

The described method does not require the use of GBCA like LGE. Therefore, the described method can extend the use of MRI based diagnosis in advanced renal impairment patients and overcome the concerns regarding GBCA. The described method uses grid tagging MRI to ensure the inclusion of structural deformation within the myocardium. Previously, Chapter 3 has reported a 3D technical extension for robust 3D strain calculation.

4.5.2 Justification for technical steps

In step 1 (Section 4.4.2), the described method performs manual segmentation of LV myocardium to ensure the accuracy of included myocardium and 16-segments. Manual segmentation could be a tedious task. However, as the method uses these segments as a basis, it is more justifiable to perform manual segmentation for accuracy.

In step 2 (Section 4.4.3), the method utilises 2D HTM for myocardial tracking because HTM includes structural deformation within the myocardium for strain calculation with grid tagging MRI. Structural deformation refers to the physiological change in the myocardium during a cardiac cycle. For example, if a cardiac cycle is recorded with a sequence of 20 MR images, then the structure of the myocardium in image one and image ten would be different. These details of the structure are essential details for myocardial tracking methods. Our infarction detection method is based on circumferential strain, which includes these crucial details of structural deformation within the myocardium. We have also shown images for structural details in the literature review Section 1.2.1 of Chapter 1.

In step 3 (Section 4.4.4), the method uses the Lagrange definition of strain as it is widely used in the clinical literature.

In step 4 (Section 4.4.5), the method uses three SAX slices of LV: basal, mid-ventricular and apical. Moreover, the literature's strain values (Moore, Lugo-Olivieri, McVeigh, *et al.*, 2000), as mentioned in Table 4.2, are also using grid tagging MRI of basal, mid-ventricular and apical LV SAX slices. Therefore, the described method has enabled the use of the literature strain values. This comparison should be limited for method development due to the difference in slice location, subject to different radiographers and

different LV sizes in human subjects. In future work, while performing a clinical study of the method, patients with all matching criteria should be recruited. To include a higher number of LV slices, strain value range in other SAX slices should be identified from the literature. At this stage of the described method, it is justifiable to use three slices and literature values, as it follows standard AHA guidelines. The technique is an applied method, and it does not perform a clinical study.

In step 5 (Section 4.4.6), the described method has used $k = 5$ to perform k-fold cross-validation. The values $k = 5$ or $k = 10$ are commonly preferred, as suggested in the literature (Kuhn and Johnson, 2013). Initially, we selected $k = 10$ in detecting infarcted segments using test dataset, and validation results of AUC values in ROC tests are reported with AUC=1 in three tests (1 out of 10 tests for basal LV segments, 1 out of 10 tests of mid-ventricular LV segments, and 1 out of 10 tests of apical LV segments) and AUC=0.5 in one test (1 out of 10 tests of basal LV segments). In contrast, when we repeated the same tests with $k = 5$, zero tests were reported with AUC=1 or AUC=0.5. Note that AUC=1 refers to the 100% accurate detection, and AUC=0.5 refers to the 0% accurate detection of the HTM method compared to the LGE imaging. Therefore, we have selected $k = 5$ as it was giving more realistic results compared to $k = 10$. Moreover, $k = 5$ is also a common choice for k-fold validation tests as mentioned in the literature(Kuhn and Johnson, 2013). We have plotted results with $k = 5$ in Chapter 7.

4.5.3 Limitations

The method uses manual segmentation of LV, which could be subjective. The method is limited to use three slices of LV. The method is flexible for the 3D extension. The number of data

samples is limited. The method uses circumferential strain calculated with HTM, which is based on image texture tracking. Therefore, as an inherited limitation of HTM, detecting infarcted segments may not be promising in the subjects having artefacts and blurred texture images.

4.6 Summary

In this chapter, a diagnostic application method for myocardial infarction patients is described, based upon the review included in Chapter 1. The method aims to diagnose infarcted myocardium using strain values. The technical strengths, a justification for technical steps and limitations are discussed. However, to understand the method's clinical implications, the method needs to be validated with clinical studies. At this stage, the method used data of 43 human subjects as part of the method and results. The characteristic details of the dataset are described in this chapter. The results are described in Chapter 7.

Chapter 5

Results – 2D Myocardial Tracking

5.1 Introduction

This chapter reports the validation results and discussion of the 2D myocardial tracking method described in Chapter 2. The used validation method of target registration error (TRE) and parameter details to develop comparative results of the benchmark - free form deformation (FFD) method are described in Chapter 2 Section 2.4.2. The dataset used to derive this chapter's results is detailed in Chapter 2 Section 2.4.1, representing the used sequence, magnetic field strength in Tesla, and details about patients. The results are published in a journal article (Bhalodiya, Palit, Tiwari, *et al.*, 2018).

5.2 Results of 2D myocardial tracking

TRE results of 2D myocardial tracking are calculated at four LV levels: basal, upper mid-ventricular, mid-ventricular and apical. The results are measured as the root mean square error in millimetre between actual myocardial point locations and the estimated locations with the HTM method. The details of the validation method are described in Chapter 2, Section 2.4.2. In Figure 5.1(a), the results are visualised according to the LV slices. In Figure 5.1(b), the results are elaborated for each LV slice and each cardiac cycle frame.

(a)

(b)
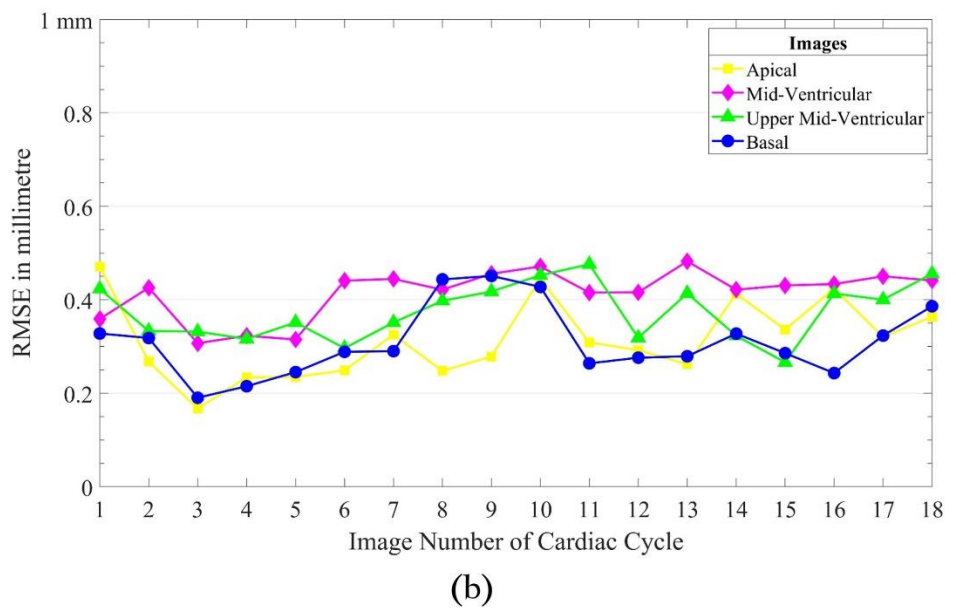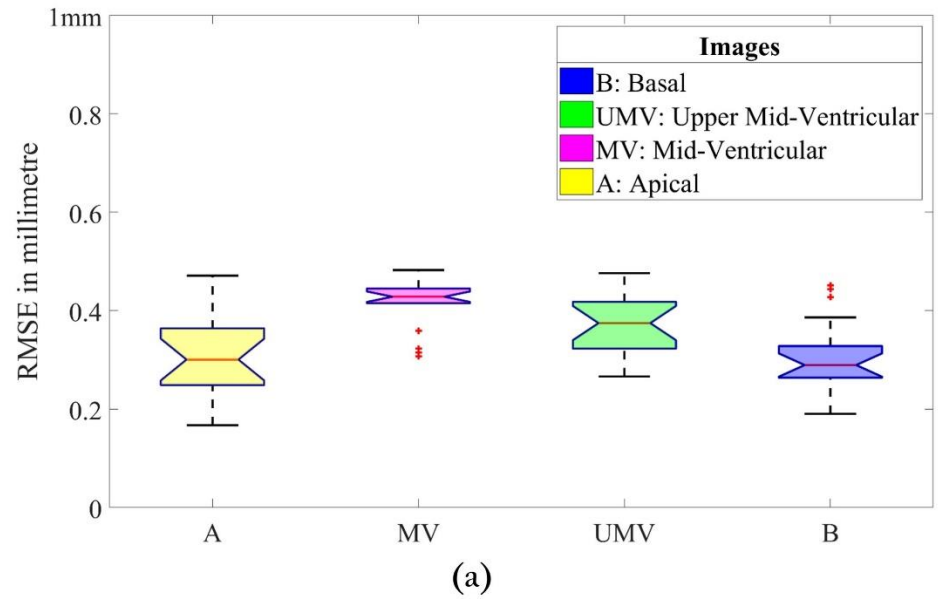
Figure 5.1| (a) TRE in basal, upper mid-ventricular, mid-ventricular, and apical SAX slices of LV. Each slice includes all segments of the respective slice and all frames of a cardiac cycle. The mid-ventricular slice has a 4% higher (P=0.05) mean error than the apical slice and 9% higher (P=0.15) mean error than the basal slice. No significant difference is found among upper mid-ventricular, basal, and apical slices. **(b)** TRE in each image frame of a cardiac cycle.

As mentioned in Figure 5.1 (a), basal SAX slice has a mean error of $0.31 \pm 0.07 \, mm$, upper mid-ventricular level slice has a mean error of $0.37 \pm 0.06 \, mm$, mid-ventricular level slice has a mean error of $0.41 \pm 0.05 \, mm$, and apical level slice has a mean error of $0.32 \pm 0.08 \, mm$. It can be seen in Figure 5.1 (b) that the TRE is less than half a millimetre in most of the images of the cardiac cycle.

To further validate our results, we have compared our results with the benchmark FFD method. The details of the FFD method can be found in Chapter 2, Section 2.4.2. The HTM and FFD results are compared (Figure 5.2), and a t-test is performed to understand the significance of the results. In Figure 5.2 (a), the overall results for all the images are shown. In Figure 5.2 (b), the results are compared for individual frames of the cardiac cycle.
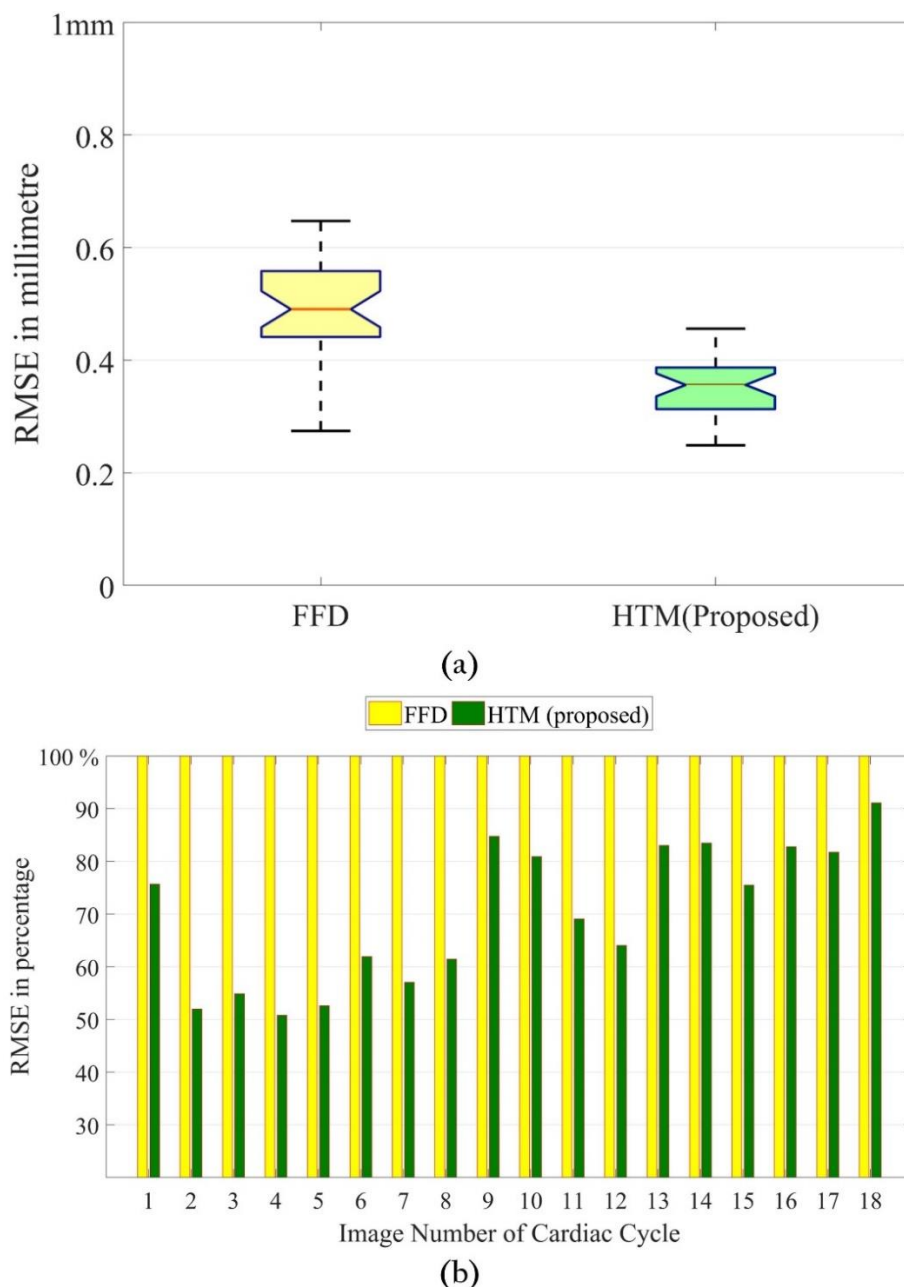
Figure 5.2| (a) Comparison of mean TRE in the proposed 2D HTM method with FFD-based benchmark method using 1080 short-axis images, including basal, mid-ventricular, upper mid-ventricular and apical images. HTM has a 17% reduced (P=0.07) error compared to FFD in a paired sample t-test. (b) Comparison of TRE in HTM and FFD in each image of a cardiac cycle. The yellow bar refers to FFD as the base, and with respect to each yellow bar, the corresponding green bar shows percentage error using 2D HTM. The height difference in each yellow and green bar graph shows the percentage error reduction using 2D HTM.

As shown in Figure 5.2, 2D myocardial tracking of HTM has reduced RMSE compared to FFD. Paired sample t-test is performed to check the significance level with the hypothesis that the HTM has x% reduced error compared to FFD. It is found that the HTM has 17% (P=0.07, CI:[-0.01,0.35]) reduced RMSE compared to FFD.

Moreover, in Figure 5.3, qualitative examples to compare the FFD method and the HTM method are shown. During the myocardial tracking, the FFD method and HTM method perform non-rigid image registration. Ideally, the derived output images with non-rigid registration should be the same as the cardiac cycle images. We compared both methods, with a couple of examples, to highlight the error issues of FFD. The reasons for the difference in results are discussed in the discussion section of this chapter.

(a)

FFD Output   Expected Output   HTM Output

(b)
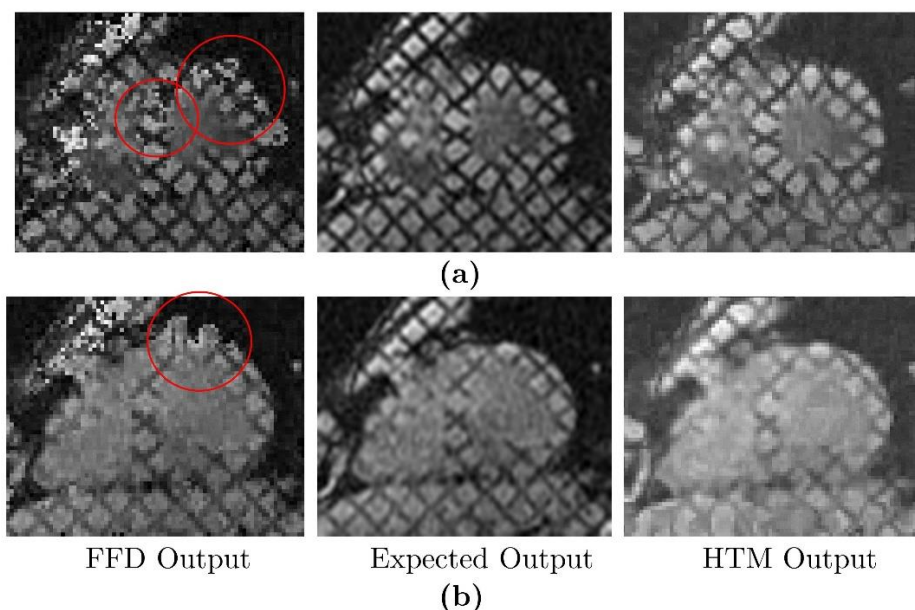
Figure 5.3| In both examples **(a)** and **(b)**, the left image is FFD-based output, the right image is HTM output, and the middle image is Expected output. Expected output refers to the original image, and FFD and HTM output refer to the derived images while performing myocardial tracking. The derived images (or registered images with image registration) of FFD are derived while tracking LV myocardium according to the parameters mentioned in Chapter 2, Section 2.4.2. HTM images are derived according to the method of Chapter 2 Section 2.2. The red circle shows error using the FFD-based benchmark method.

The strain values are reported with the results of the 2D application method, which is explained in Chapter 7 Section 7.2.

5.3 Discussion of results

As shown in the results of Figure 5.1, 2D myocardial tracking using HTM show improved accuracy with approximately half a millimetre error in most of the images of a cardiac cycle. The potential reason is dense and uniform hierarchical point matching of the HTM, which allows HTM to efficiently track the local

myocardial areas. Images from four LV slices have been examined, and it has been found that the RMSE of TRE is higher in the mid-ventricular slice compared to RMSE in other slices. The paired sample t-test shows that, within the same patient, the mean error reported in a mid-ventricular and apical slice has a significant difference (mid-ventricular slice has a 4% higher mean error with P=0.05). However, the difference in error among other slices is not significant. Then, we performed a t-test among FFD and HTM to understand the difference in error. We used images from all four LV slices and all frames of the cardiac cycle. The hypothesis tested is that the HTM has x% reduced error compared to FFD in a paired sample t-test. It is found that the HTM has 17% (P=0.07, CI:[-0.01,0.35]) reduced RMSE compared to FFD.

Moreover, quantitative examples have been shown in Figure 5.3 to highlight the reason for the higher error in FFD and the benefits of HTM. It can be seen in Figure 5.3 that FFD can produce a high error (highlighted in red circle) due to the ill-conditioned polynomials while doing computation. Such errors happen due to the spline-based transformation function. Previously, such observations have been reported in the literature (Deng and Denney, 2004). In contrast, our HTM method controls such errors with the LWM transformation function for geometric point transformation. LWM is a radial basis function. It can calculate the transformation function with a small system of equations. It is less complicated than the B-spline function while calculation, detailed in the literature (Maude, 1971; Goshtasby, 1988). Due to that, LWM can avoid ill-conditioned polynomials during computation and has the potential to perform better than spline-based and multi-quadratics transformation functions (Zagorchev and Goshtasby, 2006). Such LWM advantages have enabled HTM for better 2D myocardial tracking than the FFD-based benchmark method, shown in Figure 5.3. Moreover, the FFD-based

benchmark method needs a lot more tuning parameters, as listed in Chapter 2 Section 2.4.2, than HTM, limiting the accuracy of FFD on the subjective selection of values for tuning parameters.

However, HTM is also sensitive to the image quality and signal-to-noise ratio as HTM is fundamentally based on texture tracking, limiting the accuracy of 2D tracking of HTM in low-quality images. Moreover, the least number of local points, such as less than 6, may cause ill-conditioned polynomials and not allow LWM to perform transformation step and myocardial tracking. This limitation could be resolved by selecting a sufficiently more extensive number of local points, as explained in Chapter 2, Section 2.5.2.

The strain values related discussion is reported in Chapter 7, Section 7.3.

5.4 Summary

In this chapter, the results of 2D myocardial tracking using the HTM method are reported. Comparative results and discussion with the benchmark FFD method are provided. Results and discussion of statistical tests have been reported. The limitations regarding parameter selection are discussed in method Chapter 2 Section 2.5.2, and discussion of strain value analysis is written with results of the 2D application method in Chapter 7 Section 7.3.

Chapter 6

Results - 3D Myocardial Tracking and Strain Calculation

6.1 Introduction

This chapter reports on the 3D myocardial tracking and strain calculation method results, a method which is described in Chapter 3. Moreover, a comparative discussion of results with benchmark methods (Tobon-Gomez, Craene, Mcleod, *et al.*, 2013) is also presented in this chapter. Validation methods from the benchmark framework (Tobon-Gomez, Craene, Mcleod, *et al.*, 2013) and additional validation methods are described in Chapter 3 Section 3.3. The open-access 3D dataset used to derive the results of this chapter is detailed in Chapter 3 Section 3.2. 3D method and derived results are published in a journal article (Bhalodiya, Palit, Ferrante, *et al.*, 2019).

6.2 Results of 3D myocardial tracking and strain calculation

3D myocardial tracking is performed with an open-access dataset provided by the benchmark framework (Tobon-Gomez, Craene, Mcleod, *et al.*, 2013). This dataset has manually tracked points in the LV myocardium used by benchmark methods and our method to compare myocardial tracking results. The myocardial points are tracked from the end-diastole to the end-systole until the end of the cardiac cycle in each patient using the 3D HTM method. The tracking error is calculated with respect to the manually tracked ground truth landmarks from the dataset provider(Tobon-Gomez, Craene, Mcleod, *et al.*, 2013). The results are reported for three cases: error in all cardiac frames, error in final cardiac frames, and error in end-systolic cardiac frames. The error plots are shown in Figure 6.1, which includes all 15 patients from the

dataset. Details of dataset and validation method results are described in Chapter 3 Section 3.2 and Section 3.3.
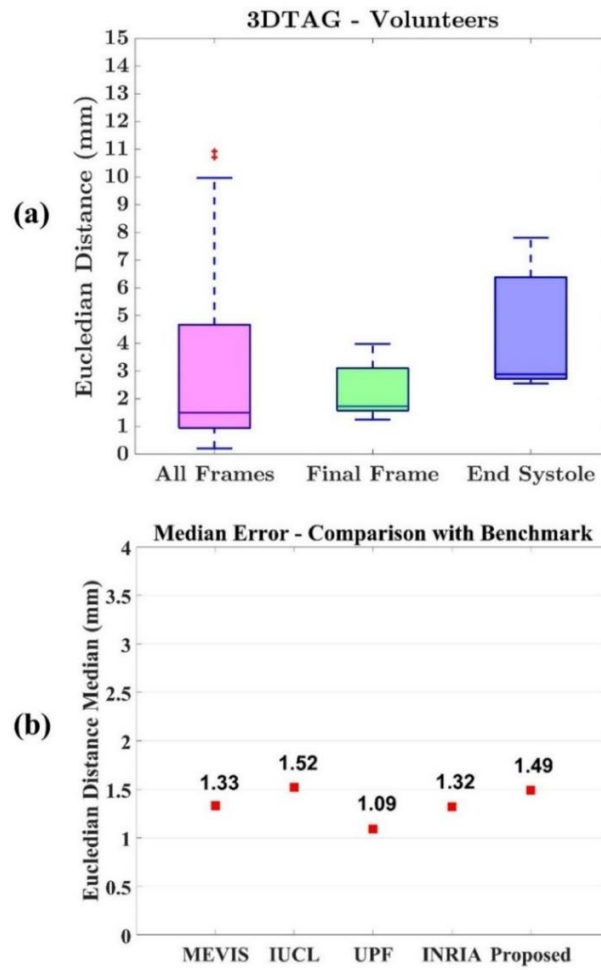
Figure 6.1| (a) Myocardial tracking error of 3D HTM method for three cases: error in all frames, error in final frames, and error in end-systolic frames, **(b)** comparison of median error among 3D HTM and benchmark methods for all frames.

As shown in Figure 6.1 (a), the 3D myocardial tracking of HTM has a median error $1.49mm$, $1.73mm$ and $2.88mm$ in cases of all frames, final frames and end-systolic frames, respectively. Figure 6.1 (b) compares the median tracking error among benchmark methods and the 3D HTM method for all frames. Benchmark methods are MEVIS, IUCL, UPF, and INRIA. The median errors of 3D myocardial tracking are MEVIS$=1.33mm$, IUCL$=1.52mm$, UPF$=1.09mm$, INRIA$=1.32mm$, and 3D HTM$=1.49mm$. As shown, the median error of 3D HTM is similar to one of the benchmark method and half a millimetre higher than other benchmark methods.

Figure 6.2 shows the displacement of myocardial points at end-systolic frames and final frames.
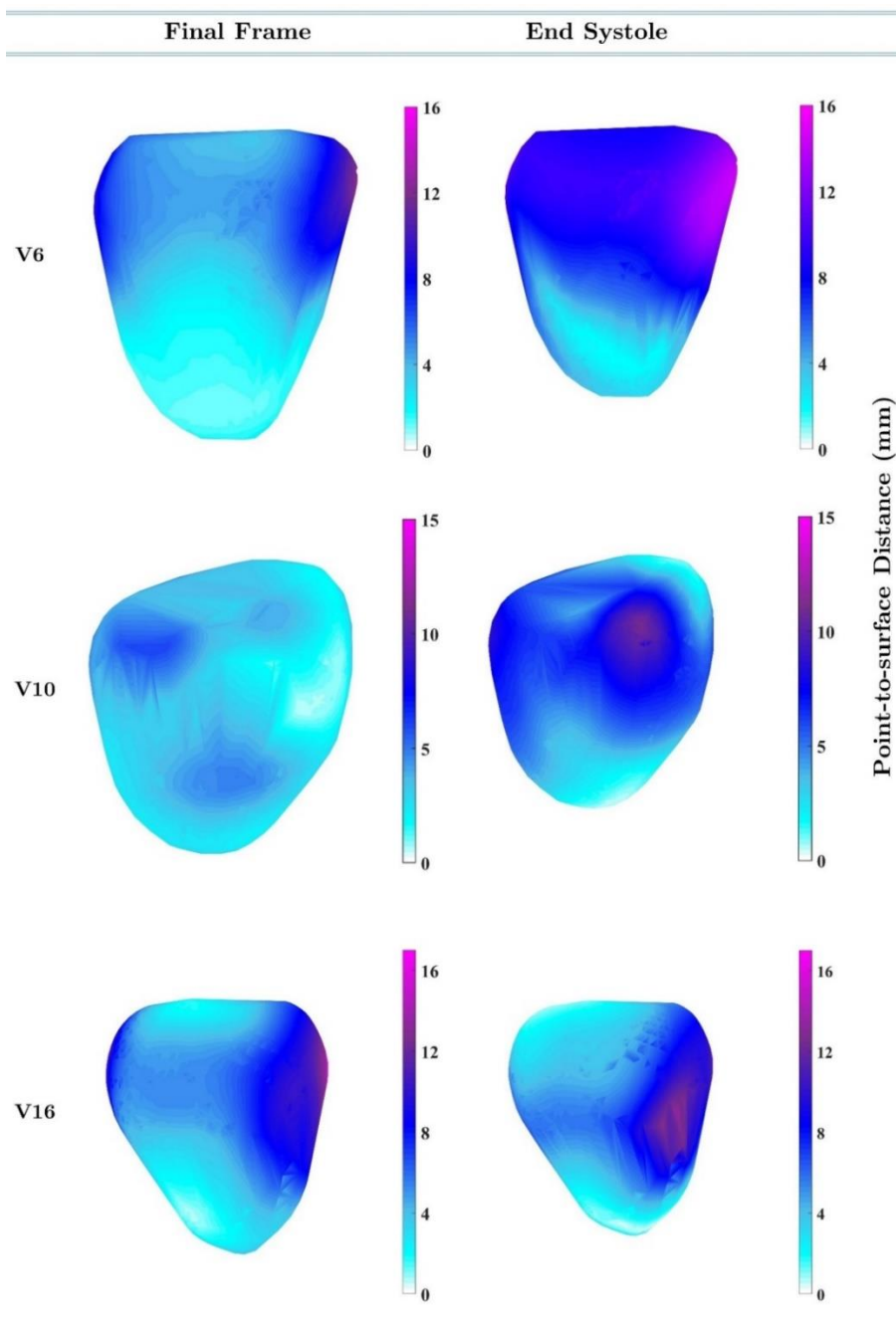
Figure 6.2| Displacement at the end-systolic frame and final frame in patients V6, V10, and V16. Point-to-surface distance shows the distance of a point from the reference end-diastolic surface.

The end-systolic frames are reported with an average $8mm$ to $18mm$ of point-to-surface distance, and the final frames are noted with an average of 0 to $6mm$ of point-to-surface distance. The images of the dataset are divided into three categories according to the quality of the images: (i) average, (ii) good, and (iii)

excellent. Average quality 3D images have localised artefacts in more than one plane or non-localised artefacts in one image-slice. Good quality images have localised artefacts in no more than one image-slice, and excellent quality images do not have artefacts. This categorisation is followed from the benchmark paper(Tobon-Gomez, Craene, Mcleod, *et al.*, 2013). Figure 6.2 has shown an example from each image quality category. It can be observed in patient V6 that the end-systolic frame has higher displacement in basal, mid-ventricular and partially apical areas compared to the final frame.

Similarly, V10 also has a higher displacement at the end-systolic frame than the final frame, especially in basal, mid-ventricular, apical, and partially apex areas. The patient V16 has higher end-systolic displacement in the mid-ventricular area compared to the final frame. Benchmark framework (Tobon-Gomez, Craene, Mcleod, *et al.*, 2013) has also reported similar results.

Figure 6.3 shows the strain curve results.

3DTAG − Myocardial Strain

volunteer 4

volunteer 2

volunteer 1
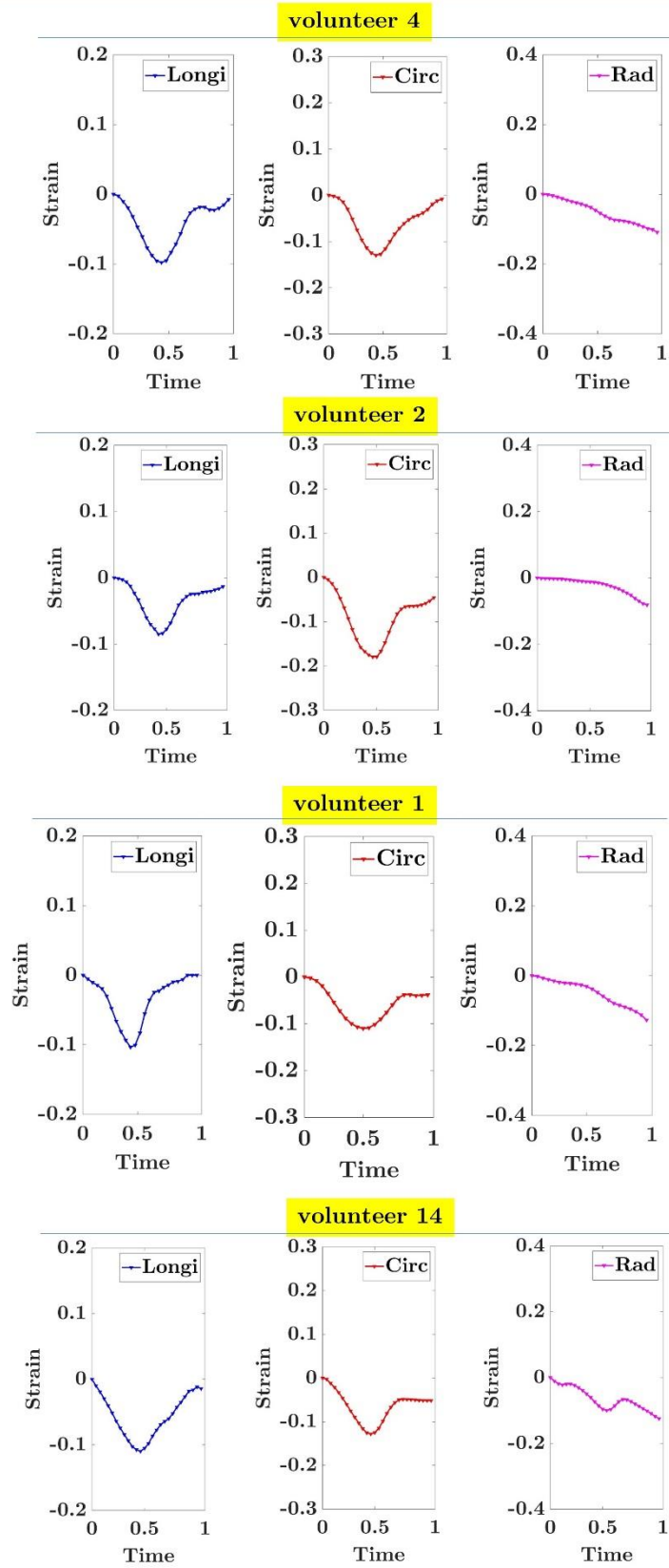
volunteer 14

3DTAG – Myocardial Strain
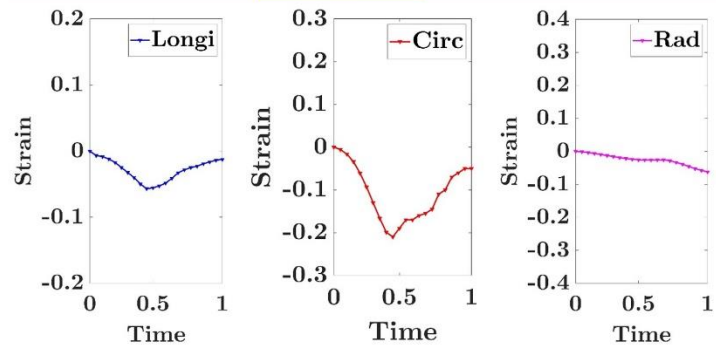
volunteer 5

volunteer 6
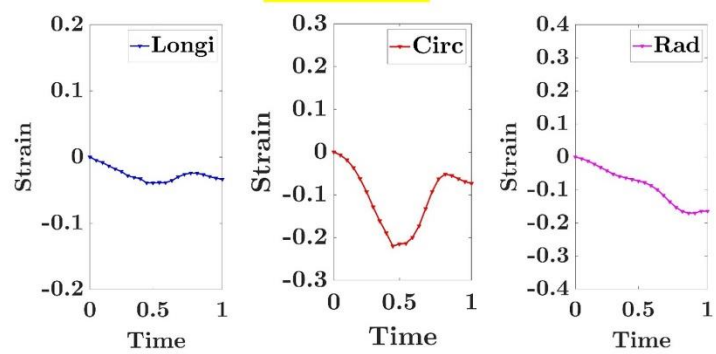
volunteer 7
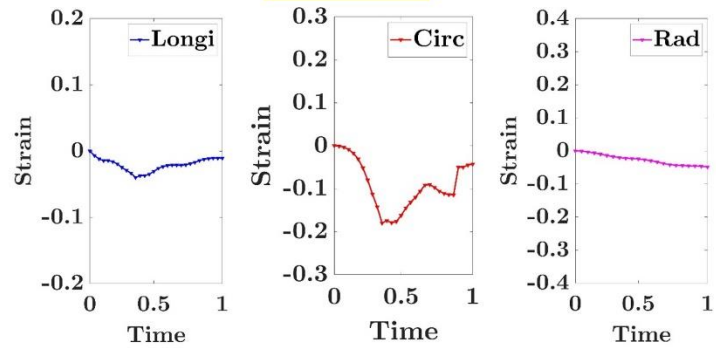
volunteer 9
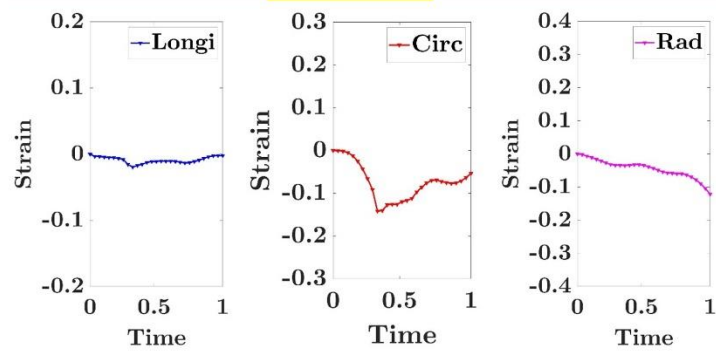
3DTAG − Myocardial Strain

volunteer 10
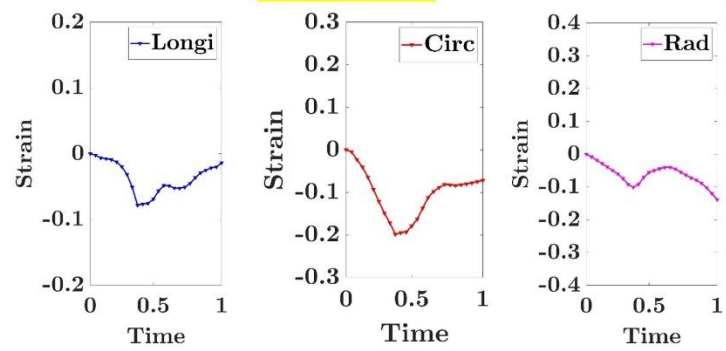
volunteer 11
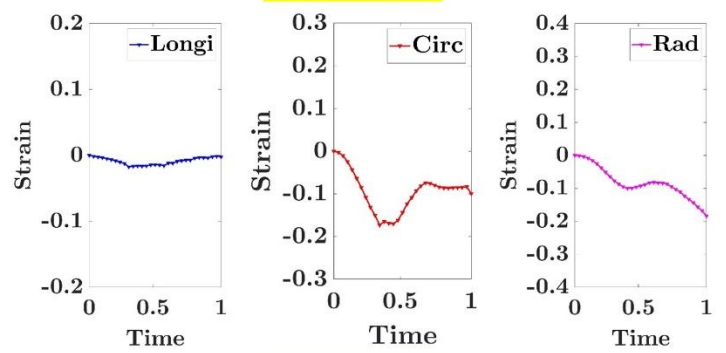
volunteer 12
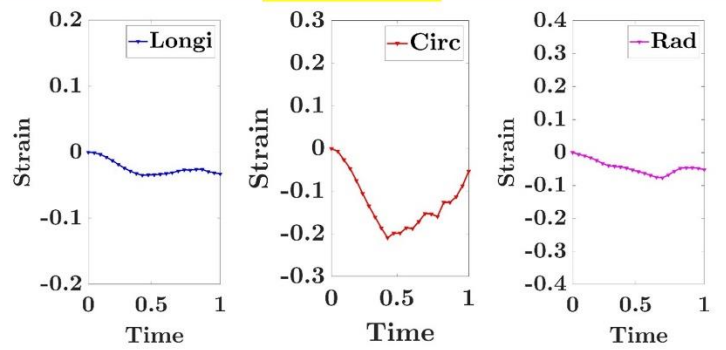
volunteer 13
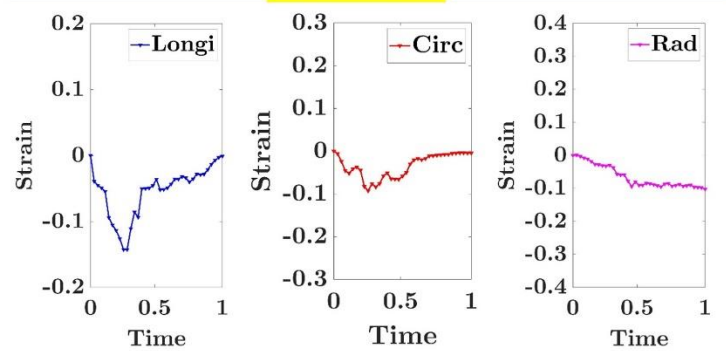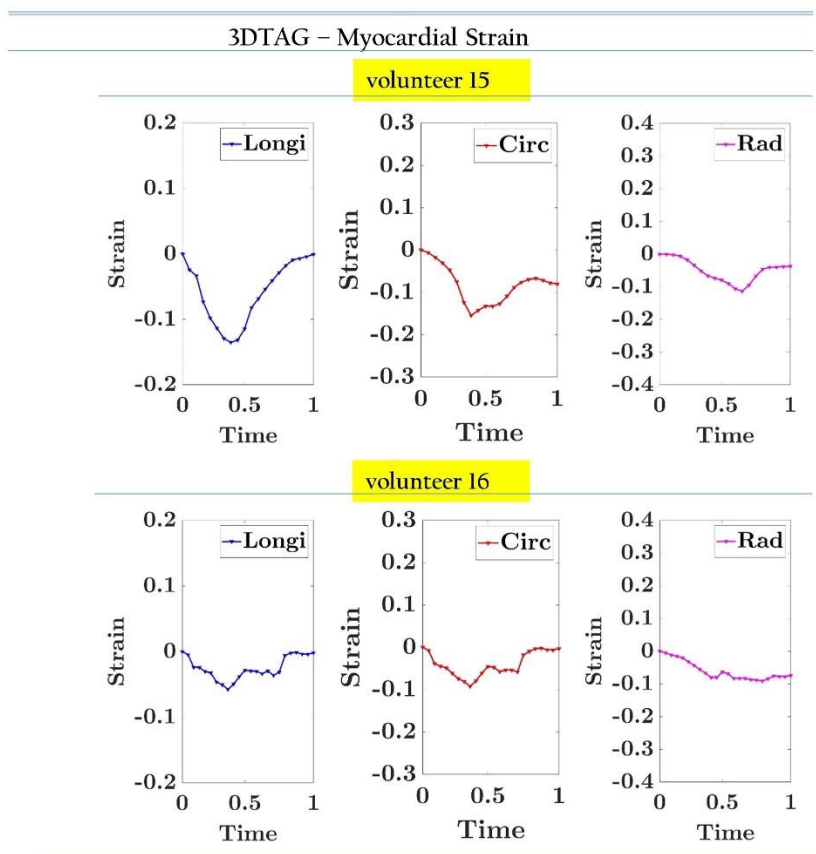
Figure 6.3| Strain plots of longitudinal, circumferential, and radial strain. Longi, Circ and Rad refer to longitudinal, circumferential, and radial strain, respectively.

As shown in Figure 6.3, the strain curves using all LV myocardial points are plotted with 3D data of patients. Longitudinal and circumferential strain curves are reported with negative values. End-systolic strain can be observed with peak values. The bell type of shape shows increasing strain in the beginning and decreasing strain in later cardiac cycle frames. Similar observations are reported in the literature (Tobon-Gomez, Craene, Mcleod, *et al.*, 2013).

Figure 6.4 shows the results of eigenvalue analysis in a patient V8.
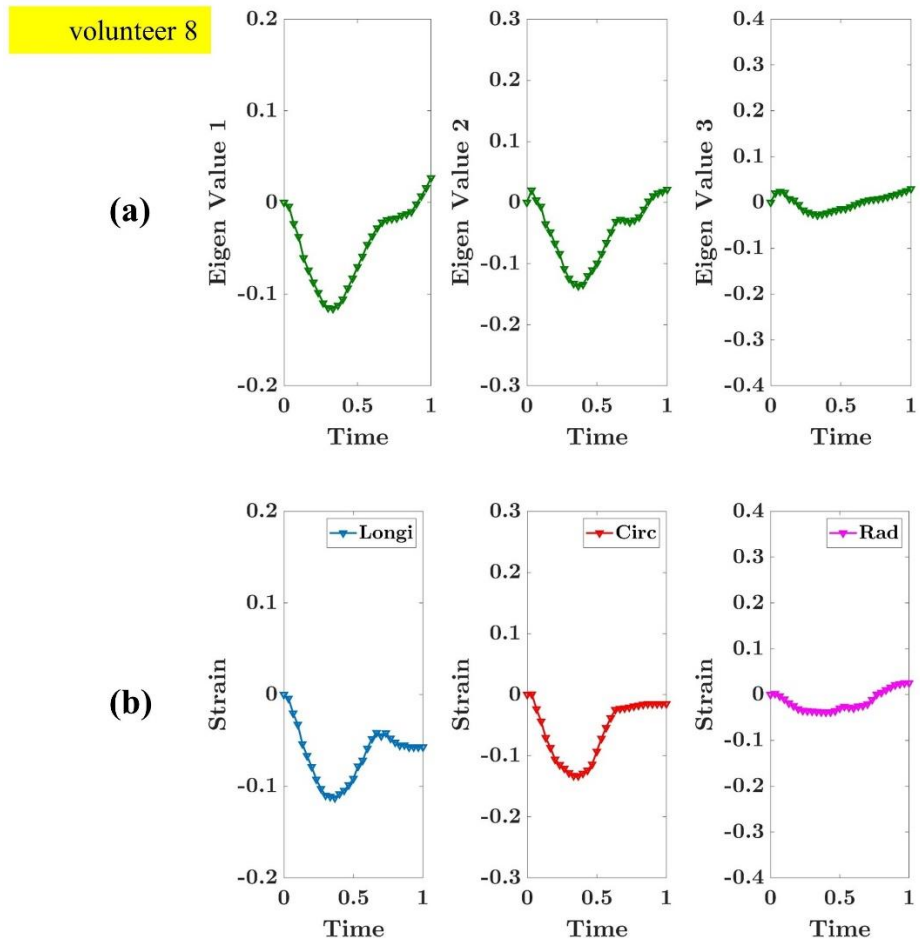
Figure 6.4| (a) Eigenvalue curves of patient V8, **(b)** strain value curves of patient V8. Rad, Circ, Longi refer to radial, circumferential, longitudinal strain, respectively.

As shown in Figure 6.4, the eigenvalue curves are reported with bell shape of increasing and decreasing values. Moreover, eigenvalue curves show end-systolic peak values similar to strain curves. Eigenvalue 1, eigenvalue 2, longitudinal strain and circumferential strain are noted similarly to physiological LV contraction and expansion. Eigenvalue 3 and radial strain are noted with almost zero values.

The discussion of 3D myocardial tracking and strain calculation results is included in the following section.

6.3 Discussion of results

3D myocardial tracking using HTM has reported a few advantages as follows: (i) numerical stability in the calculation which reported promising 3D tracking with $1.49mm$ median error and a very few outliers, (ii) 3D strain calculation can be performed at all the myocardial points without merging multiple methods or multiple 2D orientation images.

As shown in the results of Figure 6.1, 3D HTM has reported a similar median error to a benchmark method and half a millimetre higher error compared to the remaining benchmark methods. However, contrary to benchmark methods, 3D HTM does not have large error outliers at all frames, final frames and end-systolic frames. The reason is the technical advantages of HTM inherited from mathematically robust 3D LWM function. LWM function performs computation with a small number of polynomials and a system of equations, which provides LWM with the ability to avoid ill-conditioned polynomials (Goshtasby, 1988; Zagorchev and Goshtasby, 2006). Accordingly, the computation is numerically stable with fewer error outliers and lower maximum error.

Moreover, LWM can adapt to the various density of points and local geometrical variations in shape. Therefore, a specific coordinate system is not required, such as (Deng and Denney, 2004). Co-ordinate systems, like the Cartesian co-ordinate B-spline model, are prone to ill-conditioned polynomials and large error outliers (Deng and Denney, 2004).

Such limitations could be mitigated with LWM and, accordingly, 3D HTM. As shown in Figure 6.2, LV myocardial displacement is higher at the end-systolic frame and lower at the final frame. These results are aligned with the physiological ground truth of LV contraction and expansion, i.e. a healthy human heart LV

contracts maximum at end-systole to pump the blood out from LV (Katz, 2011). The smoothness of displacement agrees with the mathematical ability of the LWM function for providing smooth transformation, which is mentioned in Chapter 3 Equation 3.6. According to LV physiological behaviour (Katz, 2011), LV contracts in longitudinal and circumferential directions and expands in a radial direction during systole. As shown in Figure 6.4, the longitudinal and circumferential strain are reported with negative values, which agree with LV contraction. Moreover, the bell type of shape of strain curves agrees with LV contraction and expansion behaviour. However, the maximum values of strain are lower compared to the expected values. Expected values are -20% in circumferential (-0.20 circumferential strain), -16% in longitudinal (-0.16 longitudinal strain), and +45% in radial direction (+0.45 radial strain)(Tobon-Gomez, Craene, Mcleod, *et al.*, 2013). The reported circumferential and longitudinal values are almost half of the expected maximum values, and radial values are almost zero. The potential reasons could be a limitation of methodology or limitation of image acquisition protocol for 3D grid tagging MRI. A similar type of observation is reported by the researchers (Tobon-Gomez, Craene, Mcleod, *et al.*, 2013), who have used the same dataset in the literature.

To understand our results more in detail, we have performed an additional validation test based on eigenvalue analysis. The results are reported in Figure 6.3. Eigenvalue curve should also follow LV physiological behaviour because eigenvalues are components of principal strain (principal strain refers to the diagonal elements of strain tensor when off-diagonal (shear) components are zero). As shown in Figure 6.3, eigenvalue 1 and eigenvalue 2 curves have bell type shape, which agrees to LV contraction and expansion. Our results show that an eigenvalue less than zero leads to LV contraction, whereas literature (Gabriele, Nardinocchi and Varano, 2015) suggests that an

eigenvalue less than one shows LV contraction. This difference is because of the different definitions of strain tensors followed by both literature works (Tobon-Gomez, Craene, Mcleod, *et al.*, 2013; Gabriele, Nardinocchi and Varano, 2015). Eigenvalue 3 is reported with almost zero values. The maximum values of all three eigenvalue curves are lower than the literature (Gabriele, Nardinocchi and Varano, 2015).

These findings could be insightful to further improve 3D myocardial tracking and strain calculation. Circumferential, longitudinal, and radial strain directions are convenient for interpretation with clinical literature, and eigenvalue analysis of principal strain directions is insightful to understand results. Therefore, we have reported our results with both examples.

6.4 Summary

In this chapter, the results of 3D myocardial tracking and strain estimation are presented. An open-access 3D dataset is used (Tobon-Gomez, Craene, Mcleod, *et al.*, 2013). Comparative discussion with the benchmark methods is provided.

Chapter 7

Results - 2D Application Method for Myocardial Infarction Patients

7.1 Introduction

This chapter reports on the results of the 2D application method for myocardial infarction patients, as described in Chapter 4. Discussion of clinical validations is also presented in this chapter. The clinical dataset, validation methods, and image analysis methods are described in Chapter 4, Section 4.2 and Section 4.3. 2D application method and derived results are submitted in a journal article.

7.2 Results of the 2D application method for myocardial infarction patients

In this section, the results of identifying infarcted myocardial LV segments are reported. As detailed in Chapter 4 Section 4.2, the dataset of 43 subjects (38 myocardial infarction and 5 healthy) is divided into a training set and test set. The results derived with the training set to find $\propto_{correct}$ values for basal, mid-ventricular and apical slices are shown in Figure 7.1. These three $\propto_{correct}$ values are used with the test dataset, and the results are shown in Figure 7.2.

Figure 7.1 shows the results of detecting infarcted segments using the training dataset of k-fold tests with $k = 5$. $k = 5$ refers to 5% random data samples as test dataset. In Figure 7.1, the x-axis shows the $\propto$ value, and the y-axis shows the corresponding area under the curve (AUC) value. AUC values are derived from the ROC tests with training dataset and test dataset described in Chapter 4 Section 4.4.6.2. In summary, the ROC test calculates

sensitivity vs 1-specificity values and plots them as a curve, and the area under this curve is referred to as the AUC value. The ROC tests' input is infarcted LV segments identified in LGE imaging and corresponding infarcted LV segments identified using our method. The total number of infarcted segments in 38 MI patients is 109, and the total number of healthy segments is 579. The distribution of the infarcted segments and healthy segments per short-axis slice is (total: 109, basal: 38, mid-ventricular: 44, apical: 27), and (total: 579, basal: 220, mid-ventricular: 214, apical: 145), respectively. Among 579 healthy segments, 499 segments are from MI patients, and 80 segments are from healthy subjects. Healthy subjects do not have infarcted segments. Transmuralities of infarcts is not identified because our research question is limited to identify the infarcted LV segments only.
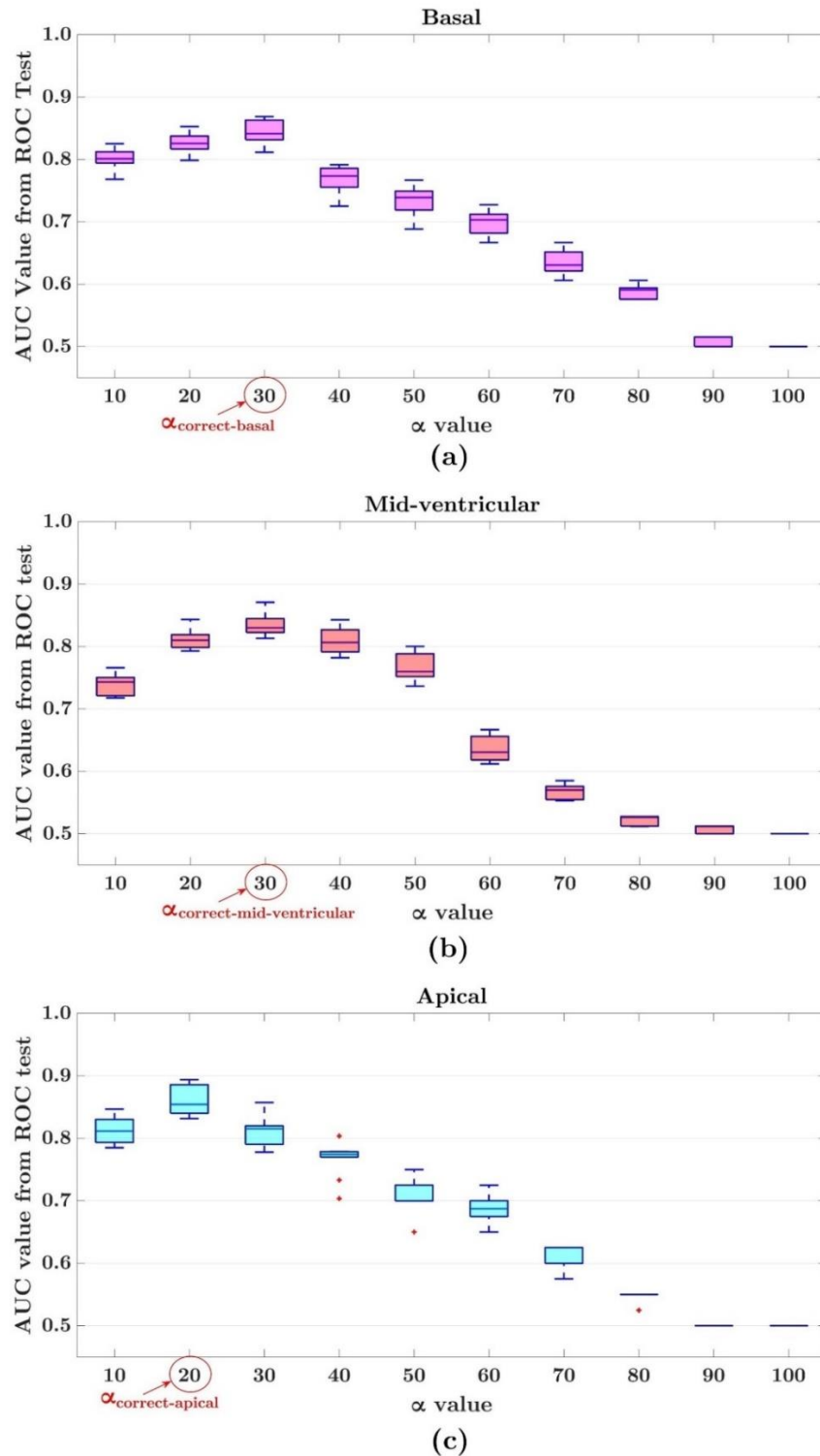
Figure 7.1| Results of 10 k-fold tests with different $\propto$ values in each short-axis slice **(a)** basal slice, **(b)** mid-ventricular slice, and **(c)** apical slice. AUC refers to the area under the curve of sensitivity vs 1-specificity curve as a ROC test output. $\propto_{correct}$ values correspond to the maximum AUC values in each slice.

As shown in Figure 7.1, AUC values corresponding to each $\propto$ value are shown in box-plots to find the maximum AUC value. Such maximum AUC has a corresponding $\propto$ value which is referred to as $\propto_{correct}$ value for each basal, mid-ventricular and apical SAX slice. According to that, $\propto_{correct-basal}=30$, $\propto_{correct-mid-ventricular}=30$, and $\propto_{correct-apical}=20$. Similar to that, it concludes that the strain H-spread of infarcted segments is at least 30% reduced in basal slices, at least 30% reduced in mid-ventricular slices, and at least 20% reduced in apical slices with respect to the H-spread of healthy segments in respective SAX slices. These $\propto_{correct}$ values are used with test datasets of k-fold tests. The results of AUC values with test datasets are shown in Figure 7.2.
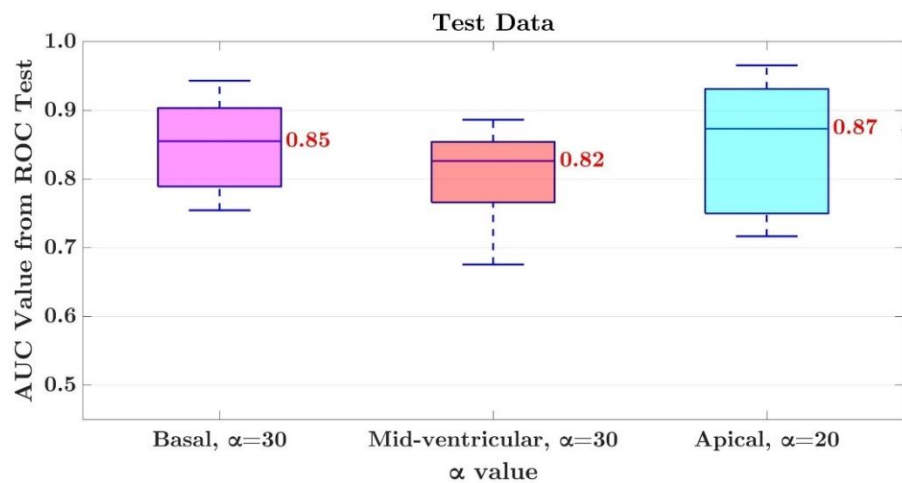
Figure 7.2| Accuracy of detecting infarcted LV segments in basal, mid-ventricular and apical slices using a test dataset. AUC refers to the area under the curve of sensitivity vs 1-specificity curve of detecting infarcted LV segments using our method and LGE imaging. $\propto$ values are $\propto_{correct}$ values found using the training dataset.

As shown in Figure 7.2, the basal slice has an accuracy of median AUC=0.85, the mid-ventricular slice has a median AUC=0.82, and the apical slice has a median AUC=0.87. Further, considering the mean values of AUC with 95% confidence level, the confidence

intervals of lower and upper AUC values in basal, mid-ventricular and apical slices are [0.80, 0.89], [0.74, 0.85], and [0.78, 0.91], respectively. The significance of the t-test (with results of 30 tests with randomly selected test data samples) shows that our method can significantly identify infarcted LV segments with AUC 0.73 (P=0.05) compared to LGE imaging. It has been hypothesised that the LGE imaging has 100% accuracy (i.e. AUC 1.0) in detecting infarcted LV segments, and accordingly, our method has AUC 0.73 with P=0.05. A patient-specific example of detections is shown in Table 7.1.

Table 7.1 | Example of detecting infarcted LV segments in an MI patient using our method compared to LGE imaging.

Patient Number					
D9		Truth (LGE imaging)		Detected (our method)	
		Infarcted?	Which segment?	Infarcted?	Which segment?
	Basal	Yes	1,2	Yes	1,2
	Mid-ventricular	Yes	7,8	Yes	7,8,12
	Apical	Yes	13,14	Yes	13,14,15

In Table 7.1, Truth refers to the clinical finding of LGE imaging and Detected relates to the results using the proposed method. An analysis summary of a test dataset is mentioned in Table 7.2.

Table 7.2 | Summary results of identifying infarcted LV segments in subjects of test dataset using our method. The base for comparison is LGE imaging.

Patient Number	Total LV Segments	Number of Infarcted Segments Identified in LGE Imaging	Performance of Identifying Infarcted Segments with Our Method					
			tp	tn	fp	fn	tpr = tp/(tp+fn) (sensitivity)	fpr = fp/(tn+fp) (1-specificity)
D1	16	5	3	9	2	2	0.75	0.18
D2	16	2	1	13	1	1	0.5	0.07
D3	16	1	1	12	3	0	0.5	0.2
D4	16	1	1	14	1	0	1	0.06
D5	16	2	2	14	0	0	0.25	0
D6	16	3	3	12	1	0	1	0.07
D7	16	7	5	9	0	2	1	0
D8	16	6	6	8	2	0	0.66	0.2
D9	16	5	5	11	0	0	1	0
H1	16	0	0	12	4	0	NaN	0.25
H2	16	0	0	16	0	0	NaN	0

tp=true positives, tn=true negatives, fp=false positives, fn=false negatives, tpr=true positive rate (sensitivity), fpr=false positive rate (1-specificity), D=diseased, H=healthy. Higher tpr and lower fpr together shows the best results (for example, D7, D9, H2).

In Table 7.2, higher true positive rate (tpr=1) and lower false-positive rate (fpr=0) together refers to ideal detections (same as LGE imaging) of infarcted LV segments in an MI patient, whereas in a healthy subject, fpr=0 is the perfect case of detections.

The sensitivity and 1-specificity of detecting infarcted LV segments with respect to LGE imaging are individually calculated for a test data set, which provides an overall sensitivity of 0.84 and specificity of 0.90 using our applied method.

An example of detecting infarcted LV segments using the clinical gold-standard LGE method and the proposed method is shown in Figure 7.3.
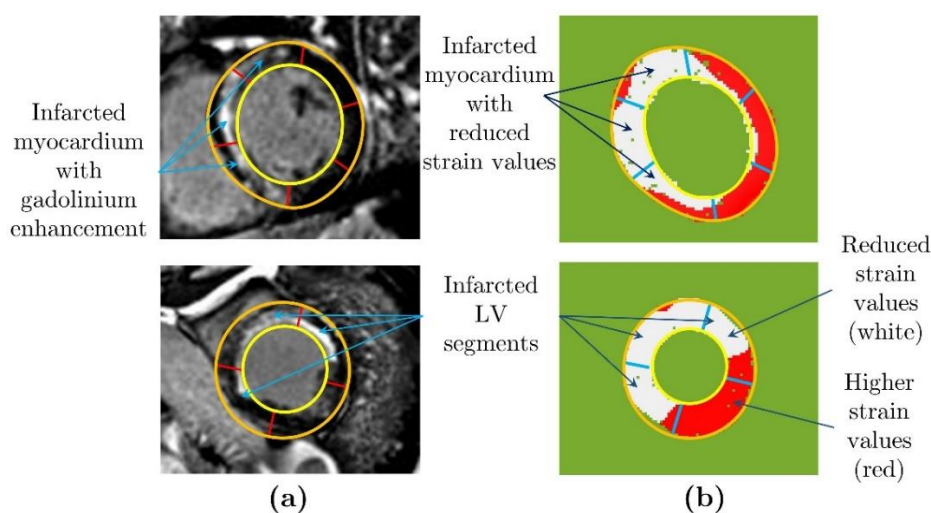
Figure 7.3| (a) Infarcted LV myocardial segments (white colour area) and healthy segments (black colour area) shown in LGE MRI findings, **(b)** infarcted LV myocardial segments (white colour area) and healthy segments (red colour area) shown with the proposed method.

As shown in Figure 7.3, LGE imaging findings show infarcted myocardium with enhancement (white colour), due to gadolinium deposition, and non-infarcted tissues without enhancement (black colour). A higher strain refers to healthy myocardium (red colour), and reduced strain values refer to infarcted myocardium (white colour) in the proposed method's results. Some of the segments have both red and white colour mixed. According to the infarction condition, such segments are decided as healthy or infarcted, as mentioned in Chapter 7 Section 7.3.6.

Strain values (end-systolic circumferential strain) calculated with the HTM method in healthy and infarcted LV segments are reported in Table 7.3.

Table 7.3 | Strain values in healthy and infarcted LV segments, and H-spread

End-systolic circumferential strain

LV segments of Basal slice as per AHA segments

	1	2	3	4	5	6	H-Spread
Healthy1	-0.01	-0.03	-0.03	-0.29	-0.02	-0.13	0.13
Healthy2	-0.04	-0.02	-0.36	-0.23	-0.05	-0.09	0.22
Healthy3	-0.06	-0.09	-0.1	-0.01	-0.34	-0.13	0.19
Healthy4	-0.07	-0.003	-0.09	-0.14	-0.12	-0.12	0.11
Healthy5	-0.06	-0.19	-0.35	-0.37	-0.29	-0.03	0.27
Infarcted1	-0.03	-0.02	-0.09	-0.08	-0.01	-0.03	0.07
Infarcted2	-0.03	-0.04	-0.02	**-0.02**	-0.04	-0.02	0.05
Infarcted3	-0.01	-0.03	-0.01	**-0.17**	-0.03	-0.15	0.09
Infarcted4	-0.07	**-0.02**	-0.08	-0.003	-0.07	-0.14	0.1
Infarcted5	-0.01	-0.02	-0.05	-0.001	-0.003	-0.08	0.05
Infarcted6	**-0.13**	**-0.01**	**-0.009**	-0.04	-0.15	-0.11	0.17
Infarcted7	-0.04	-0.04	-0.02	-0.01	-0.06	-0.02	0.07
Infarcted8	-0.1	-0.02	-0.07	-0.07	**-0.06**	-0.06	0.09
Infarcted9	**-0.06**	**-0.001**	-0.009	-0.08	-0.07	**-0.09**	0.07
Infarcted10	-0.04	-0.0006	-0.07	-0.01	-0.07	**-0.03**	0.1
Infarcted11	-0.1	-0.12	-0.11	-0.12	-0.15	-0.07	0.13
Infarcted12	-0.08	-0.01	-0.05	-0.09	-0.12	-0.12	0.1
Infarcted13	-0.13	-0.13	-0.08	-0.08	**-0.06**	**-0.02**	0.13
Infarcted14	-0.04	-0.19	-0.07	**-0.05**	-0.07	-0.06	0.15
Infarcted15	-0.15	-0.1	-0.13	**-0.17**	-0.22	-0.17	0.17
Infarcted16	-0.2	-0.11	-0.01	-0.02	-0.03	-0.05	0.11
Infarcted17	-0.08	-0.22	-0.03	-0.07	-0.15	-0.04	0.16

Red font refers to the infarcted segments and black font refers to the healthy segments

End-systolic circumferential strain

LV segments of Basal slice as per AHA segments

	1	2	3	4	5	6	H-Spread
Infarcted18	-0.03	**-0.02**	-0.05	-0.12	-0.12	**-0.04**	0.09
Infarcted19	-0.01	**-0.009**	-0.1	-0.13	-0.06	-0.07	0.1
Infarcted20	-0.12	-0.01	-0.06	-0.06	-0.11	-0.12	0.1
Infarcted21	-0.11	-0.01	-0.007	-0.04	**-0.15**	-0.13	0.08
Infarcted22	-0.13	**-0.13**	-0.2	-0.03	-0.05	-0.07	0.15
Infarcted23	-0.06	-0.01	-0.01	-0.09	-0.14	-0.14	0.09
Infarcted24	-0.16	-0.11	-0.07	-0.13	-0.19	-0.19	0.15
Infarcted25	-0.08	-0.07	-0.12	-0.13	-0.1	-0.15	0.12
Infarcted26	-0.06	-0.07	-0.11	-0.07	-0.16	-0.14	0.13
Infarcted27	-0.06	**-0.003**	-0.02	-0.07	-0.13	-0.12	0.1
Infarcted28	-0.05	-0.05	**-0.005**	**-0.04**	**-0.03**	**-0.05**	0.1
Infarcted29	-0.01	-0.06	-0.03	**-0.03**	-0.06	-0.04	0.06
Infarcted30	**-0.003**	-0.07	-0.04	-0.13	**-0.008**	**-0.009**	0.11
Infarcted31	-0.1	**-0.03**	**-0.04**	-0.13	-0.06	-0.02	0.11
Infarcted32	-0.05	**-0.03**	**-0.02**	-0.08	-0.02	-0.04	0.08
Infarcted33	-0.06	-0.01	-0.02	-0.02	-0.03	-0.04	0.06
Infarcted34	-0.12	**-0.09**	-0.11	-0.07	-0.002	**-0.02**	0.09
Infarcted35	-0.16	-0.09	**-0.01**	-0.09	-0.1	-0.15	0.13
Infarcted36	-0.16	-0.1	**-0.05**	-0.05	-0.04	-0.15	0.12
Infarcted37	**-0.06**	**-0.07**	-0.07	-0.02	-0.05	-0.15	0.11
Infarcted38	-0.09	-0.02	-0.007	-0.02	**-0.04**	**-0.05**	0.11

Red font refers to the infarcted segments and black font refers to the healthy segments

End-systolic circumferential strain

LV segments of Mid-ventricular slice as per AHA segments

	7	8	9	10	11	12	H-Spread
Healthy1	-0.03	-0.06	-0.002	-0.08	-0.21	-0.06	0.1
Healthy2	-0.12	-0.18	-0.02	-0.08	-0.01	-0.09	0.16
Healthy3	-0.17	-0.04	-0.08	-0.08	-0.1	-0.15	0.15
Healthy4	-0.05	-0.08	-0.07	-0.008	-0.08	-0.11	0.09
Healthy5	-0.003	-0.16	-0.27	-0.24	-0.08	-0.03	0.16
Infarcted1	-0.36	-0.25	-0.3	-0.11	-0.11	-0.11	0.29
Infarcted2	-0.13	-0.1	-0.03	-0.05	-0.21	-0.2	0.14
Infarcted3	-0.04	-0.12	-0.12	**-0.2**	-0.23	-0.11	0.15
Infarcted4	-0.01	-0.003	-0.04	-0.02	-0.13	-0.03	0.09
Infarcted5	**-0.07**	**-0.09**	**-0.01**	-0.04	-0.08	-0.0002	0.06
Infarcted6	**-0.004**	**-0.03**	**-0.05**	-0.08	-0.18	-0.1	0.17
Infarcted7	**-0.08**	**-0.06**	-0.05	-0.03	-0.04	-0.11	0.08
Infarcted8	-0.16	-0.06	-0.04	-0.03	**-0.05**	-0.07	0.11
Infarcted9	**-0.05**	-0.03	-0.06	-0.11	-0.11	**-0.12**	0.1
Infarcted10	-0.11	-0.17	-0.1	-0.09	-0.1	-0.07	0.16
Infarcted11	-0.09	-0.06	-0.07	-0.05	**-0.01**	-0.09	0.08
Infarcted12	-0.14	-0.03	-0.03	-0.07	-0.18	-0.2	0.13
Infarcted13	-0.14	-0.07	-0.08	-0.09	**-0.002**	-0.07	0.11
Infarcted14	-0.12	-0.1	-0.006	-0.04	-0.06	-0.03	0.07
Infarcted15	-0.12	-0.12	-0.2	-0.15	-0.19	-0.22	0.18
Infarcted16	-0.11	**-0.03**	-0.07	-0.09	-0.02	-0.005	0.08
Infarcted17	-0.02	**-0.07**	**-0.05**	-0.01	-0.03	-0.06	0.07

Red font refers to the infarcted segments and black font refers to the healthy segments

End-systolic circumferential strain

LV segments of Mid-ventricular slice as per AHA segments

	7	8	9	10	11	12	H-Spread
Infarcted18	-0.17	-0.13	-0.08	-0.05	-0.04	-0.1	0.11
Infarcted19	-0.03	-0.11	-0.04	-0.08	-0.09	-0.12	0.13
Infarcted20	-0.08	-0.2	-0.11	-0.08	**-0.02**	-0.09	0.15
Infarcted21	-0.1	-0.01	-0.01	-0.03	**-0.13**	-0.17	0.08
Infarcted22	-0.07	-0.1	-0.1	-0.16	-0.18	-0.07	0.14
Infarcted23	-0.08	**-0.06**	**-0.03**	-0.01	-0.04	-0.01	0.05
Infarcted24	-0.16	**-0.02**	-0.03	-0.12	-0.14	-0.18	0.14
Infarcted25	-0.13	-0.11	-0.19	-0.02	-0.04	**-0.03**	0.13
Infarcted26	-0.17	**-0.12**	**-0.02**	-0.09	-0.19	-0.1	0.17
Infarcted27	-0.07	**-0.05**	-0.08	-0.06	**-0.01**	**-0.05**	0.11
Infarcted28	-0.08	-0.1	**-0.04**	**-0.06**	**-0.05**	**-0.02**	0.13
Infarcted29	-0.06	-0.005	-0.06	-0.15	-0.12	-0.07	0.1
Infarcted30	**-0.12**	-0.07	-0.09	-0.14	**-0.04**	**-0.1**	0.13
Infarcted31	-0.15	-0.09	-0.06	-0.07	-0.16	-0.19	0.14
Infarcted32	-0.05	**-0.001**	-0.03	-0.08	-0.08	-0.04	0.08
Infarcted33	-0.16	-0.01	**-0.02**	**-0.07**	-0.07	-0.07	0.14
Infarcted34	-0.13	-0.03	-0.06	-0.06	-0.08	-0.15	0.12
Infarcted35	-0.09	-0.07	-0.003	-0.01	-0.14	-0.2	0.12
Infarcted36	-0.19	-0.16	-0.14	-0.11	-0.13	-0.11	0.17
Infarcted37	**-0.03**	**-0.01**	-0.03	-0.18	-0.17	-0.05	0.15
Infarcted38	-0.03	-0.003	-0.05	-0.002	**-0.01**	**-0.08**	0.03

Red font refers to the infarcted segments and black font refers to the healthy segments

End-systolic circumferential strain

LV segments of Apical slice as per AHA segments

	13	14	15	16	H-Spread
Healthy1	-0.05	-0.03	-0.12	-0.13	0.16
Healthy2	-0.02	-0.09	-0.05	-0.12	0.14
Healthy3	-0.08	-0.05	-0.09	-0.02	0.11
Healthy4	-0.06	-0.2	-0.13	-0.04	0.16
Healthy5	-0.08	-0.24	-0.028	-0.0004	0.23
Infarcted1	-0.11	**-0.01**	-0.02	-0.12	0.13
Infarcted2	-0.06	-0.06	-0.06	-0.08	0.08
Infarcted3	-0.18	-0.24	-0.15	-0.09	0.19
Infarcted4	-0.05	-0.02	-0.11	-0.13	0.14
Infarcted5	**-0.01**	**-0.01**	**-0.01**	-0.19	0.23
Infarcted6	**-0.01**	**-0.03**	-0.06	-0.08	0.1
Infarcted7	-0.01	**-0.03**	-0.08	-0.19	0.17
Infarcted8	-0.17	-0.14	**-0.05**	-0.01	0.15
Infarcted9	-0.07	-0.15	-0.23	-0.17	0.2
Infarcted10	-0.08	-0.07	-0.03	-0.004	0.08
Infarcted11	-0.01	-0.12	-0.09	**-0.1**	0.17
Infarcted12	-0.17	**-0.17**	**-0.21**	-0.19	0.21
Infarcted13	-0.19	-0.13	-0.08	**-0.01**	0.15
Infarcted14	-0.08	-0.04	-0.07	-0.09	0.12
Infarcted15	-0.0075	-0.002	-0.006	-0.04	0.04
Infarcted16	-0.14	-0.19	-0.06	-0.07	0.25
Infarcted17	-0.02	**-0.04**	-0.1	-0.02	0.12

Red font refers to the infarcted segments and black font refers to the healthy segments

End-systolic circumferential strain

LV segments of Apical slice as per AHA segments

	13	14	15	16	H-Spread
Infarcted18	-0.17	-0.23	-0.2	-0.03	0.21
Infarcted19	-0.15	-0.13	-0.1	-0.18	0.17
Infarcted20	-0.2	-0.19	-0.06	**-0.03**	0.21
Infarcted21	-0.04	-0.12	-0.22	-0.08	0.16
Infarcted22	-0.07	-0.11	-0.38	-0.25	0.28
Infarcted23	-0.04	**-0.02**	-0.05	-0.07	0.06
Infarcted24	-0.15	-0.16	-0.21	-0.23	0.22
Infarcted25	-0.05	-0.21	-0.03	**-0.08**	0.18
Infarcted26	-0.07	-0.03	-0.07	-0.13	0.1
Infarcted27	-0.05	-0.07	-0.17	**-0.07**	0.13
Infarcted28	-0.001	-0.1	**-0.05**	**-0.03**	0.12
Infarcted29	-0.01	-0.1	-0.11	-0.07	0.16
Infarcted30	-0.07	-0.19	-0.14	**-0.1**	0.17
Infarcted31	-0.15	-0.08	-0.21	-0.19	0.21
Infarcted32	-0.02	**-0.02**	-0.1	-0.09	0.11
Infarcted33	-0.17	-0.05	**-0.03**	-0.11	0.18
Infarcted34	-0.06	-0.09	-0.08	-0.003	0.08
Infarcted35	-0.13	-0.14	-0.16	-0.12	0.17
Infarcted36	-0.21	-0.15	-0.26	-0.2	0.24
Infarcted37	**-0.01**	**-0.009**	-0.01	-0.005	0.02
Infarcted38	-0.07	-0.04	**-0.04**	-0.08	0.07

Red font refers to the infarcted segments and black font refers to the healthy segments

The validity of the results is reported in the discussion section of this chapter.

7.3 Discussion of results

The method for detecting infarcted LV segments is applied, fundamentally based on the 2D HTM method. Therefore, it inherits the strengths and limitations of 2D HTM. In Chapter 2, 2D HTM is described with Eulerian strain definition, an adopted strain calculation step from the literature. In Chapter 4, the 2D application method is described with the Lagrange strain definition, which is also an adopted strain calculation step from the literature (Tobon-Gomez, Craene, Mcleod, *et al.*, 2013). These Lagrange strain values in each LV segments are shown in Table 7.3. To validate and ensure consistency of our strain values with literature, we have incorporated the first step of our 2D application method as comparing end-systolic circumferential strain values with literature (Moore, Lugo-Olivieri, McVeigh, *et al.*, 2000). The strain values reported in that literature is calculated using semi-automatic myocardial tracking with manual corrections. Therefore, those values can be used for comparison. Besides, they have used the same imaging modality as ours for strain calculation, which is grid tagging MRI.

Moreover, the same literature (Moore, Lugo-Olivieri, McVeigh, *et al.*, 2000) is referred to by the benchmark framework (Tobon-Gomez, Craene, Mcleod, *et al.*, 2013) while discussing the validation of end-systolic peak strain values of the 3D myocardial tracking and strain calculation methods. Therefore, we have compared our strain values with the same literature to validate our end-systolic strain values in the application method. However, the human subjects dataset used in that literature (Moore, Lugo-Olivieri, McVeigh, *et al.*, 2000), is different from our dataset, limiting the comparison. That literature has used 31 healthy volunteers, whereas we have used 5 healthy and 38 myocardial infarction patients. Due to this difference, we have not entirely relied on only end-systolic strain comparison. Our

method utilises the H-spread of strain value in healthy LV segments and infarcted LV segments within the same patient. As these H-spread is compared within the patient and not with literature data, they can be reliable. Within the same patient, infarcted muscle are clinically known to have reduced strain compared to healthy muscle. This limitation could be mitigated or overcome in future after the clinical consensus (standardisation of the utility of strain by global clinical committees). Currently, the strain-based methods are emerging research and lack of standardised strain values. After the clinical researchers standardise the clinical utility of strain values, the proposed method will need to be updated with new strain values. Accordingly, the updated results will need to be reported.

As shown in Figure 7.1 and Figure 7.2, the proposed method has analysed the infarcted segments at three different LV levels, which are basal, mid-ventricular and apical. The reason is that the mechanics of the myocardium is non-uniform throughout the LV. At the end-systolic phase of LV, the basal, mid-ventricular and apical areas contract an average of 18.5%, 19.25%, and 22.25%, respectively (Moore, Lugo-Olivieri, McVeigh, *et al.*, 2000). Accordingly, three separate $\propto_{correct}$ values are found which are $\propto_{correct-basal}= 30$, $\propto_{correct-mid-ventricular}= 30$, and $\propto_{correct-apical}= 20$. These values show that the circumferential strain H-spread of infarcted LV segments in basal, mid-ventricular and apical areas is reduced 30%, 30%, and 20%, respective, compared to healthy LV segments of the same slice. The difference among them is due to partially infarcted LV segments. In the proposed method, the comparison of healthy and infarcted segments are happening within the same slice. If all the same slice segments are infarcted, then the comparison is extended with healthy segments of other LV slices, detailed in Chapter 4 Section 4.4.6.1 (Equation 4.6).

Figure 7.2 shows different accuracy for each LV level and Table 7.2 shows that some of the infarcted segments are detected as healthy, causing false negatives in detection. This difference and limitation could be due to the fundamental texture tracking nature of the 2D HTM method, which may cause incorrect tracking and detection. As the 2D HTM method tracks the image texture, it could be affected by faded images or artefacts, which could happen due to blood flow or patient breathing or patient movement. Low-quality images lead to incorrect myocardial tracking using HTM, resulting in an error in calculated strain values and erroneous detections of infarcted LV segments. Table 7.2 shows the results of a test dataset of 9 infarcted patients and 2 healthy subjects. In healthy subjects, true positives and false negatives are zero, and the true positive rate is not a number (NaN), as healthy subjects do not have infarcted segments. However, false-positive detections are reported, potentially due to reduced strain values, calculated by HTM.

As shown in Figure 7.3 and Table 7.1, the method's potential implication could be in identifying infarcted LV segments without using the GBCA-based LGE method. Such advantages can extend the utility of MRI in detecting infarcted LV segments, specifically in renal impairment patients, as they are clinically contra-indicated to the use of GBCA due to patient safety concerns (McDonald, McDonald, Kallmes, *et al.*, 2015). Moreover, the patient care concerns of gadolinium deposition in tissues and bones (McDonald, McDonald, Kallmes, *et al.*, 2015) could be avoided with the proposed application method. Moreover, GBCA usage costs an additional €50 per patient MRI (Boldt, Leber, Bonaventura, *et al.*, 2013); hence, avoiding GBCA could be more economical. A practical limitation of this method could be grid tagging MRI. Grid tagging MRI requires a patient to hold the breath to capture good quality images. If the patient finds it difficult to control the breath, then there could be blur texture of

images which may give an error in myocardial tracking and strain.

The proposed method is limited to detecting infarcted LV segments only. In contrast, the current gold-standard LGE imaging can provide higher accuracy, such as detecting sub-endocardial infarction and separating transmural and non-transmural infarctions. Therefore, the proposed method will need to be improved and validated with more datasets and clinical studies. Moreover, the proposed method could detect infarcted LV segments only in basal, mid-ventricular and apical slices. Therefore, a potential future work could be extending the method for detecting infarcted myocardium in the entire LV volume. The proposed method is limited to the LV classification according to the 16-segment AHA model, which could be adapted for different LV model after a rigorous literature review to find appropriate strain value ranges.

7.4 Summary

In this chapter, identifying infarcted LV segments using 2D application method is reported with respect to the LGE imaging. The area under the curve of sensitivity vs 1-specificity curve is used to show the method's performance. Circumferential strain values of healthy and infarcted LV segments are reported. A discussion of results and potential clinical implications are provided.

Chapter 8

Conclusion

8.1 Introduction

This thesis aims to create a safe diagnostic tool without using a gadolinium-based contrast agent. It is shown, within the thesis, that the strain analysis based method can help in identifying infarcted myocardial segments, which are crucial findings in diagnosing myocardial infarction patients.

In this thesis, the following research problem is addressed:

How can a myocardial tracking and strain calculation tool be developed to calculate myocardial strain to safely and accurately aid diagnostic decisions of myocardial infarction patients?

Three research questions have been formulated to address this research problem, following a clinical and technical literature review. A novel method - Hierarchical Template Matching has been proposed for 2D and 3D myocardial tracking. A clinical application method to use 2D circumferential strain in identifying infarcted left ventricular segments has been described, and results are derived with a clinical dataset of myocardial infarction patients. A summary of key findings is presented in this chapter with potential clinical implications and future work direction.

8.2 Key research findings

This thesis has addressed three research questions, and key findings with each research question are as follows:

Research question 1: How can a 2D myocardial tracking and strain calculation method be developed using the 2D local weighted mean function and structural deformation within the myocardium?

A novel method – Hierarchical Template Matching (HTM) has been proposed to perform 2D myocardial tracking to address this research question. HTM utilises grid tagging MRI to include the details of structural deformation within the myocardium. The method is validated at basal, mid-ventricular, upper mid-ventricular and apical left ventricular slices using target registration error, with respect to the manually tracked myocardial points of grid tagging MRI. It is found that the root mean square error of the HTM in tracking LV myocardium is: basal 0.31 ± 0.07 mm, upper mid-ventricular 0.37 ± 0.06 mm, mid-ventricular 0.41 ± 0.05 mm, and apical 0.32 ± 0.08 mm. The mid-ventricular slice has a significantly 4% (P=0.05) higher tracking error compared to other slices. However, other slices do not have a significant difference among them. The overall tracking error of HTM is 0.35 ± 0.05 mm, which is 17% (P=0.07, CI:[-0.01, 0.35]) reduced compared to the benchmark method – free form deformation (FFD). The reason for this is the difference in transformation function in HTM and FFD. HTM uses the local weighted mean (LWM) transformation function while computation, whereas FFD uses a spline-based function. A list of advantages of LWM is detailed in Chapter 1, Section 1.3.3.3.

Research question 2: How can a 3D myocardial tracking and strain calculation method be developed using the 3D local weighted mean function to calculate 3D myocardial strain?
We have extended our HTM method for 3D to address this research question and introduced the 3D extension of the LWM function in the 3D myocardial tracking and strain calculation pipeline. As described in Chapter 1, Section 1.3.2.2.2, many methods, reported in the literature, require multiple 2D orientation images or tissue material properties to calculate 3D strain. In comparison, we have shown 3D strain calculation by utilising direct 3D images and without requiring tissue material

properties. Results of 3D HTM are validated with the benchmark framework (Tobon-Gomez, Craene, Mcleod, *et al.*, 2013). We found that our method does not have better accuracy in terms of myocardial point tracking's median error. Our tracking error is 1.49 mm, whereas benchmark methods have a tracking error of 1.33 mm (MEVIS), 1.52 mm (IUCL), 1.09 mm (UPF), and 1.32 mm (INRIA). However, benchmark methods have reported a large number of outliers, whereas HTM has a few outliers. This advantage is mainly due to the 3D LWM function used in HTM. LWM can avoid errors of ill-conditioned polynomials during computation, and as a result, the error outliers are very few. Due to the inaccessibility of all the error values from the benchmark framework, we are unable to do the significance test. The strain values with HTM and with benchmark methods are less than the expected strain values as discussed in Chapter 6 Section 6.3, which shows further to improve 3D myocardial tracking and strain calculation methods.

Research question 3: How can 2D circumferential strain of myocardium be used in identifying infarcted left ventricular segments for the diagnosis of myocardial infarction patients? In this research question, we have addressed to develop an applied method using strain values calculated by HTM. We have used grid-tagging MRI-based circumferential strain values. We show that the infarcted left ventricular segments can be identified with strain H-spread from end-diastolic to end-systolic cardiac frames without using a gadolinium-based contrast agent. We compare our results with LGE imaging. Our method's performance is reported in terms of the area under the curve (AUC) of sensitivity vs 1-specificity of a ROC test. For LV segments in the basal slice, we have achieved an accuracy of AUC 0.85. For the mid-ventricular slice, AUC is 0.82, and for the apical slice, AUC is 0.87. Calculating AUC with 95% confidence level, the

confidence intervals of lower and upper mean AUC values in basal, mid-ventricular and apical slices are [0.80, 0.89], [0.74, 0.85], and [0.78, 0.91], respectively. Moreover, our method has AUC 0.73 (P=0.05) in detecting infarcted left ventricular segments with respect to LGE imaging. Our method does not require a gadolinium-based contrast agent. Hence, it is safe. However, our method does not separate transmural and non-transmural infarction, which is discussed in limitations.

8.3 Potential implications

The research described in this thesis is aiming to reduce the mortality and morbidity regarding cardiovascular diseases. The addressed research problem is centred around developing a diagnostic tool to aid clinical decisions with better patient safety and care. The overall research has shown technical and clinical methods to create a diagnostic tool. The clinical method is reported with preliminary results of detecting infarcted myocardium in myocardial infarction (myocardial infarction) patients.

The described method shows that the circumferential strain analysis can identify the infarcted myocardium. The method does not require GBCA injection, which helps to overcome patient safety concerns and mitigate patient care concerns compared to current clinical practice. The described method could be offered in clinical condition, such as advanced renal impairment, which is contraindicated with the GBCA-based LGE imaging. Moreover, the GBCA usage increases the cost by approximately €50 per patient for LGE imaging. Therefore, the described method could be more economical in practice.

The described tool is in its early stage of research, and it has several limitations as well, which are described in Section 8.4.

8.4 Limitations of the research

This research is limited to the myocardial strain-based diagnostic tools, and precisely, image processing-based tools. Regarding clinical conditions, the research is limited to myocardial infarction patients, specifically identifying infarcted LV segments, only in three SAX slices, i.e. basal, mid-ventricular, and apical slices. The research is based at a non-clinical organisation, limited to method developments. Dataset of myocardial infarction patients is collected from a clinical unit. However, the research does not represent a clinical study. The number of data samples is limited to only one clinical centre, and it does not have multi-centre clinical data. The technical validations are limited to the benchmark methods of literature and a limited number of data samples from healthy subjects. The described methods are not ready to use in clinical units, though it has shown early-stage promising results. The code developed during the research is limited to academic research.

8.5 Future Work

As future work, performing the 3D application method would be a relevant task. In specific, collecting 3D data of myocardial infarction patients and then developing a clinical application method to verify and validate the usage of the proposed 3D method would be relevant. Moreover, the 3D LWM function, which is mentioned in Chapter 3, as a part of the 3D method, would be used with 3D Echo data to perform speckle tracking-based myocardial tracking. This future work should be performed before proceeding to the 3D clinical application work because these findings would be insightful to improve the 3D technical method further. The 3D strain value curves would be developed using Echo data of the same patients as MRI to enable comparative analysis of myocardial tracking accuracy.

Regarding the 2D application method, even though it has better patient safety than LGE imaging, the accuracy is still not as good as the current gold-standard LGE imaging. For example, LGE imaging can identify the transmurality of an infarct, and it can locate sub-endocardial infarction. Such accuracy is not observed in our results, which suggests improving technical and clinical application methods before proceeding to the clinical studies.

From the point of view of strain components, the proposed method has utilised circumferential strain. The methods have used grid tagging MRI (2D SAX slices in the 2D method and 3D volumes in the 3D method), which is accurate to capture circumferential motion. As future work, the strain components such as radial strain, longitudinal strain, the shear strain could be calculated by merging multiple imaging modalities. For example, cine MRI could capture radial motion more accurately than grid tagging MRI and could be integrated with grid tagging MRI using MRI header information. Also, 2D LAX slices can be promising to capture longitudinal strain, which would be interesting to explore as future work.

Future work for associated clinical studies would potentially include collecting a dataset of myocardial infarction patients from multiple clinical institutes, with patient data comprised of different geographical locations, age groups, sex, and imaging scanners. Such datasets would be used to validate the methods with respect to the gold-standard LGE imaging. Later, the validation results would be used to revise the developed procedures, followed by validation and standard diagnostic tool development.

Bibliography and References

Abd-elmoniem, K. Z., Stuber, M. and Prince, J. L. (2008) 'Direct three-dimensional myocardial strain tensor quantification and tracking using z HARP', *Medical Image Analysis*, 12(6), pp. 778–786. doi: 10.1016/j.media.2008.03.008.

Amini, A. A., Chen, Y., Elayyadi, M., *et al.* (2001) 'Tag surface reconstruction and tracking of myocardial beads from SPAMM-MRI with parametric B-spline surfaces', *IEEE Transactions on Medical Imaging*, 20(2), pp. 94–103. doi: 10.1109/42.913176.

Angelini, E. D. and Gerard, O. (2006) 'Review of myocardial motion estimation methods from optical flow tracking on ultrasound data', *Annual International Conference of the IEEE Engineering in Medicine and Biology*, pp. 1537–1540. doi: 10.1109/IEMBS.2006.259640.

Arts, T., Prinzen, F. W., Delhaas, T., *et al.* (2010) 'Mapping displacement and deformation of the heart with local sine-wave modeling', *IEEE Transactions on Medical Imaging*, 29(5), pp. 1114–1123. doi: 10.1109/TMI.2009.2037955.

Azevedo, P. S., Polegato, B. F., Minicucci, M. F., *et al.* (2016) 'Cardiac Remodeling: Concepts, Clinical Impact, Pathophysiological Mechanisms and Pharmacologic Treatment', *Arquivos Brasileiros de Cardiologia*, pp. 62–69. doi: 10.5935/abc.20160005.

B., S. D. and Joseph, L. (2002) 'Myocardial Hibernation', *Circulation*, 105(13), pp. 1517–1519. doi: 10.1161/01.CIR.0000014689.12415.89.

Bardinet, E., Cohen, L. D. and Ayache, N. (1996) 'Tracking and motion analysis of the left ventricle with deformable superquadrics.', *Medical image analysis*, 1(2), pp. 129–149. doi: 10.1016/S1361-8415(96)80009-0.

Bhalodiya, J. M., Palit, A., Tiwari, M. K., *et al.* (2018) 'A Novel Hierarchical Template Matching Model for Cardiac Motion Estimation', *Scientific Reports*, 8(1), p. 4475. doi: 10.1038/s41598-018-22543-y.

Bhalodiya, J. M., Palit, A., Ferrante, E., *et al.* (2019) 'Hierarchical Template Matching for 3D Myocardial Tracking and Cardiac Strain Estimation', *Scientific Reports*, 9(1), p. 12450. doi: 10.1038/s41598-019-48927-2.

Bhalodiya, J. M., Palit, A., Giblin, G., *et al.* (2021) 'Identifying Myocardial Infarction Using Hierarchical Template Matching–Based Myocardial Strain: Algorithm Development and Usability Study', *JMIR Med Inform*, 9(2), p. e22164. doi: 10.2196/22164.

BHF (2019) *Cardiovascular Disease Statistics*. Available at: https://www.bhf.org.uk/for-professionals/press-centre/facts-and-figures.

Bleumke, D. A. and Pattanayak, P. (2015) 'Tissue Characterization of the Myocardium: State of the Art Characterization by Magnetic Resonance and Computed Tomography Imaging', *Radiologic Clinics of North America*, 53(2), pp. 413–423. doi: https://doi.org/10.1016/j.rcl.2014.11.005.

Boldt, J., Leber, A. W., Bonaventura, K., *et al.* (2013) 'Cost-effectiveness of cardiovascular magnetic resonance and single-photon emission computed tomography for diagnosis of coronary artery disease in Germany', *Journal of Cardiovascular Magnetic Resonance*, 15(1). doi: 10.1186/1532-429X-15-30.

Bruder, O., Schneider, S., Nothnagel, D., *et al.* (2011) 'Acute Adverse Reactions to Gadolinium-Based Contrast Agents in CMR', *JACC: Cardiovascular Imaging*, 4(11), pp. 1171–1176. doi: 10.1016/j.jcmg.2011.06.019.

Captur, G., Lobascio, I., Ye, Y., *et al.* (2019) 'Motion-corrected free-

breathing LGE delivers high quality imaging and reduces scan time by half: an independent validation study', *International Journal of Cardiovascular Imaging*, 35(10), pp. 1893–1901. doi: 10.1007/s10554-019-01620-x.

CDC, N. (2015) *Underlying Cause of Death 1999-2013 on CDC WONDER Online Database*. Available at: https://wonder.cdc.gov/ucd-icd10.html.

Cerqueira, M. D. ., Weissman, N. J. ., Dilsizian, V., *et al.* (2002) 'Standardized Myocardial Segmentation and Nomenclature for Tomographic Imaging of the Heart: A Statement for Healthcare Professionals From the Cardiac Imaging Committee of the Council on Clinical Cardiology of the American Heart Association', *Circulation*, 105(4). doi: 10.1161/hc0402.102975.

Chandrashekara, R., Mohiaddin, R. H. and Rueckert, D. (2004) 'Analysis of 3-D myocardial motion in tagged MR images using nonrigid image registration', *IEEE Transactions on Medical Imaging*, 23(10), pp. 1245–1250. doi: 10.1109/TMI.2004.834607.

Chen, T., Wang, X., Chung, S., *et al.* (2010) 'Automated 3D motion tracking using gabor filter bank, robust point matching, and deformable models', *IEEE Transactions on Medical Imaging*, 29(1), pp. 1–11. doi: 10.1109/TMI.2009.2021041.

Chotenimitkhun, R. and Hundley, W. G. (2011) 'Pharmacological stress cardiovascular magnetic resonance', *Postgraduate medicine*, 123(3), pp. 162–170. doi: 10.3810/pgm.2011.05.2295.

Collignon, A., Maes, F., Delaere, D., *et al.* (1995) 'Automated multi-modality image registration based on information theory', *Information processing in medical imaging*, 3(6), pp. 263–274. doi: 10.1007/11784012_16.

Crosby, J., Amundsen, B. H., Hergum, T., *et al.* (2009) '3-D Speckle Tracking for Assessment of Regional Left Ventricular Function',

Ultrasound in Medicine & Biology, 35(3), pp. 458–471. doi: 10.1016/J.ULTRASMEDBIO.2008.09.011.

Cui, C., Wang, S., Lu, M., *et al.* (2018) 'Detection of Recent Myocardial Infarction Using Native T1 Mapping in a Swine Model : A Validation Study', *Scientific Reports*, (May 2017), pp. 1–10. doi: 10.1038/s41598-018-25693-1.

Deng, X. and Denney, T. S. (2004) 'Three-Dimensional Myocardial Strain Reconstruction Model', *IEEE Transactions on Medical Imaging*, 23(7), pp. 861–867.

Ergün, I., Keven, K., Uruç, I., *et al.* (2005) 'The safety of gadolinium in patients with stage 3 and 4 renal failure', *Nephrology Dialysis Transplantation*, 21(3), pp. 697–700. doi: 10.1093/ndt/gfi304.

Evangelista, A., Gabriele, S., Nardinocchi, P., *et al.* (2015) 'Non-invasive assessment of functional strain lines in the real human left ventricle via speckle tracking echocardiography', *Journal of Biomechanics*, 48(3), pp. 465–471. doi: 10.1016/j.jbiomech.2014.12.028.

Evangelista, A., Gabriele, S., Nardinocchi, P., *et al.* (2016) 'A comparative analysis of the strain-line pattern in the human left ventricle: experiments vs modelling', *Computer Methods in Biomechanics and Biomedical Engineering: Imaging and Visualization*, 4(3–4), pp. 164–173. doi: 10.1080/21681163.2014.927741.

Fitzpatrick, J. M. and West, J. B. (2001) 'The Distribution of Target Registration Error in Rigid-Body Point-Based Registration', *IEEE Transactions on Medical Imaging*, 20(9), pp. 917–927.

Flachskampf, F. A., Schmid, M., Rost, C., *et al.* (2011) 'Cardiac imaging after myocardial infarction', *European Heart Journal*, 32(3), pp. 272–283. doi: 10.1093/eurheartj/ehq446.

Flett, A. S., Hasleton, J., Cook, C., *et al.* (2011) 'Evaluation of

techniques for the quantification of myocardial scar of differing etiology using cardiac magnetic resonance', *JACC: Cardiovascular Imaging*, 4(2), pp. 150–156. doi: 10.1016/j.jcmg.2010.11.015.

Franco, A., Javidi, S. and Ruehm, S. G. (2015) 'Delayed myocardial enhancement in cardiac magnetic resonance imaging', *Journal of Radiology Case Reports*, 9(6), pp. 6–18. doi: 10.3941/jrcr.v9i6.2328.

Frangi, A. F., Niessen, W. J. and Viergever, M. A. (2001) 'Three-dimensional modeling for functional analysis of cardiac images: A review', *IEEE Transactions on Medical Imaging*, 20(1), pp. 2–25. doi: 10.1109/42.906421.

Gabriele, S., Nardinocchi, P. and Varano, V. (2015) 'Evaluation of the strain-line patterns in a human left ventricle: a simulation study', *Computer Methods in Biomechanics and Biomedical Engineering*, 18(7), pp. 790–798. doi: 10.1080/10255842.2013.847094.

Gavara, J., Rodriguez-Palomares, J. F., Valente, F., *et al.* (2018) 'Prognostic Value of Strain by Tissue Tracking Cardiac Magnetic Resonance After ST-Segment Elevation Myocardial Infarction', *JACC: Cardiovascular Imaging*, 11(10), pp. 1448–1457. doi: 10.1016/j.jcmg.2017.09.017.

Goldwasser, D., Elizari, M. V. and Bayés de Luna, A. (2017) 'Chronic Myocardial Infarction', *Circulation*, 136(10), pp. 966–968. doi: 10.1161/CIRCULATIONAHA.117.029565.

Gorcsan, J. and Tanaka, H. (2011) 'Echocardiographic Assessment of Myocardial Strain', *Journal of the American College of Cardiology*, 58(14), pp. 1401 LP – 1413. Available at: http://www.onlinejacc.org/content/58/14/1401.abstract.

Goshtasby, A. (1988) 'Image registration by local approx methods', *Image and Vision Computing*, 6(4), pp. 255–261.

Grobner, T. (2006) 'Gadolinium – a specific trigger for the development of nephrogenic fibrosing dermopathy and nephrogenic systemic fibrosis?', *Nephrology Dialysis Transplantation*, 21(4), pp. 1104–1108. doi: 10.1093/ndt/gfk062.

GUSTO (1993) 'The Effects of Tissue Plasminogen Activator, Streptokinase, or Both on Coronary-Artery Patency, Ventricular Function, and Survival after Acute Myocardial Infarction', *New England Journal of Medicine*, 329(22), pp. 1615–1622. doi: 10.1056/NEJM199311253292204.

Guttman, M. A., Zerhouni, E. A. and McVeigh, E. R. (1997) 'Analysis of Cardiac Function from MR Images', *IEEE computer graphics and applications*, 17(1), pp. 30–38. doi: 10.1109/38.576854.

Guyton, A. C. and Hall, J. E. (2011) *Textbook of medical physiology guyton and hall*. 12th edn. Philadelphia.

Hajian-Tilaki, K. (2013) 'Receiver operating characteristic (ROC) curve analysis for medical diagnostic test evaluation', *Caspian Journal of Internal Medicine*, 4(2), pp. 627–635.

Haralick, R. M. and Shapiro, L. G. (1993) *Computer and Robot Vision Vol. 2*. Addison-Wesley.

Hawthorne, E. W. (1966) 'Dynamic geometry of the left ventricle', *The American Journal of Cardiology*, 18(4), pp. 566–573. doi: 10.1016/0002-9149(66)90012-9.

High, W. A., Ayers, R. A., Chandler, J., *et al.* (2007) 'Gadolinium is detectable within the tissue of patients with nephrogenic systemic fibrosis', *Journal of the American Academy of Dermatology*, 56(1), pp. 21–26. doi: 10.1016/j.jaad.2006.10.047.

Hor, K. N., Baumann, R., Pedrizzetti, G., *et al.* (2011) 'Magnetic resonance derived myocardial strain assessment using feature tracking', *Journal of Visualized Experiments*, (48), pp. 1–6. doi: 10.3791/2356.

ImageJ (no date) 'Fiji - https://imagej.net/Fiji'.

Jung, J., Kang, H., Kim, M., *et al.* (2012) 'Immediate Hypersensitivity Reaction to Gadolinium-based MR Contrast Media', *RSNA Radiology*, 264(2). doi: 10.1148/radiol.12112025/-/DC1.

Kali, A., Cokic, I., Tang, R. L. Q., *et al.* (2014) 'Determination of location, size, and transmurality of chronic myocardial infarction without exogenous contrast media by using cardiac magnetic resonance imaging at 3 T', *Circulation: Cardiovascular Imaging*, 7(3), pp. 471–481. doi: 10.1161/CIRCIMAGING.113.001541.

Kali, A., Choi, E. Y., Sharif, B., *et al.* (2015) 'Native T1 Mapping by 3-T CMR Imaging for Characterization of Chronic Myocardial Infarctions', *JACC: Cardiovascular Imaging*, 8(9), pp. 1019–1030. doi: 10.1016/j.jcmg.2015.04.018.

Kalin, R. and Stanton, M. S. (2005) 'Current clinical issues for MRI scanning of pacemaker and defibrillator patients', *PACE - Pacing and Clinical Electrophysiology*, 28(4), pp. 326–328. doi: 10.1111/j.1540-8159.2005.50024.x.

Kanal, E. and Tweedle, M. F. (2015) 'Residual or Retained Gadolinium: Practical Implications for Radiologists and Our Patients', *Radiology*, 275(3), pp. 630–634. doi: 10.1148/radiol.2015150805.

Kanda, T., Matsuda, M., Oba, H., *et al.* (2015) 'Gadolinium Deposition after Contrastenhanced MR Imaging', *Radiology*, 277(3).

Katz, A. M. (2011) *Physiology of the Heart*. Fifth. WOLTERS KLUWER | LIPPINCOTT WILLIAMS & WILKINS.

Khan, J. N., Singh, A., Nazir, S. A., *et al.* (2015) 'Comparison of cardiovascular magnetic resonance feature tracking and tagging for the assessment of left ventricular systolic strain in acute

myocardial infarction', *European Journal of Radiology*, 84(5), pp. 840–848. doi: 10.1016/j.ejrad.2015.02.002.

Kihlberg, J., Haraldsson, H., Sigfridsson, A., *et al.* (2015) 'Clinical experience of strain imaging using DENSE for detecting infarcted cardiac segments', *Journal of Cardiovascular Magnetic Resonance*, 17(1), pp. 1–9. doi: 10.1186/s12968-015-0155-8.

Knutsson, H. and Andersson, M. (2005) 'MORPHONS: Segmentation using elastic canvas and paint on priors', in *International Conference on Image Processing, IEEE*.

Kroon, D.-J. (no date) *MATLAB File Exchange*. Available at: https://www.mathworks.com/matlabcentral/mlc-downloads/downloads/submissions/21451/versions/12/previews/functions/strain.m/index.html (Accessed: 10 August 2016).

Kuhn, M. and Johnson, K. (2013) 'Applied Predictive Modeling', in. Springer Nature, pp. 69–71. doi: 10.1007/978-1-4614-6849-3.

Lai, W. M., Rubin, D. and Krempl, E. (2010) *Introduction to continuum mechanics, Chapter 3*. Butterworth-Heinemann/Elsevier. Available at: https://www.sciencedirect.com/science/book/9780750685603 (Accessed: 21 March 2018).

Lewis, J. P. (1995) 'Fast Normalized Cross Correlation', *Industrial Light & Magic*, 10(11), pp. 120–123. Available at: http://citeseerx.ist.psu.edu/viewdoc/download?doi=10.1.1.157.3888&rep=rep1&type=pdf.

Lima, J. A. C. and Desai, M. Y. (2004) 'Cardiovascular magnetic resonance imaging: Current and emerging applications', *Journal of the American College of Cardiology*, 44(6), pp. 1164–1171. doi: 10.1016/j.jacc.2004.06.033.

Maes, F., Collignon, A., Vandermeulen, D., *et al.* (1997) 'Multimodality image registration by maximization of mutual

information', *IEEE Transactions on Medical Imaging*, 16(2), pp. 187–198. doi: 10.1109/42.563664.

Mangion, K., McComb, C., Auger, D. A., *et al.* (2017) 'Magnetic resonance imaging of myocardial strain after acute st-segment-elevation myocardial infarction a systematic review', *Circulation: Cardiovascular Imaging*, 10(8), pp. 1–10. doi: 10.1161/CIRCIMAGING.117.006498.

Manovel, A., Dawson, D., Smith, B., *et al.* (2010) 'Assessment of left ventricular function by different speckle-tracking software', *European Journal of Echocardiography*, 11(5), pp. 417–421. doi: 10.1093/ejechocard/jep226.

Mansi, T., Pennec, X., Sermesant, M., *et al.* (2011) 'iLogDemons: A demons-based registration algorithm for tracking incompressible elastic biological tissues', *International Journal of Computer Vision*, 92(1), pp. 92–111. doi: 10.1007/s11263-010-0405-z.

Martin, T. N., Groenning, B. A., Murray, H. M., *et al.* (2007) 'ST-Segment Deviation Analysis of the Admission 12-Lead Electrocardiogram as an Aid to Early Diagnosis of Acute Myocardial Infarction With a Cardiac Magnetic Resonance Imaging Gold Standard', *Journal of the American College of Cardiology*, 50(11), pp. 1021–1028. doi: 10.1016/j.jacc.2007.04.090.

Maude, A. D. (1971) 'Interpolation-mainly for graph plotters', *The Computer Journal*.

McDonald, J. S., Hunt, C. H., Kolbe, A. B., *et al.* (2019) 'Acute Adverse Events Following Gadolinium-based Contrast Agent Administration: A Single-Center Retrospective Study of 281 945 Injections', *Radiology*, 292(3), pp. 620–627. doi: 10.1148/radiol.2019182834.

McDonald, R. J., McDonald, J. S., Kallmes, D. F., *et al.* (2015)

'Intracranial Gadolinium Deposition after Contrast-enhanced MR Imaging', *Radiology*, 275(3), pp. 772–782. doi: 10.1148/radiol.15150025.

McLeod, K., Prakosa, A., Mansi, T., *et al.* (2012) 'An Incompressible Log-Domain Demons Algorithm for Tracking Heart Tissue', in Camara, O. et al. (eds) *Statistical Atlases and Computational Models of the Heart*. Berlin, Heidelberg: Springer Berlin Heidelberg, pp. 55–67.

McVeigh, E. R. and Atalar, E. (1992) 'Cardiac Tagging with Breath-Hold Cine MRI', *Magnetic Resonance in Medicine*, 28(2), pp. 318–327. doi: 10.1002/mrm.1910280214.

Messroghli, D. R., Walters, K., Plein, S., *et al.* (2007) 'Myocardial T1mapping: Application to patients with acute and chronic myocardial infarction', *Magnetic Resonance in Medicine*, 58(1), pp. 34–40. doi: 10.1002/mrm.21272.

Meunier, J. (1998) 'Tissue motion assessment from 3D echographic speckle tracking.', *Physics in medicine and biology*, 43(5), pp. 1241–1254. doi: 10.1088/0031-9155/43/5/014.

Mildenberger, P., Eichelberg, M. and Martin, E. (2002) 'Introduction to the DICOM standard', *European Radiology*, 12(4), pp. 920–927. doi: 10.1007/s003300101100.

Miyagi, H., Nagata, M., Kitagawa, K., *et al.* (2013) 'Quantitative assessment of myocardial strain with displacement encoding with stimulated echoes MRI in patients with coronary artery disease', *International Journal of Cardiovascular Imaging*, 29(8), pp. 1779–1786. doi: 10.1007/s10554-013-0274-y.

Modat, M., Ridgway, G. R., Taylor, Z. A., *et al.* (2010) 'Fast free-form deformation using graphics processing units', *Computer Methods and Program in Biomedicine*, 98, pp. 278–284. doi: 10.1016/j.cmpb.2009.09.002.

Molinaro, A. M., Simon, R. and Pfeiffer, R. M. (2005) 'Prediction error estimation: A comparison of resampling methods', *Bioinformatics*, 21(15), pp. 3301–3307. doi: 10.1093/bioinformatics/bti499.

Moore, C. C., Lugo-Olivieri, C. H., McVeigh, E. R., *et al.* (2000) 'Three-dimensional Systolic Strain Patterns in the Normal Human Left Ventricle: Characterization with Tagged MR Imaging', *Radiology*, 214(2), pp. 453–466. doi: 10.1148/radiology.214.2.r00fe17453.

Nacif, M. S., Arai, A. E., Lima, J. A. C., *et al.* (2012) 'Gadolinium-enhanced cardiovascular magnetic resonance : administered dose in relationship to united states food and drug administration (FDA) guidelines', *Journal of Cardiovascular Magnetic Resonance*, 14(18), pp. 1–8.

Nakatani, S. (2011) 'Left Ventricular Rotation and Twist: Why Should We Learn?', *Journal of Cardiovascular Ultrasound*, 19(1), p. 1. doi: 10.4250/jcu.2011.19.1.1.

Nezafat, R. (2015) 'Native T1Mapping for Myocardial Infarction Time to Throw Out the Gadolinium?', *JACC: Cardiovascular Imaging*, 8(9), pp. 1031–1033. doi: 10.1016/j.jcmg.2015.07.003.

Osman, N. F., Kerwin, W. S., Mcveigh, E. R., *et al.* (1999) 'Cardiac Motion Tracking Using CINE Harmonic Phase (HARP) Magnetic Resonance Imaging', *Magnetic Resonance in Medicine*, 42, pp. 1048–1060.

Osman, N. F., Sampath, S., Atalar, E., *et al.* (2001) 'Imaging longitudinal cardiac strain on short-axis images using strain-encoded MRI', *Magnetic Resonance in Medicine*, 46(2), pp. 324–334. doi: 10.1002/mrm.1195.

Oyama-Manabe, N., Ishimori, N., Sugimori, H., *et al.* (2011) 'Identification and further differentiation of subendocardial and

transmural myocardial infarction by fast strain-encoded (SENC) magnetic resonance imaging at 3.0 Tesla', *European Radiology*, 21(11), pp. 2362–2368. doi: 10.1007/s00330-011-2177-4.

Ozturk, C. and Mcveigh, E. R. (2000) 'Four-dimensional B-spline based motion analysis of tagged MR images : introduction and in vivo validation', *Physics in Medicine & Biology*, 1683.

Pan, L., Prince, J. L., Lima, J. A. C., *et al.* (2005) 'Fast tracking of cardiac motion using 3D-HARP', *IEEE Transactions on Biomedical Engineering*, 52(8), pp. 1425–1435. doi: 10.1109/TBME.2005.851490.

Papademetris, X., Sinusas, A. J., Dione, D. P., *et al.* (2002) 'Estimation of 3-D left ventricular deformation from medical images using biomechanical models', *IEEE Transactions on Medical Imaging*, 21(7), pp. 786–800. doi: 10.1109/TMI.2002.801163.

Pedrizzetti, G., Claus, P., Kilner, P. J., *et al.* (2016) 'Principles of cardiovascular magnetic resonance feature tracking and echocardiographic speckle tracking for informed clinical use', *Journal of Cardiovascular Magnetic Resonance*, 18(1), pp. 1–12. doi: 10.1186/s12968-016-0269-7.

Pennell, D. J., Sechtem, U. P., Higgins, C. B., *et al.* (2004) 'Clinical indications for cardiovascular magnetic resonance (CMR): Consensus Panel report', *European Heart Journal*, 25, pp. 1940–1965. doi: 10.1016/j.ehj.2004.06.040.

Pfeffer, M. A. and Braunwald, E. (1990) 'Ventricular remodeling after myocardial infarction. Experimental observations and clinical implications', *Circulation*, pp. 1161–1172. doi: 10.1161/01.CIR.81.4.1161.

Prince, J. L., Gupta, S. N. and Osman, N. F. (2000) 'Bandpass optical flow for tagged MRI', *Medical Physics*, 27(1), pp. 108–118. doi:

10.1118/1.598862.

Radeva, P., Amini, A. A. and Huang, J. (1997) 'Deformable B-Solids and Implicit Snakes for 3D Localization and Tracking of SPAMM MRI Data', *Computer Vision and Image Understanding*, 66(2), pp. 163–178.

Remme, E. W., Augenstein, K. F., Young, A. A., *et al.* (2005) 'Parameter distribution models for estimation of population based left ventricular deformation using sparse fiducial markers.', *IEEE transactions on medical imaging*, 24(3), pp. 381–388.

Rueckert, D., Hayes, C., Studholme, C., *et al.* (1998) 'Non-rigid registration of breast MR images using mutual information', in Wells, W. M., Colchester, A., and Delp, S. (eds) *Medical Image Computing and Computer-Assisted Intervention — MICCAI'98*. Berlin, Heidelberg: Springer Berlin Heidelberg, pp. 1144–1152.

Rueckert, D., Sonoda, L. I., Hayes, C., *et al.* (1999) 'Nonrigid registration using free-form deformations: application to breast MR images.', *IEEE Transactions on Medical Imaging*, 18(8), pp. 712–21. doi: 10.1109/42.796284.

Rutz, A. K., Ryf, S., Plein, S., *et al.* (2008) 'Accelerated Whole-Heart 3D CSPAMM for Myocardial Motion Quantification', *Magnetic Resonance in Medicine*, 59, pp. 755–763. doi: 10.1002/mrm.21363.

Sampath, S., Osman, N. F. and Prince, J. L. (2013) 'A combined harmonic phase and strain-encoded pulse sequence for measuring three-dimensional strain', *Magnetic Resonance Imaging*, 27(1), pp. 55–61. doi: 10.1038/mp.2011.182.doi.

Schär, M., Kozerke, S., Fischer, S. E., *et al.* (2004) 'Cardiac SSFP Imaging at 3 Tesla', *Magnetic Resonance in Medicine*, 51(4), pp. 799–806. doi: 10.1002/mrm.20024.

Schnabel, J. A., Rueckert, D., Quist, M., *et al.* (2001) 'A generic

framework for non-rigid registration based on non-uniform multi-level free-form deformations', *Lecture Notes in Computer Science (including subseries Lecture Notes in Artificial Intelligence and Lecture Notes in Bioinformatics)*, 2208, pp. 573–581. doi: 10.1007/3-540-45468-3_69.

Schuster, A., Stahnke, V. C., Unterberg-Buchwald, C., *et al.* (2015) 'Cardiovascular magnetic resonance feature-tracking assessment of myocardial mechanics: Intervendor agreement and considerations regarding reproducibility', *Clinical Radiology*, 70(9), pp. 989–998. doi: 10.1016/j.crad.2015.05.006.

Selvadurai, B. S. N., Puntmann, V. O., Bluemke, D. A., *et al.* (2018) 'Definition of Left Ventricular Segments for Cardiac Magnetic Resonance Imaging', *JACC: Cardiovascular Imaging*, 11(6), pp. 926–928. doi: 10.1016/j.jcmg.2017.09.010.

Sengupta, P. P., Tajik, A. J., Chandrasekaran, K., *et al.* (2008) 'Twist Mechanics of the Left Ventricle. Principles and Application', *JACC: Cardiovascular Imaging*, 1(3), pp. 366–376. doi: 10.1016/j.jcmg.2008.02.006.

Shi, W., Zhuang, X., Wang, H., *et al.* (2012) 'A comprehensive cardiac motion estimation framework using both untagged and 3-D tagged MR images based on nonrigid registration', *IEEE Transactions on Medical Imaging*, 31(6), pp. 1263–1275. doi: 10.1109/TMI.2012.2188104.

Shi, W., Zhuang, X., Pizarro, L., *et al.* (2012) 'Registration using sparse free-form deformations.', *Medical image computing and computer-assisted intervention : MICCAI ... International Conference on Medical Image Computing and Computer-Assisted Intervention*, 15(Pt 2), pp. 659–66. Available at: http://www.ncbi.nlm.nih.gov/pubmed/23286105.

Šimundić, A.-M. (2009) 'Measures of Diagnostic Accuracy: Basic DefinitiŠimundić, A.-M. (2009). Measures of Diagnostic Accuracy:

Basic Definitions. EJIFCC, 19(4), 203–11. Retrieved from http://www.ncbi.nlm.nih.gov/pubmed/27683318ons.', *Ejifcc*, 19(4), pp. 203–11. doi: eJIFCC2008Vol19No4pp203-211.

Sjøli, B., Ørn, S., Grenne, B., *et al.* (2009) 'Diagnostic Capability and Reproducibility of Strain by Doppler and by Speckle Tracking in Patients With Acute Myocardial Infarction', *JACC: Cardiovascular Imaging*, 2(1), pp. 24–33. doi: 10.1016/j.jcmg.2008.10.007.

Smiseth, O. A., Torp, H., Opdahl, A., *et al.* (2016) 'Myocardial strain imaging: How useful is it in clinical decision making?', *European Heart Journal*, 37(15), pp. 1196-1207b. doi: 10.1093/eurheartj/ehv529.

Strom, J. B., Whelan, J. B., Shen, C., *et al.* (2017) 'Safety and utility of magnetic resonance imaging in patients with cardiac implantable electronic devices', *Heart rhythm*. 2017/04/03, 14(8), pp. 1138–1144. doi: 10.1016/j.hrthm.2017.03.039.

Tautz, L., Hennemuth, A. and Peitgen, H.-O. (2011) 'Motion Analysis with Quadrature Filter Based Registration of Tagged MRI Sequences', in Camara, O. et al. (eds) *International Workshop on Statistical Atlases and Computational Models of the Heart (STACOM)*. Berlin, Heidelberg: Springer Berlin Heidelberg, pp. 78–87.

Taylor, A. J., Salerno, M., Dharmakumar, R., *et al.* (2016) 'T1 Mapping Basic Techniques and Clinical Applications', *JACC: Cardiovascular Imaging*, 9(1), pp. 67–81. doi: 10.1016/j.jcmg.2015.11.005.

Thomsen, H. S., Morcos, S. K., Almén, T., *et al.* (2013) 'Nephrogenic systemic fibrosis and gadolinium-based contrast media: updated ESUR Contrast Medium Safety Committee guidelines', *European Radiology*, 23(2), pp. 307–318. doi: 10.1007/s00330-012-2597-9.

Thygesen, K., Alpert, J. S., Jaffe, A. S., *et al.* (2012) 'Third universal

definition of myocardial infarction', *Nature Reviews Cardiology*, 9(11), pp. 620–633. doi: 10.1038/nrcardio.2012.122.

Tobon-Gomez, C., Craene, M. De, Mcleod, K., *et al.* (2013) 'Benchmarking framework for myocardial tracking and deformation algorithms : An open access database', *Medical Image Analysis*, 17(6), pp. 632–648. doi: 10.1016/j.media.2013.03.008.

Veress, A. I., Weiss, J. A., Klein, G. J., *et al.* (2002) 'Quantification of 3D left ventricular deformation using hyperelastic warping: comparisons between MRI and PET imaging', *Computers in Cardiology, IEEE*, pp. 709–712. doi: 10.1109/cic.2002.1166871.

Vogel-Claussen, J., Rochitte, C. E., Wu, K. C., *et al.* (2006) 'Delayed enhancement MR imaging: Utility in myocardial assessment', *Radiographics*, 26(3), pp. 795–810. doi: 10.1148/rg.263055047.

Voigt, J. U., Pedrizzetti, G., Lysyansky, P., *et al.* (2015) 'Definitions for a common standard for 2D speckle tracking echocardiography: consensus document of the EACVI/ASE/Industry Task Force to standardize deformation imaging', *European heart journal cardiovascular Imaging*, 16(1), pp. 1–11. doi: 10.1093/ehjci/jeu184.

Wagner, A., Mahrholdt, H., Holly, T. A., *et al.* (2003) 'Contrast-enhanced MRI and routine single photon emission computed tomography (SPECT) perfusion imaging for detection of subendocardial myocardial infarcts: an imaging study', *The Lancet*, 361(9355), pp. 374–379. doi: 10.1016/S0140-6736(03)12389-6.

Wang, H. and Amini, A. A. (2012) 'Cardiac motion and deformation recovery from MRI: A review', *IEEE Transactions on Medical Imaging*, 31(2), pp. 487–503. doi: 10.1109/TMI.2011.2171706.

Wang, H. and Amini, A. A. (2013) 'Cardiac deformation analysis using 3D SinMod from 3D CSPAMM tagged MRI', *Medical Imaging 2013: Biomedical Applications in Molecular, Structural, and Functional Imaging*, 8672(March 2013), p. 86720B. doi: 10.1117/12.2008426.

WHO (2017) *WHO | Cardiovascular Diseases (CVDs)*. Available at: http://www.who.int/mediacentre/factsheets/fs317/en/ (Accessed: 16 February 2020).

Wong, D. T. L., Leong, D. P., Weightman, M. J., *et al.* (2014) 'Magnetic resonance-derived circumferential strain provides a superior and incremental assessment of improvement in contractile function in patients early after ST-segment elevation myocardial infarction', *European Radiology*, 24(6), pp. 1219–1228. doi: 10.1007/s00330-014-3137-6.

Young, A. A. (1999) 'Model tags: direct three-dimensional tracking of heart wall motion from tagged magnetic resonance images.', *Medical image analysis*, 3(4), pp. 361–372. doi: 10.1016/S1361-8415(99)80029-2.

Zagorchev, L. and Goshtasby, A. (2006) 'A comparative study of transformation functions for nonrigid image registration.', *IEEE transactions on image processing : a publication of the IEEE Signal Processing Society*, 15(3), pp. 529–538. doi: 10.1109/TIP.2005.863114.

Zhang, Y., Chan, A. K. Y., Yu, C. M., *et al.* (2005) 'Strain rate imaging differentiates transmural from non-transmural myocardial infarction: A validation study using delayed-enhancement magnetic resonance imaging', *Journal of the American College of Cardiology*, 46(5), pp. 864–871. doi: 10.1016/j.jacc.2005.05.054.

Zhou, Y., Bernard, O., Saloux, E., *et al.* (2015) '3D harmonic phase tracking with anatomical regularization', *Medical Image Analysis*, 26(1), pp. 70–81. doi: 10.1016/j.media.2015.08.003.

APPENDIX-1

✓ **BSREC Approval**

WARWICK
THE UNIVERSITY OF WARWICK

PRIVATE
Mr Jayendra Bhalodiya
PhD Student
WMG
University of Warwick
Coventry
CV4 7AL

5 December 2016

Dear Mr Bhalodiya

Study Title and BSREC Reference: *Computational Modelling of Human Heart using MR Images* REGO-2016-1865

Thank you for submitting your revisions to the above-named study to the University of Warwick's Biomedical and Scientific Research Ethics Sub-Committee for approval.

I am pleased to confirm that approval is granted and that your study may commence.

In undertaking your study, you are required to comply with the University of Warwick's *Research Data Management Policy*, details of which may be found on the Research and Impact Services' webpages, under "Codes of Practice & Policies" » "Research Code of Practice" » "Data & Records" » "Research Data Management Policy", at: http://www2.warwick.ac.uk/services/ris/research_integrity/code_of_practice_and_policies/research_code_of_practice/datacollection_retention/research_data_mgt_policy

You are also required to comply with the University of Warwick's *Information Classification and Handling Procedure*, details of which may be found on the University's Governance webpages, under "Governance" » "Information Security" » "Information Classification and Handling Procedure", at:
http://www2.warwick.ac.uk/services/gov/informationsecurity/handling.
Investigators should familiarise themselves with the classifications of information defined therein, and the requirements for the storage and transportation of information within the different classifications:

> *Information Classifications:*
> http://www2.warwick.ac.uk/services/gov/informationsecurity/handling/classifications
> *Handling Electronic Information:*
> http://www2.warwick.ac.uk/services/gov/informationsecurity/handling/electronic/
> *Handling Paper or other media*
> http://www2.warwick.ac.uk/services/gov/informationsecurity/handling/paper/.

Please also be aware that BSREC grants **ethical approval** for studies. **The seeking and obtaining of _all_ other necessary approvals is the responsibility of the investigator.**

These other approvals may include, but are not limited to:

www.warwick.ac.uk

1. Any necessary agreements, approvals, or permissions required in order to comply with the University of Warwick's Financial Regulations and Procedures.
2. Any necessary approval or permission required in order to comply with the University of Warwick's Quality Management System and Standard Operating Procedures for the governance, acquisition, storage, use, and disposal of human samples for research.
3. All relevant University, Faculty, and Divisional/Departmental approvals, if an employee or student of the University of Warwick.
4. Approval from the applicant's academic supervisor and course/module leader (as appropriate), if a student of the University of Warwick.
5. NHS Trust R&D Management Approval, for research studies undertaken in NHS Trusts.
6. NHS Trust Clinical Audit Approval, for clinical audit studies undertaken in NHS Trusts.
7. Approval from Departmental or Divisional Heads, as required under local procedures, within Health and Social Care organisations hosting the study.
8. Local ethical approval for studies undertaken overseas, or in other HE institutions in the UK.
9. Approval from Heads (or delegates thereof) of UK Medical Schools, for studies involving medical students as participants.
10. Permission from Warwick Medical School to access medical students or medical student data for research or evaluation purposes.
11. NHS Trust Caldicott Guardian Approval, for studies where identifiable data is being transferred outside of the direct clinical care team. Individual NHS Trust procedures vary in their implementation of Caldicott guidance, and local guidance must be sought.
12. Any other approval required by the institution hosting the study, or by the applicant's employer.

There is no requirement to supply documentary evidence of any of the above to BSREC, but applicants should hold such evidence in their Study Master File for University of Warwick auditing and monitoring purposes. You may be required to supply evidence of any necessary approvals to other University functions, e.g. The Finance Office, Research & Impact Services (RIS), or your Department/School.

May I take this opportunity to wish you success with your study, and to remind you that any Substantial Amendments to your study require approval from BSREC before they may be implemented.

Yours sincerely

pp.

Professor John Davey
Chair
Biomedical and Scientific
Research Ethics Sub-Committee

**Biomedical and Scientific
Research Ethics Sub-Committee**
Research & Impact Services
University of Warwick
Coventry, CV4 8UW.
E: BSREC@Warwick.ac.uk

http://www2.warwick.ac.uk/services/
ris/research_integrity/researchethics
committees/biomed

✓ RBHT Approval

NHS
Health Research Authority

Dr Sunil K Bhudia
Consultant Cardiac Surgeon
Royal Brompton and Harefield NHS Foundation Trust
Harefield Hospital
Hill End Road
Harefield UB9 6JH

29 March 2017

Dear Dr Bhudia

Letter of HRA Approval

Study title	**Computational Modelling of Human Heart using Magentic Resonance Imaging Scans and Computational Tomography Scans**
IRAS project ID	**211977**
Sponsor	**Royal Brompton and Harefield NHS Foundation Trust**

I am pleased to confirm that **HRA Approval** has been given for the above referenced study, on the basis described in the application form, protocol, supporting documentation and any clarifications noted in this letter.

Participation of NHS Organisations in England
The sponsor should now provide a copy of this letter to all participating NHS organisations in England.

Appendix B provides important information for sponsors and participating NHS organisations in England for arranging and confirming capacity and capability. **Please read *Appendix B* carefully**, in particular the following sections:
- *Participating NHS organisations in England* – this clarifies the types of participating organisations in the study and whether or not all organisations will be undertaking the same activities
- *Confirmation of capacity and capability* - this confirms whether or not each type of participating NHS organisation in England is expected to give formal confirmation of capacity and capability. Where formal confirmation is not expected, the section also provides details on the time limit given to participating organisations to opt out of the study, or request additional time, before their participation is assumed.
- *Allocation of responsibilities and rights are agreed and documented (4.1 of HRA assessment criteria)* - this provides detail on the form of agreement to be used in the study to confirm capacity and capability, where applicable.

Further information on funding, HR processes, and compliance with HRA criteria and standards is also provided.

It is critical that you involve both the research management function (e.g. R&D office) supporting each organisation and the local research team (where there is one) in setting up your study. Contact details and further information about working with the research management function for each organisation can be accessed from www.hra.nhs.uk/hra-approval.

Appendices
The HRA Approval letter contains the following appendices:
- A – List of documents reviewed during HRA assessment
- B – Summary of HRA assessment

IRAS project ID	211977

After HRA Approval
The attached document *"After HRA Approval – guidance for sponsors and investigators"* gives detailed guidance on reporting expectations for studies with HRA Approval, including:
- Working with organisations hosting the research
- Registration of Research
- Notifying amendments
- Notifying the end of the study

The HRA website also provides guidance on these topics and is updated in the light of changes in reporting expectations or procedures.

Scope
HRA Approval provides an approval for research involving patients or staff in NHS organisations in England.

If your study involves NHS organisations in other countries in the UK, please contact the relevant national coordinating functions for support and advice. Further information can be found at http://www.hra.nhs.uk/resources/applying-for-reviews/nhs-hsc-rd-review/.

If there are participating non-NHS organisations, local agreement should be obtained in accordance with the procedures of the local participating non-NHS organisation.

User Feedback
The Health Research Authority is continually striving to provide a high quality service to all applicants and sponsors. You are invited to give your view of the service you have received and the application procedure. If you wish to make your views known please use the feedback form available on the HRA website: http://www.hra.nhs.uk/about-the-hra/governance/quality-assurance/.

HRA Training
We are pleased to welcome researchers and research management staff at our training days – see details at http://www.hra.nhs.uk/hra-training/

Your IRAS project ID is **211977**. Please quote this on all correspondence.

Yours sincerely

Michael Higgs
Assessor

Email: hra.approval@nhs.net

Copy to: Patrik Pettersson, Royal Brompton and Harefield NHS Foundation Trust *[Sponsor and NHS R&D contact]*

✓ **Honorary Observer placement contract**

Royal Brompton & Harefield **NHS**
NHS Foundation Trust

A lifetime of specialist care

Royal Brompton Hospital
Sydney Street
London
SW3 6NP

PRIVATE AND CONFIDENTIAL

28 March 2018
Sent Via Email

T: +44 (0)20 7352 8121
F: +44 (0)20 7351 8473

Dear Dr Jayendra Maganbhai Bhalodiya,

Honorary Observer (non-participant) Contract

Statement of Terms and Conditions of Service for Honorary Appointments

1. I am directed by the Royal Brompton and Harefield NHS Foundation Trust ("the Trust") to offer you an Honorary Contract in the CMR Unit department. Your appointment commences on the 28th April 2018 and terminates on the 27th April 2019. Your Sponsor will be Dr Sanjay Prasad/Dr Sunil Bhudia. Under the terms of this of this appointment you are not entitled to any form of payment or access to other benefits provided by the Trust to employees.

2. This honorary contract is offered to you subject to satisfactory evidence of medical fitness and the Trust reserves the right to request that you have a medical examination to ascertain your state of health at any time.

3. The Trust accepts no responsibility for damage to or loss of personal property and you are therefore recommended to take out an insurance policy to cover your personal property.

4. The Royal Brompton and Harefield NHS Foundation Trust will cover all staff for NHS work under Crown Indemnity and is required to encourage staff to ensure they have adequate defence cover for any work which does not fall within the scope of the indemnity scheme.

5. You are expected to maintain confidentiality of information relating to patients, staff, and Trust business matters and to pay due regard to relevant legislation. This does not affect your rights under the Public Interest Disclosure Act 1998.

6. You are required to keep the Trust aware on an ongoing basis of any conflict or potential conflict of interests which may arise during the period of your appointment. If you are in any doubt whether a conflict exists, or may exist, you must inform the Trust.

7. While your honorary contract does not confer the status of an employee of the Trust upon you, it is a condition of this honorary contract, because you will be working on Trust premises, that you maintain certain standards of conduct expected of any honorary post holder. These standards include but are not limited to those standards set out in policies listed below:

   - Diversity policy (inc. Harassment and Bullying at Work)
   - 'Whistle Blowing' Policy
   - Health and Safety
   - Confidentiality
   - No Smoking
   - Alcohol at work
   - Information Governance Policy

   *All policies can be found on the Trust Intranet

8. Royal Brompton & Harefield NHS Foundation Trust manages all research in accordance with the requirements of the research governance framework. As an honorary employee of the Royal Brompton and Harefield NHS Trust you must comply with all reporting requirements, systems, and duties of action put in place by the Trust to deliver research governance.

Revised July 2017

www.rbht.nhs.uk   @RBandH

9. The contract may be terminated by you with one month's notice in writing to the Trust. A copy of the termination letter must be sent to the Human Resources Department.

The contract may be terminated by the Trust with immediate effect at any time. This is most likely to occur in the event of failure to observe the terms of this Agreement and/or in the following circumstances:

- Serious or repeated breach after warning of Trust's regulations and procedures
- Serious misconduct and/or negligence in the course of this employment.

Otherwise this contract will automatically cease at the date indicated above. However, you may be considered for a new honorary contract.

10. Under the terms of this contract you are not entitled to any form of payment or access to other benefits provided by the Trust to its employees. Although you will at all times be subject to the Trust's policies, procedures, rules and regulations, contract of an honorary nature only and does not give rise to any other relationship between you and the Trust, in particular that of a contract of employment. For the avoidance of doubt, this honorary contract does not connote any obligation on the part of the Trust to provide you with work, nor does it connote any obligation on your part to accept any work offered.

Observer Duties:

Non GMC registered observers are <u>not permitted</u> to:

- prescribe
- order diagnostic tests or radiological examinations
- take specimens
- initiate, advise, order or stop the treatment of patients
- undertake clinical procedures
- teach clinical procedures
- "scrub up" in theatre.
- take any part in obtaining/witnessing the signature by/on behalf of a patient on a form of consent to treatment

Non GMC registered clinical observers may <u>when fully supervised</u>:

- take a clinical history under supervision
- contribute to the examination of a patient (but not undertake the examination unaided)
- contribute to discussion on diagnosis (but not diagnose or advise treatment).
- participate in non-invasive, low risk external imaging (eg cutaneous ultrasound, transthoracic echocardiography) for educational purposes and with the voluntary and informed consent of the patient. Observers must be fully supervised by a Consultant in this situation and must not be responsible in any way for interpreting or reporting the results
- observe in theatre. With the proviso that this is for educational purposes and not for service. Observers may not perform autonomous surgery (e.g. open or close surgical incisions, harvest conduit, insert drains etc) and may only be in theatre when the supervising Consultant is present.

Yours sincerely,

Jasmine Frimpong
Medical HR Honorary Coordinator

I hereby accept the honorary appointment offered by the Royal Brompton & Harefield NHS Foundation Trust in the foregoing letter on the terms and subject to the conditions referred to in it.

Name: _Jayembry_   Date: _28/3/2018_

Signed: ▉▉▉▉▉

Ver.1 - October 2017   2   Medical HR

APPENDIX 2

ALGORITHM AND CODE

- **HTM Algorithm**

Algorithm | HTM-based Myocardial Tracking

Parameters: I: set of N images, I_M: Moving Image, I_R: Reference Image, NCC: Normalized Cross-Correlation, T_M: Moving Template, T_R: Reference Template, S_M: Moving Segment, S_R: Reference Segment, C_M: Moving Chunk, C_R: Reference Chunk, W_M: Moving Window, W_R: Reference Window, T_{size}: Template Size, P_M: Moving Points Set, P_R: Reference Point Set, P_{myo}: Myocardial Point Set, i: i^{th} template, j: j^{th} segment, k: k^{th} chunk, l: l^{th} window, N: Number of images

Require: I, set of N images

initialize: $T_{size} = 16{\times}16$

repeat

    for each: im ϵ I **do**

        initialize: $I_R =$ im, $I_M =$ next(im)

        calculate: T_M locations

        for each: movingT ϵ T_M **do**

            referenceT $\leftarrow$ NCC (movingT, I_R)

            calculate: S_M locations

            for each: movingS ϵ S_M **do**

                referenceS $\leftarrow$ NCC(movingS, referenceT)

                calculate: C_M locations

                for each: movingC ϵ C_M **do**

                    referenceC $\leftarrow$ NCC(movingC, referenceS)

                    calculate: W_M locations

                    for each: movingW ϵ W_M **do**

referenceW←NCC(moving W, referenceC)

$W_R[l] \leftarrow$ referenceW

end for

$C_R[k] \leftarrow$ referenceC

end for

$S_R[j] \leftarrow$ referenceS

end for

$T_R[i] \leftarrow$ referenceT

end for

$P_M \leftarrow W_M$ locations

$P_R \leftarrow W_R$ locations

function: track_myocardial_points (P_{myo}, P_M, P_R)

tform ← Local_Weighted_Mean (P_M, P_R)

calculate: $R_{myo} \leftarrow f$ (tform, P_{myo})

return: R_{myo}

end function

end for

until index(im) < N

- **Strain calculation MATLAB code**

```matlab
function [E, D]=strain(Ux,Uy,Uz)

% Calculate the Lagranje strain from displacement images
%
% E = STRAIN(Ux,Uy)  or (3D)  E = STRAIN(Ux,Uy, Uz)
%
% inputs,
%   Ux,Uy: The displacement vector images in
%        x and y direction
%   Uz: The displacement vector image in z direction.
%
% outputs,
%   E the 3-D Lagranje tensor images defined by Lai et al. 1993
%     with dimensions [SizeX SizeY 2 2] or in 3D [SizeX SizeY SizeZ 3 3]
%
% Source used:
% Abd-elmoniem, K. Z., Stuber, M. and Prince, J. L. (2008) 'Direct
% three-dimensional myocardial strain tensor quantification and
% tracking using z HARP', Medical Image Analysis. Elsevier B.V.,
% 12(6), pp. 778–786. doi: 10.1016/j.media.2008.03.008.


%


if(~exist('Uz','var')) % Detect if 2D or 3D inputs
```

```
% Initialize output matrix

E=zeros([size(Ux) 2 2]);

% displacement images gradients

[Uxy,Uxx] = gradient(Ux);

[Uyy,Uyx] = gradient(Uy);

% Loop through all pixel locations

for i=1:size(Ux,1)

   for j=1:size(Ux,2)

      % The displacement gradient

      Ugrad=[Uxx(i,j) Uxy(i,j); Uyx(i,j) Uyy(i,j)];

      % The (inverse) deformation gradient

      F=inv([1 0;0 1]-Ugrad);  % F=inv(Finv);

      D(i,j,:,:)=F;

      % the 3-D Lagranje strain tensor

      e=(1/2)*(F'*F-[1 0;0 1]);

      % Store tensor in the output matrix

      E(i,j,:,:)=e;

    end

  end

else

  % Initialize output matrix

  E=zeros([size(Ux) 3 3]);

  % displacement images gradients

  [Uxy,Uxx,Uxz] = gradient(Ux);
```

```matlab
        [Uyy,Uyx,Uyz] = gradient(Uy);

        [Uzy,Uzx,Uzz] = gradient(Uz);

        % Loop through all pixel locations

        for i=1:size(Ux,1)

            for j=1:size(Ux,2)

                for k=1:size(Ux,3)

                    % The displacement gradient

                        Ugrad=[Uxx(i,j,k) Uxy(i,j,k) Uxz(i,j,k); Uyx(i,j,k)
                        Uyy(i,j,k) Uyz(i,j,k);Uzx(i,j,k) Uzy(i,j,k) Uzz(i,j,k)];

                    % The (inverse) deformation gradient

                    F=inv([1 0 0;0 1 0;0 0 1]-Ugrad); %F=inv(Finv);

                    D(i,j,k,:,:)=F;

                    % the 3-D Lagranje strain tensor

                    e=(1/2)*(F'*F-[1 0 0;0 1 0;0 0 1]);

                    % Store tensor in the output matrix

                    E(i,j,k,:,:)=e;

                end

            end

        end

end
```